THE UNIVERSITY OF CHICAGO

PEEKING INTO THE FUTURE OF DARK MATTER SEARCHES

A DISSERTATION SUBMITTED TO
THE FACULTY OF THE DIVISION OF THE PHYSICAL SCIENCES
IN CANDIDACY FOR THE DEGREE OF
DOCTOR OF PHILOSOPHY

DEPARTMENT OF ASTRONOMY AND ASTROPHYSICS

BY

FEI XU

CHICAGO, ILLINOIS
MARCH 2024

My little boat has passed ten thousand mountains. - Bai Li, Tang Dynasty

The dog days are over,

The dog days are done.

Can you hear the horses?

Cause here they come.

- Florence and the Machine

TABLE OF CONTENTS

LIST OF FIGURES

LIST OF TABLES

ACKNOWLEDGMENTS

I would like to thank my Ph.D. advisor Professor Dan Hooper who has guided me to finish this great thesis and his constant support. I would like to give a very special acknowledgment to Professor Rich Kron who has been not only supporting me academically as a committee member but also as a life mentor in the past several years. He always believes in my potential and truly believes that I can overcome any difficulties. His support has helped me as I went through some of the darkest times during my PhD. I could not go this far and get the Ph.D. degree without his help. I would also like to thank Professor Dan Fabrycky for his kind support in the past years. I feel grateful for all these interesting and inspiring conversations we have had about science and religion. I would also like to thank Professor Dan Holz and other people I have worked with for their mentorship. I would like to thank Professor Chihway Chang for being my faculty mentor.

I would also like to thank Professor Xiaohui Fan, Professor Zonghong Zhu, and Dr. Fuyan Bian for their constant support even after I graduated from my undergraduate college.

I would like to thank my husband Victor Zhang and our cute cat Phoebe for giving me a place that I can safely call home millions of miles away from China.

I would like to thank my grandparents for raising me. I would also like to thank my mother and Doudou for their support. I wish I could have spent more time with them during my Ph.D.

I want to thank my best friend Yang Yang for helping me survive one of the darkest moments of my life. Thank you for chatting with me at 4 am in Beijing and telling me not to give up on life, because many good things are on their way. I would like to thank Amy Tang who has been giving me very kind and professional advice as my student mentor and supporting me like a big sister. I would also like to thank Yuhan Liu, Xinyu Zhang, Hao Li, Aritrajit Gupta, Jason Poh, Dimitrios Tanoglidis, Chuan Yin, George Noarov, Seth Lovelace, Wen Han Chiu, Ege Eren, Mun Jung Jung, Geoffery Zheng, Ian Holst, Jisheng

Zhang, Gourav Khullar, Andrew Neil, Yiming Zhong, Laticia Rebeles, Carlos Blanco, David Zegeye and numerous other friends for their constant support.

ABSTRACT

Non-baryonic dark matter is understood to constitute approximately 27% of the universe's total energy density. Despite its substantial contribution to the cosmic energy budget, its negligible non-gravitational interactions make it extremely challenging to detect. This thesis focuses on potential signals of dark matter in both the electromagnetic spectrum, in particular gamma rays, and in the form of gravitational waves. We focus on predicting the potential observational signals of dark matter, including its particle annihilation in dwarf galaxies, and in the effects of gravitational lensing. More specifically, we evaluate the sensitivity of the proposed Advanced Particle-astrophysics Telescope (APT) to dark matter in dwarf galaxies, finding that such an instrument would be capable of constraining thermal relics with masses as large as $m_X \sim$600 GeV. Moreover, if the Galactic Center gamma-ray excess is generated by dark matter annihilation, we predict that APT would detect several dwarf galaxies with high significance. Such observations could be used to test the predicted proportionality between the gamma-ray fluxes and J-factors of individual dwarf galaxies, providing us with an unambiguous test of the origin of the Galactic Center Excess. In addition to studying gamma ray from dwarf galaxies, we also discuss a recently discovered gamma-ray signal surrounding pulsars, TeV halos, which are produced through the inverse Compton scattering of very high energy electrons and positrons. Such TeV halos are responsible for a large fraction of the Milky Way's TeV-scale gamma-ray emission. We calculate the gamma-ray spectrum from the population of TeV halos located within the Andromeda Galaxy, predicting a signal that is expected to be detectable by the Cherenkov Telescope Array (CTA). We also calculate the contribution from TeV halos to the isotropic gamma-ray background (IGRB), finding that these sources should contribute significantly to this flux at the highest measured energies, constituting up to $\sim$20% of the signal observed above $\sim$0.1 TeV. Lastly, we propose a novel method using strong gravitational lensing of gravitational wave sources to probe the gravitational effects of dark matter. In particular, the strong lensing event rate and the time

delay distribution of multiply-imaged gravitational-wave binary coalescence events can be used to constrain the mass distribution of the dark matter halo lenses by measuring the characteristic velocity dispersion, σ_*, of the massive elliptical galaxy whose mass is dominated by dark matter. We calculate the strong lensing event rate for a range of second (2G) and third-generation (3G) detectors, including Advanced LIGO/Virgo, A+, Einstein Telescope (ET), and Cosmic Explorer (CE). For 3G detectors, we find that $\sim$0.1% of observed events are expected to be strongly lensed. We predict the detection of $\sim$1 lensing pair per year with A+, and $\sim$50 pairs per year with ET/CE. These rates are highly sensitive to σ_*, implying that observations of the rates will be a sensitive probe of lens properties. We explore using the time delay distribution between multiply-imaged gravitational-wave sources to constrain properties of the lenses. We find that 3G detectors would constrain σ_* to $\sim$21% after 5 years.

CHAPTER 1

INTRODUCTION

1.1 Early Observations of Dark Matter

1.1.1 Early Evidence of Dark Matter from Galaxies and Galaxy Clusters

The journey of dark matter (DM) searches began in the early 20th century. Fritz Zwicky, in 1933, observed unexpectedly high and varied velocities of galaxies within the Coma cluster [Zwicky, 1933]. Zwicky deduced that the Coma cluster's total mass greatly exceeded that of its visible matter by utilizing the virial theorem, which relates the time-averaged total kinetic energy $\langle T \rangle$ of a system to its time-averaged total gravitational potential $\langle U \rangle$. More precisely, for a stable system bound by gravitational forces, we have

$$2\langle T \rangle + \langle U \rangle = 0. \tag{1.1}$$

For a collection of particles, the kinetic energy T and potential energy U can be expressed as

$$T = \sum_i \frac{1}{2} m_i v_i^2, \tag{1.2}$$

where m_i is the mass of the i^{th} particle and v_i is its velocity, and

$$U = \sum_{i<j} \frac{-G m_i m_j}{r_{ij}}, \tag{1.3}$$

where G is the gravitational constant, m_i and m_j are the masses of the i^{th} and j^{th} particles respectively, and r_{ij} is the distance between them. This theorem implies that the overall mass of the Coma cluster significantly surpasses that of observable components like stars, gas, and dust.

Later studies of spiral galaxies strongly suggested the discrepancy between the total mass and visible matter of the Coma cluster observed by Zwicky was not special to the Coma cluster. In the 1970s, when observing the redshift of emission lines from regions of hot ionized gas in spiral galaxies, astronomer Vera Rubin and her team made the startling discovery that the orbital velocity was flat (i.e. constant) at distances far from the center of the galaxy instead of decreasing with distance, as a Newtonian mechanics calculation would indicate. For example, as shown in Figure 1.1, the galaxy rotation curve for M31 is almost flat beyond $R = 20$ kpc.

More precisely, a simple theoretical calculation of the orbital speed $v(R)$ gives

$$\begin{aligned} a = \frac{v^2}{R} &= \frac{GM(R)}{R^2}, \\ \Rightarrow v &= \sqrt{\frac{GM(R)}{R}}, \end{aligned} \tag{1.4}$$

where $M(R)$ is the mass of the galaxy within a radius R (assuming the mass distribution to be spherically symmetric). It follows that if the mass of the galaxy does not change beyond a certain radius, the velocity should decay at large R as $R^{-1/2}$ instead of being completely flat as Rubin and her team found. The galaxy rotation curves observed by Vera Rubin cannot be explained by the visible matter alone, suggesting there must be some form of invisible mass, or 'dark matter', influencing the gravitational dynamics.

1.1.2 Insights of Dark Matter from Cosmic Microwave Background

Shortly before the measurements of Rubin and Ford [1970], Arno Penzias and Robert Wilson discovered the Cosmic Microwave Background (CMB). This discovery was pivotal as subsequent analyses, notably by missions such as the Cosmic Background Explorer (COBE) [Mather, 1982], the Wilkinson Microwave Anisotropy Probe (WMAP) [Bennett et al., 2013], and the Planck satellite [Planck Collaboration and Aghanim, 2020], scrutinized the CMB in

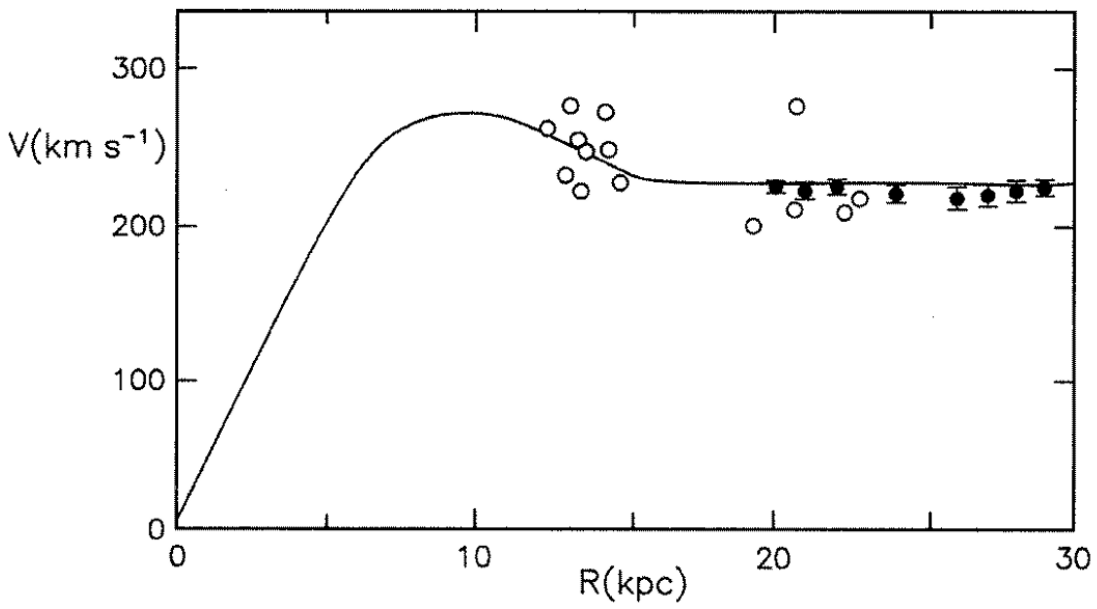

Figure 1.1: The orbital radius R versus orbital velocity v in M31. The open circles and solid dots correspond to the data points in visible wavelengths [Rubin and Ford, 1970] and radio wavelengths [Roberts and Whitehurst, 1975], respectively. This figure is sourced from van den Bergh [2000] and found in Ryden [2003].

angular power spectrum in detail. These studies revealed fluctuations consistent with the theoretical expectations of cold DM – a type of matter that neither emits nor interacts with the electromagnetic (EM) field and moves slowly compared to the speed of light. In this section, we briefly introduce the measurement of the DM abundance that can be inferred from the CMB spectrum.

Precise measurements of the spectrum of the CMB strongly indicate that the CMB can be described by a nearly perfect black body with an average temperature of $T = 2.72548 \pm 0.00057K$ [Fixsen, 2009]. Yet, the CMB doesn't exhibit this uniform temperature across the entire sky. The CMB temperature fluctuations $\Delta T(\theta, \phi)$ on the sky can be expanded in terms of spherical harmonics. At a given point on the sky with polar coordinates θ and ϕ

we have

$$\Delta T(\theta, \phi) = \sum_{l=0}^{\infty} \sum_{m=-l}^{l} a_{lm} Y_{lm}(\theta, \phi), \tag{1.5}$$

where $Y_{lm}(\theta, \phi)$ are the spherical harmonics, and a_{lm} are the expansion coefficients.

The angular power spectrum of CMB at scale l is given by

$$C_l = \frac{1}{2l+1} \sum_{m=-l}^{l} |a_{lm}|^2. \tag{1.6}$$

Larger values of l correspond to progressively smaller angular scales, e.g. $l = 2$ corresponds to the largest scales, roughly half the sky and $l = 200$ corresponds to angular scales of about 1 degree.

These anisotropies, after accounting for the motion of the Earth, are extremely subtle. These anisotropies offer a snapshot of the universe as it was about 380,000 years after the Big Bang and serve as a testing ground for our understanding of cosmology. They provide empirical data that can be used to constrain cosmological parameters such as the density of DM, the curvature of the universe, and the rate of cosmic expansion.

In the early universe, before atoms formed, there was a hot, dense plasma of photons, electrons, baryons (like protons and neutrons), and DM. Photons and baryons were tightly coupled through EM interactions in this plasma. Perturbations or density fluctuations in this plasma led to acoustic oscillations, similar to sound waves in air. These oscillations resulted in regions of compression (where the plasma is denser) and rarefaction (where the plasma is less dense). The series of peaks and troughs from the CMB power spectrum arise directly from the acoustic oscillations in the primordial plasma, through the Sachs-Wolfe effect. The Sachs-Wolfe effect refers to the temperature fluctuations in the CMB due to the gravitational redshift or blueshift of photons as they traverse through potential wells and hills, respectively. In particular, photons climbing out of a gravitational potential well (a region of higher than average density) would lose energy and get redshifted, which manifests

as a cold spot in the CMB. Conversely, photons descending into a gravitational potential well (from a region of lower than average density) gain energy and get blueshifted, which appears as a hot spot in the CMB.

During the era of radiation domination, photons provided outward pressure that resisted compression due to gravitational contraction. In particular, when a given region reached a maximum state of compression, the outward pressure from the photons caused the region to expand, making the density in that region decrease. If there is less gravitational force to suppress the rebound, the amplitude of the acoustic oscillation will remain large. However, when the DM started to dominate the energy density, it suppressed the oscillations that had not yet reached their maximum compression or had not yet rebounded. According to theory, the bounces of the first two peaks in the CMB spectrum are most strongly suppressed by the presence of DM. Therefore, the ratio of the heights of these first two peaks to those of the higher-l peaks is a powerful probe for the abundance of DM. Figure 1.2 gives a demonstration of how fitting the peaks can yield a measurement of cold DM energy density Ω_{CDM}. The details of this calculation are beyond the scope of this thesis.

1.1.3 The Thermal Relic Abundance of Dark Matter Particles

Data from the CMB is crucial for examining the effects of DM in the early stages of the universe. Although it remains a mystery what specific particle is DM, we can constrain its properties. The thermal evolution of a stable DM particle X that can annihilate in pairs, with number density n_X, can be described by the Boltzmann equation,

$$\frac{dn_X}{dt} + 3Hn_X = \langle \sigma v \rangle [n_X^2 - (n_X^{Eq})^2], \tag{1.7}$$

where H is the rate of Hubble expansion, $\langle \sigma v \rangle$ is the thermally averaged value of the annihilation cross-section multiplied by the relative velocity of the two particles, and n_X^{Eq} is

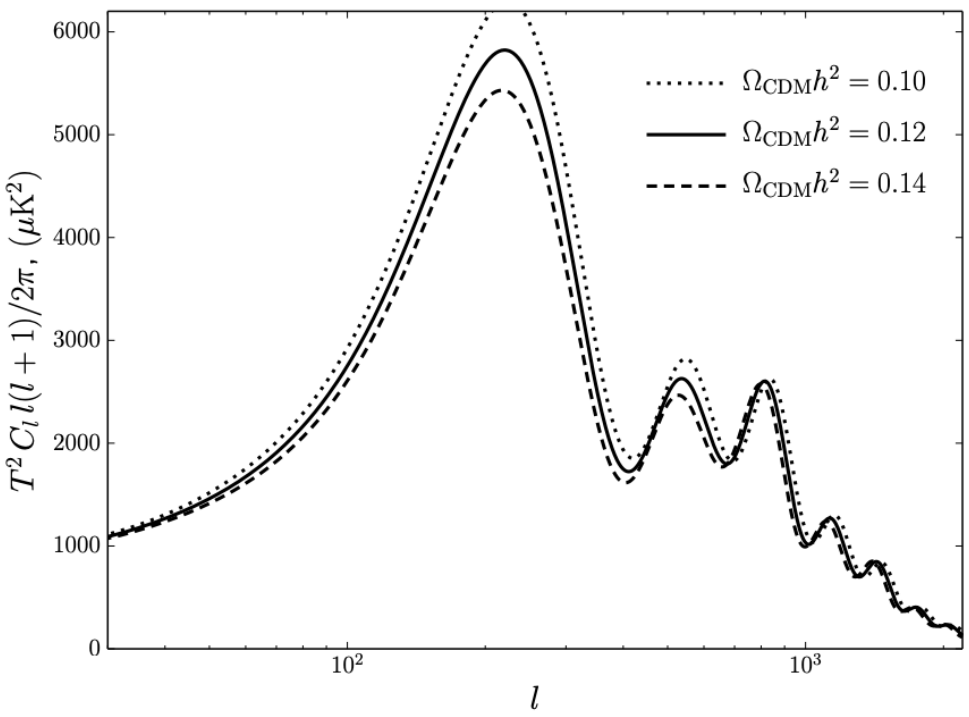

Figure 1.2: Constraints of the energy density of cold DM $\Omega_{\rm CDM}$ from CMB angular spectrum [Hooper, 2022]. Other parameters are set to their best-fit values, adjusting Ω_Λ such that $\Omega_{\rm tot} = 1$.

the equilibrium number density (i.e. the number density that would be predicted if the X population were in chemical equilibrium with the thermal bath).

In the early universe when temperatures were extremely high, DM particles were in thermal equilibrium with other standard particles, meaning they were constantly interacting, annihilating, and being produced. At high temperatures, $T \gg m_X$, the equilibrium number density of particle X is given by:

$$n_X^{Eq} = \begin{cases} \frac{\zeta(3)}{\pi^2} g_X T^3 & \text{(Bose)} \\ \frac{3}{4}\frac{\zeta(3)}{\pi^2} g_X T^3 & \text{(Fermi)}, \end{cases} \tag{1.8}$$

where $\zeta(3) \approx 1.20206$, g_X is the number of internal degrees-of-freedom of X. At lower temperatures, $T \ll m_X$, n_X^{Eq} is exponentially suppressed:

$$n_X^{Eq} = g_X \left(\frac{m_X T}{2\pi}\right)^{3/2} \exp(-m_X/T). \tag{1.9}$$

The abundance of X will continue to decrease exponentially until the expansion of the universe outpaces the interaction rate of these DM particles, or $H > n_X \langle \sigma v \rangle$. This moment when DM particles "decoupled" from the thermal bath of the universe and ceased to interact frequently with other particles, is called thermal freeze-out. The corresponding temperature is called the freeze-out temperature T_F and ranges from $1/30 - 1/10\, m_X$ for typical thermal dark matter candidates. From this point on, the comoving number density $n_X a^3$ remains almost unchanged, as $n_X \propto 1/a^3$. The total annihilation cross section can thus be revealed by the dark matter density of the present universe:

$$\Omega_X h^2 \approx 0.12 \left(\frac{2.2 \times 10^{-26} \mathrm{cm}^3/\mathrm{s}}{\langle \sigma v \rangle}\right) \left(\frac{80}{g_\star}\right)^{1/2} \left(\frac{m_X/T_F}{23}\right), \tag{1.10}$$

The cross-section $\langle \sigma v \rangle = 2.2 \times 10^{-26} \mathrm{cm}^3/\mathrm{s}$ is a generic benchmark model and popular cross-section for weakly interacting massive particles (WIMP) DM particles. It is consistent with the constraints given by the current cosmological measurements [Planck Collaboration et al., 2020]:

$$\Omega_{\mathrm{DM}} h^2 = \frac{\rho_{DM}}{\rho_{crit}} h^2 \approx 0.11933 \pm 0.00091, \tag{1.11}$$

where h is the scaled current Hubble constant, $h = \frac{H}{100 \mathrm{km/s/Mpc}}$. This value is derived from fitting the angular spectrum of CMB, especially the relative ratios of the peaks as shown in Figure 1.2. After thermal freeze out, the DM then underwent gravitational interactions to form halos and other large-scale structures.

In the derivations above, we've presumed that the particle X underwent freeze-out at a

temperature significantly lower than its mass, categorizing X as a cold thermal relic. One of the leading classes of cold DM candidates are WIMPs[1]. If the relic is exceptionally light, it may not be cold. An example are neutrinos, which experience freeze-out while being relativistic ($T \gg m_X$). Considering observations of the large-scale structures in our universe, it's unlikely that a substantial part of the DM is 'hot'. Hence, our primary focus remains on DM as a cold thermal relic. An in-depth description can be found in Hooper [2018].

1.2 Indirect Searches of Dark Matter Signals in Gamma rays

1.2.1 Gamma-Ray Telescopes: Present and Future

A joint effort of space-based and ground-based telescopes has been made to capture the gamma-ray signatures from DM annihilations. Figure 1.3 gives a summary of current and planned gamma-ray telescopes, covering the energy range from the MeV to the PeV scale.

- **The Fermi Gamma-Ray Space Telescope**: The Fermi Gamma-Ray Space Telescope, launched in 2008, covers the energy range of 0.1 to 100 GeV. It monitors the entire sky with a near one-degree angular resolution and about 10% energy resolution. Notably, Fermi aims to detect DM in the Galactic Center and in the Milky Way's dwarf galaxies. Fermi consists of two main instruments: the Large Area Telescope (LAT) and the Gamma-ray Burst Monitor (GBM). While the LAT observes high-energy gamma rays, the GBM is designed to monitor gamma-ray bursts (GRB) in the universe.

- **Advanced Particle-Astrophysics Telescope (APT)**: As Fermi has operated for more than a decade, people are planning to design its successor, the APT, to go beyond the sensitivity of Fermi. APT has been proposed to NASA and is expected to be a 10-year mission in a sun-Earth Lagrange orbit, providing near all-sky sensitivity. APT

1. The word WIMP can refer to different things in the literature. In this thesis, WIMP refers to particles that interact through the electroweak force or a similarly feeble force.

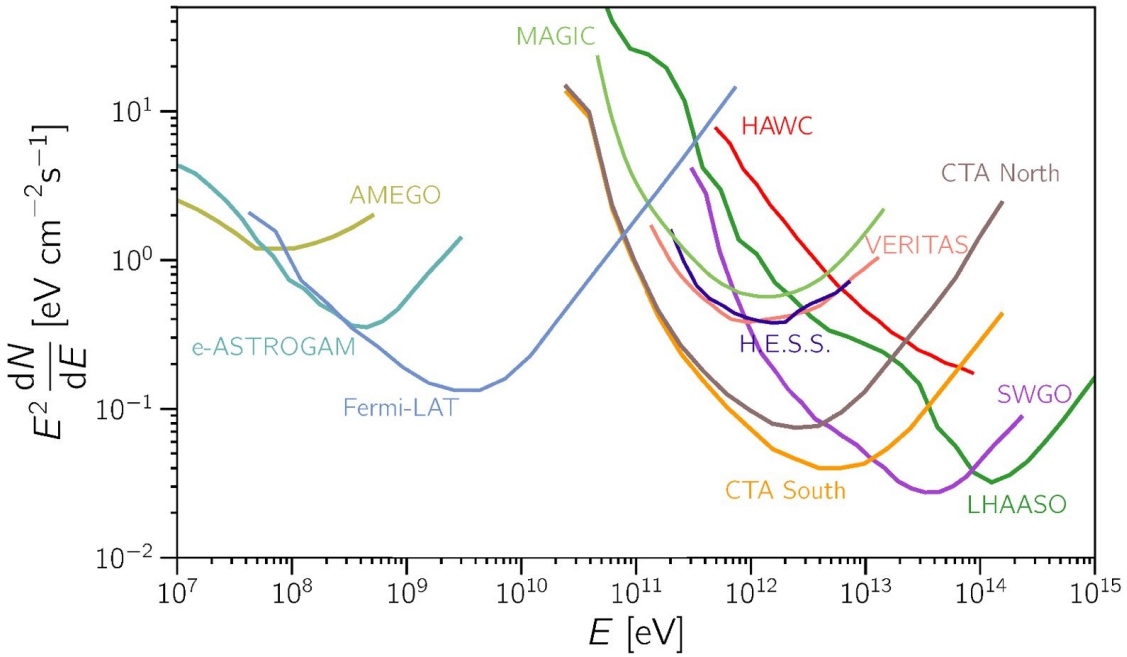

Figure 1.3: Detection sensitivities of various gamma-ray telescopes as a function of energy. For details, see Alves Batista and Saveliev [2021].

will have an effective area that is an order of magnitude larger than that of Fermi at GeV energies [Buckley and Team, 2022]. One of the prime research goals for APT is to explore the thermal DM particles across their entire natural range of masses and annihilation cross sections. It also plans to achieve rapid, all-sky detection and precise localization of GRBs and other gamma-ray transients, including gravitational wave (GW) counterparts [Buckley et al., 2021]. APT aims to detect gamma rays ranging from energies of 0.3 MeV to 1 TeV. Additionally, the Antarctic Demonstrator for APT (ADAPT), a balloon-based experiment, is set to test and validate the instrument concept inherent to the APT. ADAPT is a prototype mission for the larger space-based APT mission. It's designed to test the major components that will be used in the APT mission. ADAPT will operate during a roughly 30-day flight in Antarctica, its findings and operational insights will likely inform and optimize the design and objectives of the APT mission. The comparison of the telescope acceptance of APT, ADAPT, and

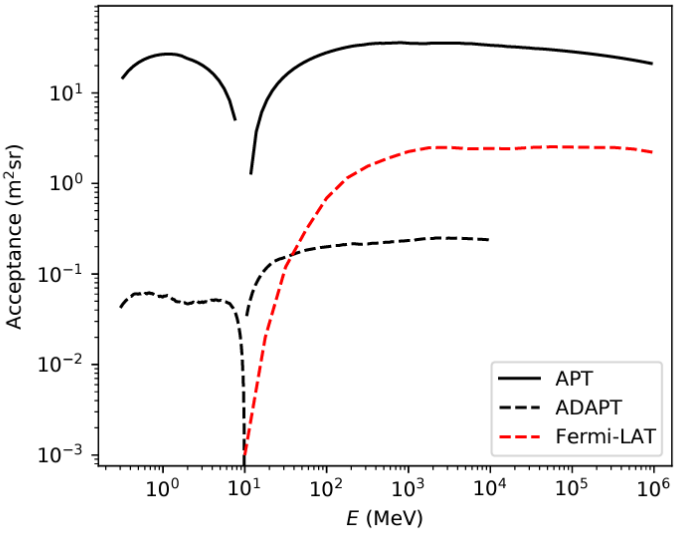

Figure 1.4: The acceptance values of Fermi, ADPAT and APT [Alnussirat et al., 2021].

Fermi is shown in Figure 1.4.

- **Imaging Atmospheric Cherenkov Telescopes (IACTs)**: IACTs are a type of ground-based observatory designed primarily to detect very high-energy gamma rays. These gamma rays shed light on astrophysical phenomena such as supernova remnants, active galactic nuclei (AGN), and pulsars. When a high-energy gamma ray photon strikes the Earth's atmosphere, it triggers a shower of secondary particles. These particles, traveling faster than light in the atmosphere, emit a type of blue light called Cherenkov radiation. IACTs are engineered to capture these brief flashes. The telescopes utilize large parabolic or spherical mirrors that gather and focus the Cherenkov light onto a camera. This distribution of light provides an image of the shower, revealing the direction and energy of the original gamma ray. Many modern IACT systems deploy multiple telescopes in an array, enhancing the observation capabilities. Representative IACT observatories include H.E.S.S. in Namibia [H. Abdallah, 2016], MAGIC on the Canary Island of La Palma [MAGIC Collaboration, 2016], and

VERITAS in Arizona [S. Archambault, 2017], USA, and the Cherenkov Telescope Array (CTA) [A. Acharyya, 2021]. These telescopes have significantly contributed to our understanding of the very high-energy universe, offering insights into the universe's most energetic processes.

- **Water Cherenkov Telescope**: Another type of telescope for detecting Cherenkov radiation is water Cherenkov telescopes such as The High Altitude Water Cherenkov Observatory (HAWC) [A.U. Abeysekara, 2018] and Large High Altitude Air Shower Observatory (LHAASO) [Cao et al., 2022]. HAWC is located at an altitude of over 4,100 meters above sea level on the Sierra Negra volcano near Puebla, Mexico. Similarly as in the case of IACT, when high-energy cosmic or gamma rays make contact with the Earth's atmosphere, they generate air showers of secondary particles. As some of these particles traverse through the water in the tanks at speeds surpassing the speed of light in water, they emit the so-called Cherenkov radiation. HAWC predominantly observes gamma rays and cosmic rays in the 500 GeV $\sim$ 100 TeV energy spectrum. In contrast, LHAASO is located on the Haizi Mountain in Sichuan, China, at an altitude of about 4,410 meters. LHAASO has the capacity to observe an expansive range of energies, spanning from 1 TeV to 1 PeV and even beyond.

- **Medium Energy Gamma-ray Telescope**: In lower energies close to X-rays, we have space-based gamma-ray observatories such as All-sky Medium Energy Gamma-ray Observatory (AMEGO) [Kierans, 2020] and e-ASTROGAM [A. De Angelis, 2017]. They aim to cover the medium-energy gamma-ray range between MeV to GeV, bridging the gap between current hard X-ray observatories and high-energy gamma-ray detectors.

1.2.2 Promising Locations for Detecting Dark Matter Signals

The Galactic Center: Signal and Backgrounds

The Navarro-Frenk-White (NFW) profile is a model that characterizes the distribution of DM in halos based on N-body cosmological simulations of structure formation in the universe [Navarro et al., 1996, 1997]. The profile is mathematically represented as

$$\rho(r) = \frac{\rho_s}{\left(\frac{r}{r_s}\right)^{\gamma}\left(1+\frac{r}{r_s}\right)^{3-\gamma}}, \tag{1.12}$$

where $\rho(r)$ denotes the density at a given radius r from the galaxy center, ρ_s is the characteristic density, r_s is the scale radius, and γ gives the inner slope of the profile. The NFW profile exhibits a central cusp where the density tends to infinity as r approaches zero. The NFW profile has been observed to be a good fit for simulated halos across a wide range of halo masses and cosmological scenarios [Gnedin et al., 2011, 2004, Governato et al., 2012].

We can estimate the flux of DM annihilation products by integrating the annihilation rate and the spectrum produced per annihilation over the volume V of the region observed:

$$\frac{dN_\gamma}{dE_\gamma} = \int \frac{d\Gamma_{XX}}{dV}\frac{dN_\gamma}{dE_\gamma}\bigg|_{\text{ann}}\frac{dV}{4\pi d^2} \tag{1.13}$$

$$= \frac{\langle\sigma v\rangle}{8\pi m_X^2}\frac{dN_\gamma}{dE_\gamma}\bigg|_{\text{ann}}\int_{\Delta\Omega}\int_{\text{los}}\rho_X^2\, dl\, d\Omega \tag{1.14}$$

$$= \frac{\langle\sigma v\rangle}{8\pi m_X^2}\frac{dN_\gamma}{dE_\gamma}\bigg|_{\text{ann}} J(\Delta\Omega),$$

where the density of the annihilation rate Γ_{XX} is given by

$$\frac{d\Gamma_{XX}}{dV} = \frac{\langle\sigma v\rangle\rho_X^2}{2m_X^2} \tag{1.15}$$

where $\langle\sigma v\rangle$ is the annihilation cross section, m_X is the mass of the DM particle, ρ_X is the DM

particle volume density, dN_γ/dE_γ is the annihilation spectrum, d is the distance to where the annihilation happens, V is the volume where annihilation happens, l is the line-of-sight, Ω is the solid angle. Here we consider the case where the DM particle X annihilates with itself.

The quantity $J(\Delta\Omega)$, known as the J-factor, encompasses the distribution of the DM within a solid angle $\Delta\Omega$ and is defined as

$$J(\Delta\Omega) = \int_{\Delta\Omega}\int_{\text{los}} \rho_X(l,\Omega)^2 \, dl \, d\Omega. \tag{1.16}$$

If one considers an NFW profile to describe the DM distribution in the Milky Way, the highest J factor will correspond to the center of the Galaxy, the closest of which to Earth would be the center of the Milky Way, the Galactic Center.

We can estimate the emission from DM annihilation near the Galactic Center using [Hooper, 2022]

$$F_\gamma \approx 3.6\times10^{-8}\,\text{cm}^{-2}\text{s}^{-1} \times \left(\frac{\langle\sigma v\rangle}{2.2\times10^{-26}\,\text{cm}^3/\text{s}}\right)\left(\frac{\int \frac{dN_\gamma}{dE_\gamma}dE_\gamma}{10}\right)\left(\frac{100GeV}{m_X}\right)^2. \tag{1.17}$$

Here we've taken $r_s \approx 20$kpc, with $\gamma = 1$, and have normalized the NFW profile such that the density of the DM at $r = 8.25$ kpc to 0.4 GeV/cm^3 [Bovy and Tremaine, 2012]. We also integrate the distribution within $\Delta\Omega = 10^\circ$ around the Galactic Center. If we further take into account the sensitivity of the Fermi telescope, we can estimate the rate of the detected DM annihilation products:

$$N_\gamma = F_\gamma \times A \times f \approx 2000\,\text{yr}^{-1}, \tag{1.18}$$

where $A \approx 8500\,\text{cm}^2$ is the effective area of the Fermi telescope, and $f \approx 20\%$ is the sky fraction [Ajello and W. B. Atwood, 2021]. If we consider a wider range of γ from 0.7 $\sim$

1.4 suggested by various numerical simulations [Gnedin et al., 2011, 2004, Governato et al., 2012], the rate can range from $670 \sim 10000$ yr^{-1} [Hooper, 2022].

Despite having the most luminous DM signal in theory, the Galactic Center also suffers from contamination by numerous sources in the gamma-ray band. This includes:

- **Pion production**: When high-energy cosmic-ray protons collide with ambient protons or nuclei in the interstellar medium (ISM), they can produce charged and neutral pions (π^+, π^-, and π^0). The neutral pions decay almost immediately after their formation, predominantly into two gamma-ray photons through the process of $\pi^0 \to \gamma + \gamma$. The charged pions decay into electrons, positions, and neutrinos. In order to produce one or more pions, a cosmic-ray proton colliding with a proton at rest must have a total energy in excess of $E_p > m_p + 2m_\pi + \frac{m_\pi^2}{2m_p} \approx 1.2$ GeV, where E_p is the kinetic energy of the cosmic-ray protons, and m_p, m_π are the rest mass of proton and pion.

- **Bremsstrahlung**: When a charged particle, such as an electron, is decelerated or deflected by another charged particle, such as an atomic nucleus, the electron loses energy through radiation in X-rays or gamma-rays [Bethe and Heitler, 1934]. This change in kinetic energy gets emitted as a photon. Bremsstrahlung frequently serves as the primary cooling method for cosmic-ray electrons in the ∼MeV-GeV range.

- **Inverse Compton scattering (ICS)**: ICS occurs when a relativistic electron scatters off a low-energy photon, transferring a fraction of its energy to the photon. ICS plays a significant role in generating gamma rays. Within our galaxy, cosmic-ray electrons scattering off the CMB or interstellar light can produce gamma rays via this mechanism. The detailed spectrum from ICS depends on the energies of the particles involved. In the Thomson regime, $E_e \ll m_e^2/\epsilon_\gamma$, where ϵ_γ is the energy of a target photon, such scattering causes the electrons to lose only a small fraction of their energy. In the Klein–Nishina regime, $E_e \gg m_e^2/\epsilon_\gamma$, ICS transfers an order one fraction of the electron's energy to an individual photon [Hooper, 2022].

- **Point Sources**: Gamma-ray point sources near the Galactic center can also affect DM searches. These point sources include supernova remnants, pulsars, and the supermassive black hole in the center of the Milky Way, Sagittarius A* [Saurabh et al., 2022].

Constructing a detailed and accurate model for the Galactic diffuse emission is very challenging. Current models are derived from gas maps and cosmic-ray spectra measured locally. The detailed morphology of the background is yet to be accurately described [Hooper, 2022].

The observation of the Galactic Center in the last decade revealed a gamma-ray excess, taking all the background sources above into account. The spectrum and angular distribution of this signal are consistent with a scenario in which $m_X = 40 - 70\,\mathrm{GeV}$ and $\sigma v = 10^{-26}\mathrm{cm}^3/\mathrm{s}$, considering the $b\bar{b}$ annihilation channel [Ackermann, 2017, Albert, 2017].

DM Constraints from Dwarf Galaxies

In the previous section, we showed that the center of the Milky Way should yield the most luminous signal from DM annihilation. However, numerous sources proximate to the Galactic center also emit gamma rays. They contaminate the signals attributed to DM in a non-trivial way. This contamination poses a significant challenge to the clear detection and analysis of DM annihilation signals in this region.

On the contrary, dwarf galaxies provide a unique site for DM annihilation detection with much less contamination due to their low star formation rate. These dwarf galaxies reside in the largest subhalos of the Milky Way. Some of these galaxies are relatively bright, allowing them to be discovered decades ago, such as Draco, Ursa Minor, Sculptor, Fornax, etc. Others are more faint and were discovered more recently using state-of-the-art observations by cosmological surveys including the SDSS and the Dark Energy Survey (DES) [Bechtol et al., 2015, Drlica-Wagner, 2015, Koposov et al., 2015].

To estimate the DM annihilation signal from dwarf galaxies, we first need to estimate the J-factors. Such J-factors can be derived from spectroscopic observations of the line-of-sight velocities of bright stars in the dwarf galaxy [Martinez, 2015, Bonnivard et al., 2015]. Pace and Strigari [2019] have compiled a large sample of dwarf galaxies from a wide range of literature. They assume an NFW profile and fit the parameters of the DM potential from the spectroscopic data. They also calculated the J-factor over various solid angles. We adopt their dwarf galaxy catalog, more specifically, their measurements of J-factors within the radius of 0.5 degrees. The J-factors in our final assembled catalog range from $10^{16.4} - 10^{19.5}\,\mathrm{GeV}^2/\mathrm{cm}^5$. More details about the dwarf galaxy catalog will be described in Chapter 2.

If we take the maximum J-factors in our catalog, $10^{19.5}\mathrm{GeV}^2/\mathrm{cm}^5$, we can make a similar estimate of the flux of DM annihilation products from a dwarf galaxy:

$$F_\gamma \approx 2.7 \times 10^{-11}\,\mathrm{cm}^{-2}\mathrm{s}^{-1} \times \left(\frac{\langle\sigma v\rangle}{2.2 \times 10^{-26}\,\mathrm{cm}^3/\mathrm{s}}\right)\left(\frac{\int \frac{dN_\gamma}{dE_\gamma} dE_\gamma}{10}\right)\left(\frac{100\,\mathrm{GeV}}{m_X}\right)^2. \quad (1.19)$$

This gives an event rate of approximately 1.5 events per year in Fermi [Hooper, 2022] which is orders of magnitude fainter than the emission from the Galactic center.

Although dwarf galaxies suffer significantly less background contamination from their own components, such as stars, gas, etc, they still have backgrounds from extra-galactic sources. Taking these into account is important for understanding the observational potential of these dwarf galaxies:

- **The Isotropic Gamma-ray Background (IGRB)**: The IGRB refers to the diffuse extra-galactic gamma-ray radiation that appears to be distributed uniformly across the sky. It represents the aggregate emission from sources that are either too faint or too distant to be resolved by gamma-ray telescopes. Such sources often emit fewer than one photon on average during an observation, and their photon statistics are described by

a Poisson distribution, as the sources are too faint to show correlations [Malyshev and Hogg, 2011]. The IGRB spectrum can be well-explained by a combination of distant AGNs, blazars, star-forming galaxies, and start-burst galaxies [Pavlidou and Fields, 2002, Mauro, 2016].

- **Bright Blazars**: In addition to the IGRB, bright point sources, mostly bright blazars, also contribute to the extra-galactic gamma-ray background. This component of the gamma-ray background is fundamentally non-Poissonian in nature. To calculate the emission from these bright blazars, which isn't discussed in the original APT proposal, we need to take into account the blazar source count function, dP/dS. Given the source count function, we can calculate the probability of observing a given number of photons from point sources:

$$P(N_{\rm PS}) = \int_S \frac{dP}{dS} dS \, \frac{\langle N_{\rm PS} \rangle^{N_{\rm PS}} \, e^{-\langle N_{\rm PS} \rangle}}{N_{\rm PS}!}, \tag{1.20}$$

  The photon counts in sky pixels for these sources diverge from Poisson statistics due to correlations among photons from the same source. We don't consider correlation in time and treat the entire observation as a single time bin. The detailed source count function and calculations are described in Chapter 2.

- **Galactic Diffuse Emission**: Galactic diffuse emission refers to the pervasive emission of gamma rays that originate from processes which take place throughout our Milky Way galaxy. This emission is not associated with discrete point sources like individual stars or supernovae but arises from widespread interactions across the galactic plane and beyond, such as the interactions between cosmic-ray protons and electrons in the ISM, as previously mentioned in Section 1.2.2.

We perform detailed simulations considering the above background sources and discuss the potential of DM observation using APT (see Section 1.2.1) in Chapter 2. We combine

the background and the DM signals to calculate the probability of getting $N_{\rm tot}$ total number of events by summing all the possible combinations of signal $N_{\rm sig}$ and background $N_{\rm bg}$.

Our analysis reveals that APT would have the capability to efficiently detect gamma-ray emissions from numerous dwarf galaxies with pronounced clarity. More specifically, if the Galactic Center gamma-ray excess is generated by annihilaiting DM, APT would detect an average of 7 dwarf galaxies with a significance of at least 2σ, and 3 dwarfs with a significance of 5σ or greater. It will bring valuable insights for validating or ruling out the DM hypotheses associated with the persistent Galactic center gamma-ray excess.

1.2.3 Gamma-Ray Background in TeV Halos

Observations by the HAWC [Hooper et al., 2017, Linden et al., 2017, Abeysekara et al., 2017, 2020, Albert et al., 2020b], Milagro [Abdo et al., 2009, Linden and Buckman, 2018], and HESS [Abdalla et al., 2018b,a] telescopes have revealed that pulsars are surrounded by spatially extended "TeV halos" [Albert et al., 2021]. The multi-TeV gamma-ray emission that is associated with these halos is the result of ICS as mentioned in Section 1.2.2, and is powered by the rotational kinetic energy of the host pulsar [Sudoh et al., 2021]. These objects represent a new class of high-energy sources, which are responsible for a significant fraction of the Milky Way's TeV-scale gamma-ray emission.

The integrated energy budget for the resulting emission is consequently limited by the pulsar's initial rotational kinetic energy:

$$E_{\rm rot} = \frac{I\Omega^2}{2} = \frac{4\pi^2 M R^2}{5P^2}, \tag{1.21}$$

where M and R are the mass and radius of the neutron star, and P is the pulsar rotation period, which is a function of time, t.

Only a fraction of a given pulsar's total rotational kinetic goes into the gamma-ray

emission associated with a TeV halo. We define the efficiency η of a TeV halo as the fraction of the pulsar's rotational kinetic energy that goes into the production of TeV-scale gamma-rays:

$$\eta \equiv \frac{F_\gamma}{\dot{E}_{\rm rot}/4\pi d^2}, \tag{1.22}$$

where F_γ is the flux of the gamma-ray emission bewteen $0.1 - 100$ TeV, $\dot{E}_{\rm rot}$ is the time derivative of the pulsar's rotational kinetic energy, and d is the distance to the pulsar. We can determine the value of η by comparing the current spindown flux of a given pulsar, $\dot{E}_{\rm rot}/4\pi d^2$, from radio observations to the gamma-ray flux reported by the HAWC Collaboration. More details are described in Chapter 3.

From the measured abundance of pulsars and the efficiency with which they are observed to generate TeV halos, it can be shown that these objects dominate the diffuse TeV-scale emission that is observed along the plane of the Milky Way [Linden and Buckman, 2018, Aharonian and Atoyan, 2000, Fang and Murase, 2021]. On similar grounds, one can deduce that this class of sources must contribute significantly to the total IGRB, in particular at TeV-scale energies. In this sense, TeV halos appear to be an important means by which star formation leads to the production of very high-energy radiation.

In Chapter 3, we use the observed characteristics of the TeV halos detected by HAWC to estimate the TeV-scale gamma-ray emission from the TeV halo population in the Andromeda Galaxy (M31), as well as to calculate the contribution from this source class to the total IGRB. When determining the contribution of TeV halos to the IGRB, we consider attenuation effects and the EM cascades. Specifically, photons at the TeV scale can interact with the infrared background, producing electron-positron pairs. These pairs, in turn, generate photons with lower energy as they cool, primarily through ICS. For this calculation, we employ the γ-Cascade software [Blanco, 2019], which comprehensively simulates the impacts of pair production, ICS, and synchrotron losses.

We predict that the gamma-ray emission from the TeV halos in M31 will be detectable in

the future by the CTA. Furthermore, we predict that the TeV halos distributed throughout the observable universe should be responsible for up to ∼20% of the IGRB at 100 GeV, and perhaps even a larger fraction at TeV-scale energies.

1.3 Strong Lensing: Electromagnetic and Gravitational Waves

Lensing of EM waves is a phenomenon predicted by Einstein's general theory of relativity. When a massive object, such as a massive galaxy or galaxy cluster, lies between a distant light source and the observer, it can distort the light from that source, acting much like a lens. This effect is particularly pronounced in cases of strong lensing, where the gravitational field of the intervening mass is so intense that it can produce multiple, highly magnified, and often distorted images of the background source. For example, Figure 1.5 shows a case where the emission of a bright quasar has been distorted into 4 distinct images by a foreground galaxy. Observing such lensing events provides astronomers with a unique tool to probe the universe, measure cosmological parameters [Turner et al., 1984, Cao et al., 2012, Liu et al., 2020b], and study the nature of DM halos [Davis et al., 2003, Chae, 2003, Chae and Mao, 2003, Sohn et al., 2017, Smail et al., 1994, Schneider, 1996, Keeton and Madau, 2001, Oguri et al., 2002, Hoekstra et al., 2004, Corless and King, 2007, Massey et al., 2010, Collett, 2015, Diego et al., 2018, Meneghetti et al., 2020]. In particular, one of the most basic properties that one can probe with strong lensing are the masses of the DM halos, as traced by their velocity dispersions, σ. For example, Davis et al. [2003] studied 13 lenses provided by the Cosmic Lens All-Sky Survey/Jodrell Very Large Array Astrometric Survey data to constrain the characteristic velocity dispersion distribution of elliptical galaxies, σ_*, to $168 \leq \sigma_* \leq 200$ kms^{-1} at 68% confidence level. Similarly, Chae [2005] selected ∼15 multiply-imaged systems from the same surveys and constrained σ_* to ∼80 km/s for the case of SDSS, and ∼190 km/s for the case of SSRS2. In addition, the time delay between lensed images can be used to investigate the density profile of the lens halos as well as the Hubble

Figure 1.5: Quasar HE 0435-1223 multiply lensed by foreground galaxy discovered by H0LiCOW Survey [Suyu et al., 2017].

parameter, H_0 [Oguri et al., 2002, Li et al., 2012]. In addition to the properties of the lenses, the observational samples of lensed systems also depend on the properties of the sources, and in particular, the rate density (for transient sources such as Type Ia supernovae) of the sources as a function of mass and redshift. These samples are also sensitive to observational selection effects, which can cause dramatic differences between the observed and intrinsic distributions.

Like EM waves, gravitational waves (GWs) can also be strongly lensed by massive objects between the observer and the binary black holes (BBHs) merger event, and form multiple 'images'. These 'images' appear as distinct GW events with similar sky positions but with different magnifications and arrival times. The magnification changes the overall amplitude of the signal, biasing the inference of the luminosity distance and, as a consequence, the source-frame masses.

In this thesis, we focus on lenses at the scale of massive elliptical galaxies, since these are expected to be the dominant strong lenses. For these systems, the Schwarzschild radius

is significantly larger than the wavelength of the GWs emitted by stellar-mass BBH, and we can therefore adopt the geometric optics limit in which GWs are treated as rays and the wave nature of the GWs is not emphasized (e.g. diffraction of GWs is not considered in this case). We also consider BBH merger events as our sources whose event rate can be derived from cosmic star formation rate. The detailed calculation is described in Section 4.2.2 in Chapter 4.

Strong lensing of GWs will provide a novel and independent way to study the matter distribution in the universe. Compared to EM studies, GW lensing has several advantages:

- **No Dust Extinction**: GWs do not suffer from dust extinction or anything else that might compromise the signal; GWs propagate directly from source to observer without any intervening impact (except for the curvature of space-time). The correction of dust attenuation in EM observation is a challenging and non-trivial task due to the uncertainty in dust physics [Calzetti, 1997, Calzetti et al., 2000].

- **Clean All-Sky Survey**: Comparing to EM surveys, where it is difficult to guarantee both uniform depth and breadth even for surveys in the radio band [Adams and van Leeuwen, 2019], GW detections "hear" lensing events happening on the entire sky simultaneously, allowing us to study a clean lensing sample with well-understood and characterized selection effects.

- **Well-Understood Selection Effect**: Unlike EM sources which can be obscured or time variable, the noise power spectrum of GW detectors can be measured and the source properties are well characterized, further reducing selection effects on the lensing sample.

There are several useful observables in GW lensing that can serve as useful cosmological probes:

- **Lensing Event Rate**: A fundamental aspect of statistical lensing is the rate of strong lensing, which depends both on the properties of the lenses and sources. Several studies have provided theoretical predictions for this rate. For present 2nd-generation (2G) advanced Laser Interferometer Gravitational-Wave Observatory (aLIGO), the strong lensing event rate was found to be up to $0.5 - 1\,\mathrm{yr}^{-1}$ (Oguri [2018], Li et al. [2018], Yang et al. [2021]). These results are consistent with the current non-detection of lensing events during the first two observing runs [Hannuksela et al., 2019, McIsaac et al., 2020, Kim et al., 2020] and the first half of the third one [Abbott et al., 2021].[2] The chances of strong lensing will increase with future sensitivity upgrades, as a higher redshift implies a larger probability of lensing. 2G detectors are expected to be upgraded beyond design sensitivity (A+), which will allow the detection of GW source out to redshift of $z \sim 3$ [see Fig. 3 of The LIGO Scientific collaboration, 2019b]. Future 3rd-generation (3G) instruments, such as Einstein Telescope (ET) and Cosmic Explorer (CE), will be able to detect BBH sources with masses up to $10^4 M_\odot$ and at redshifts as high as $z \sim 100$ [see Fig. 2 left panel in Maggiore et al., 2020]. The enhancement in the detectable cosmological volume will greatly increase the lensing event rate, to as high as $40–10^3\,\mathrm{yr}^{-1}$ for ET [Piórkowska et al., 2013, Biesiada et al., 2014, Ding et al., 2015, Oguri, 2018, Li et al., 2018]. The more detailed calculations are described in Section 4.2.4 in Chapter 4.

- **Magnification**: A lensed GW event would undergo magnification, which would alter the amplitude of the detected signal. The magnification factor depends on the lens properties and the relative alignment of the source, lens, and observer. In most cases,

2. Dai et al. [2020] and Liu et al. [2020a] have found an intriguing pair, GW170104–GW170814, with masses, sky positions, and phases a priori consistent with the strong lensing hypothesis. However, other properties of the pair such as the large time delay and image type configuration make this association unlikely [Dai et al., 2020, Liu et al., 2020a]. The analysis of Abbott et al. [2021] confirms that the inclusion of selection effect and source and lens population priors drastically reduce the likelihood that this is a lensing event.

we will see two separate GW events coming from the same BBH merger event. These two events correspond to the primary (the brightest image, or the one with the highest magnification) and the secondary image (the second brightest image) of the lens system. The magnification distribution of the lensing events is another interesting observable that may reflect the properties of the lens population.

- **Time Delay**: A lensed GW event can also be split into multiple GW signals, each arriving at slightly different times due to different path lengths, creating a time delay between the signals. We note that the time delay is proportional to σ^4 where σ is the velocity dispersion of the lens galaxies. In addition, GW facilities have exquisite time resolution (to fractions of a second) and is thus able to measure time delays in high precision. Therefore, time delay distribution is potentially a very ideal cosmological probe that is highly sensitive to the lens population.

In Chapter 4, we explore the capabilities of current and future GW detectors to constrain both the properties of the lens galaxies and the source population. We first compute the lensing event rates for aLIGO, A+, ET, and CE and further perform Monte Carlo (MC) sampling to simulate the gravitational lensing of BBHs and calculate the lensing properties including the time delay and magnification distributions. We then estimate our ability to constrain the typical lens velocity dispersion which gives crucial insights into the DM distribution of these massive systems assuming different observation duration times and detector sensitivities. Furthermore, since the strong lensing event rate of GWs is also affected by the number of sources in the universe, we show that this information can be used as a complementary probe of the population of BBH mergers. Both detection and non-detection of GW lensing events will provide insights on the formation channels of these binaries as well as the star formation rate (SFR) and delay-time distributions.

CHAPTER 2

THE DARK MATTER DISCOVERY POTENTIAL OF THE ADVANCED PARTICLE-ASTROPHYSICS TELESCOPE (APT)

2.1 Introduction

For decades, the most widely studied DM candidates have been thermal relics of the early universe [Bertone and Hooper, 2018]. Such particles were motivated by the realization that, if they had weak-scale masses and couplings, they would freeze out of equilibrium with an abundance that is approximately equal to that of the measured DM density – a fact frequently referred to as the "WIMP miracle." Many WIMP models, however, have since been ruled out by the null results of direct [Aalbers et al., 2022, Aprile et al., 2023] and indirect [Albert et al., 2017, Calore et al., 2022, Bergstrom et al., 2013, Aghanim et al., 2020] searches. In light of this progress, some have argued that the WIMP paradigm is now disfavored. Simultaneously, it is not difficult to identify WIMP models which continue to be consistent with all existing constraints (for a discussion, see Ref. [Bertone and Tait, 2018]).

The WIMP paradigm has been bolstered in recent years by the signal known as the Galactic Center Gamma-Ray Excess, as identified within the data collected by the Fermi Gamma-Ray Space Telescope [Cholis et al., 2021, Di Mauro, 2021] (for early work, see Refs. [Goodenough and Hooper, 2009, Hooper and Goodenough, 2011, Hooper and Linden, 2011, Abazajian and Kaplinghat, 2012, Hooper and Slatyer, 2013, Gordon and Macias, 2013, Daylan et al., 2016, Calore et al., 2015, Ajello et al., 2016]). The spectrum and angular distribution of this excess are each consistent with those predicted from annihilating DM. In particular, the measured characteristics of this signal are well fit by DM particles with a mass of $m_X \sim 35-60\,\text{GeV}$ and an annihilation cross section of $\langle \sigma v \rangle \sim (1-3) \times 10^{-26}\,\text{cm}^3/\text{s}$ (for the case of annihilations to $b\bar{b}$). This agrees remarkably well with the annihilation cross section expected of a thermal relic, $\langle \sigma v \rangle \approx 2.2 \times 10^{-26}\,\text{cm}^3/\text{s}$ (see, for example, Ref.

[Steigman et al., 2012]).

If the Galactic Center Gamma-Ray Excess is generated by annihilating DM, an analogous signal should be produced from dwarf galaxies (for a review, see Ref. [Strigari, 2018]). Gamma-ray observations of the Milky Way's dwarf galaxy population thus have the potential to confirm or rule out DM interpretations of the Galactic Center excess and, more broadly, to test the WIMP paradigm itself. The most recent such analysis by the Fermi Collaboration studied six years of data from the directions of 45 dwarf galaxies (and dwarf galaxy candidates), allowing them to rule out DM annihilation cross sections greater than $\langle \sigma v \rangle \sim 2.2 \times 10^{-26}\,\mathrm{cm}^3/\mathrm{s}$ for masses up to $m_X \sim 50\,\mathrm{GeV}$ (again, for the case of annihilations to $b\bar{b}$) [Albert et al., 2017]. More recently, Di Mauro *et al.* used 14 years of Fermi data to study a sample of 22 dwarf galaxies, producing similar constraints [Di Mauro et al., 2022]. Perhaps more interesting, these analyses also identified what could be hints of a DM annihilation signal. In particular, Ref. [Di Mauro et al., 2022] reports the presence of gamma-ray excesses from the dwarf galaxies Reticulum II, Sculptor, and Tucana II at a level of TS $\approx$ 11, 9, and 6, respectively (for the case of $m_X = 50\,\mathrm{GeV}$), where TS is the log-likelihood test statistic. Overall, this stacked analysis favors the presence of annihilating DM over the null hypothesis at a level of TS $\approx$ 11, corresponding to a local significance of 3.0σ [Di Mauro et al., 2022] (see also, Refs. [Drlica-Wagner et al., 2015, Hooper and Linden, 2015, Bhattacharjee et al., 2019]).

Whereas gamma-ray studies of the Galactic Center are currently limited by systematic uncertainties associated with bright and poorly understood backgrounds, searches for gamma rays from dwarf galaxies are statistically limited. Future observations of the Milky Way's dwarf galaxy population with a large-acceptance, space-based gamma-ray telescope could thus significantly increase our sensitivity to DM and clarify the origin of the Galactic Center Gamma-Ray Excess.

In this chapter, we evaluate the sensitivity of the proposed Advanced Particle-astrophysics

Dwarf Galaxy	Distance (kpc)	$log_{10}J(0.5$	l	b	Included in Fig.1
Canes Venatici I	210.0 ± 6.0	$17.42^{+0.17}_{-0.15}$	74.30	79.83	No
Carina	105.6 ± 5.4	$17.83^{+0.10}_{-0.09}$	260.11	-22.22	Yes
Draco	76.0 ± 6.0	$18.83^{+0.12}_{-0.12}$	86.37	34.71	Yes
Fornax	147.0 ± 9.0	$18.09^{+0.10}_{-0.10}$	237.24	-65.67	Yes
Leo I	258.2 ± 9.5	$17.64^{+0.14}_{-0.12}$	225.98	49.11	No
Leo II	233.0 ± 15.0	$17.76^{+0.22}_{-0.18}$	220.16	67.23	Yes
Sculptor	83.9 ± 1.5	$18.58^{+0.05}_{-0.05}$	287.70	-83.15	Yes
Sextans	92.5 ± 2.2	$17.73^{+0.13}_{-0.12}$	243.50	42.27	Yes
Ursa Minor	76.0 ± 4.0	$18.75^{+0.12}_{-0.12}$	104.98	44.81	Yes
Aquarius II	107.9 ± 3.3	$18.27^{+0.66}_{-0.58}$	55.11	-53.01	No
Boötes I	66.0 ± 3.0	$18.17^{+0.31}_{-0.29}$	358.10	69.64	Yes
Canes Venatici II	160.0 ± 7.0	$17.82^{+0.47}_{-0.47}$	113.57	82.70	Yes
Carina II	37.4 ± 0.4	$18.25^{+0.55}_{-0.54}$	269.98	-17.14	No
Coma Berenices	42.0 ± 1.5	$19.00^{+0.36}_{-0.35}$	241.86	83.61	Yes
Draco II	20.0 ± 3.0	$18.93^{+1.39}_{-1.70}$	98.32	42.88	No
Grus I	120.2 ± 11.1	$16.88^{+1.51}_{-1.66}$	338.65	-58.24	No
Hercules	132.0 ± 6.0	$17.37^{+0.53}_{-0.53}$	28.73	36.86	Yes
Horologium I B	87.0 ± 8.0	$18.79^{+0.90}_{-0.86}$	271.38	-54.74	No
Leo IV	154.0 ± 5.0	$16.40^{+1.01}_{-1.15}$	265.46	56.51	Yes
Leo V	173.0 ± 5.0	$17.65^{+0.91}_{-1.03}$	261.86	58.53	No
Pegasus III	215.0 ± 12.0	$18.30^{+0.89}_{-0.97}$	69.85	-41.83	No
Pisces II	183.0 ± 15.0	$17.30^{+1.00}_{-1.09}$	79.21	-47.11	No
Reticulum II B	32.0 ± 2.0	$18.88^{+0.39}_{-0.37}$	266.30	-49.74	No
Segue 1	23.0 ± 2.0	$19.12^{+0.49}_{-0.58}$	220.48	50.41	Yes
Tucana II B	57.5 ± 5.3	$19.02^{+0.58}_{-0.53}$	328.09	-52.32	No
Ursa Major I	97.3 ± 5.85	$18.26^{+0.29}_{-0.27}$	159.36	54.43	No
Ursa Major II	34.7 ± 2.1	$19.44^{+0.41}_{-0.39}$	152.46	37.44	Yes
Willman 1	38.0 ± 7.0	$19.53^{+0.50}_{-0.50}$	158.57	56.78	Yes
Cetus	780.0 ± 40.0	$16.28^{+0.20}_{-0.19}$	156.47	-78.53	No
Eridanus II	366.0 ± 17.0	$17.28^{+0.34}_{-0.31}$	249.78	-51.64	No
Leo T	407.0 ± 38.0	$17.49^{+0.49}_{-0.45}$	214.85	43.66	No

Table 2.1: The dwarf galaxies are considered in this analysis. Note that we have excluded Fornax from our main analysis (due to it containing globular clusters [Pace et al., 2021]). The J-factor estimate are from Ref. [Pace and Strigari, 2019] and are given in units of $\mathrm{GeV}^2/\mathrm{cm}^5$.

Telescope (APT) Alnussirat et al. [2021], Buckley et al. [2021] to DM annihilating in the dwarf galaxies of the Milky Way.[1] To this end, we perform a stacked analysis of simulated data from the directions of 30 Milky Way dwarf galaxies, assessing the constraints on annihilating DM that could be achieved by such an instrument. We then estimate the projected sensitivity of APT to DM in a scenario motivated by the Galactic Center Gamma-Ray Excess. If the Galactic Center Excess is generated by annihilating DM, we find that APT will be able to detect gamma-ray signals from several dwarf galaxies at high significance. We conclude that such a telescope would be able to definitively confirm or rule out DM interpretations of the long-standing Galactic Center Gamma-Ray Excess.

2.2 Dark Matter Annihilation in Milky Way Dwarf Galaxies

The gamma-ray signal from annihilating DM can be calculated as follows:

$$\begin{aligned}\frac{dN_\gamma}{dE_\gamma} &= \frac{\langle\sigma v\rangle}{8\pi m_X^2}\left.\frac{dN_\gamma}{dE_\gamma}\right|_{\rm ann}\int_{\Delta\Omega}\int_{\rm los}\rho_X^2\,dl\,d\Omega \\ &= \frac{\langle\sigma v\rangle}{8\pi m_X^2}\left.\frac{dN_\gamma}{dE_\gamma}\right|_{\rm ann} J(\Delta\Omega),\end{aligned} \tag{2.1}$$

where $\langle\sigma v\rangle$ is the thermally-averaged DM annihilation cross section, m_X is the mass of the DM particle, and $dN_\gamma/dE_\gamma|_{\rm ann}$ is the spectrum of gamma rays produced per annihilation. The J-factor, $J(\Delta\Omega)$, is defined as the square of the DM density, ρ_X, integrated over a solid angle, $\Delta\Omega$, and along the line-of-sight, l. The J-factor is defined in the same way as in Equation 1.16. The DM distributions of the Milky Way dwarf galaxies (and their corresponding J-factors) are constrained by spectroscopic measurements of stellar velocities. In our main analysis, we have used the J-factors provided by Pace and Strigari in Ref. [Pace and Strigari, 2019].

1. The proposed APT [Alnussirat et al., 2021, Buckley et al., 2021] is planned to follow the ADAPT (Antarctic Demonstrator for the Advanced Particle-astrophysics Telescope) mission, which is scheduled for a 30 day, sub-orbital flight in 2025. For more details, see `https://adapt.physics.wustl.edu/`.

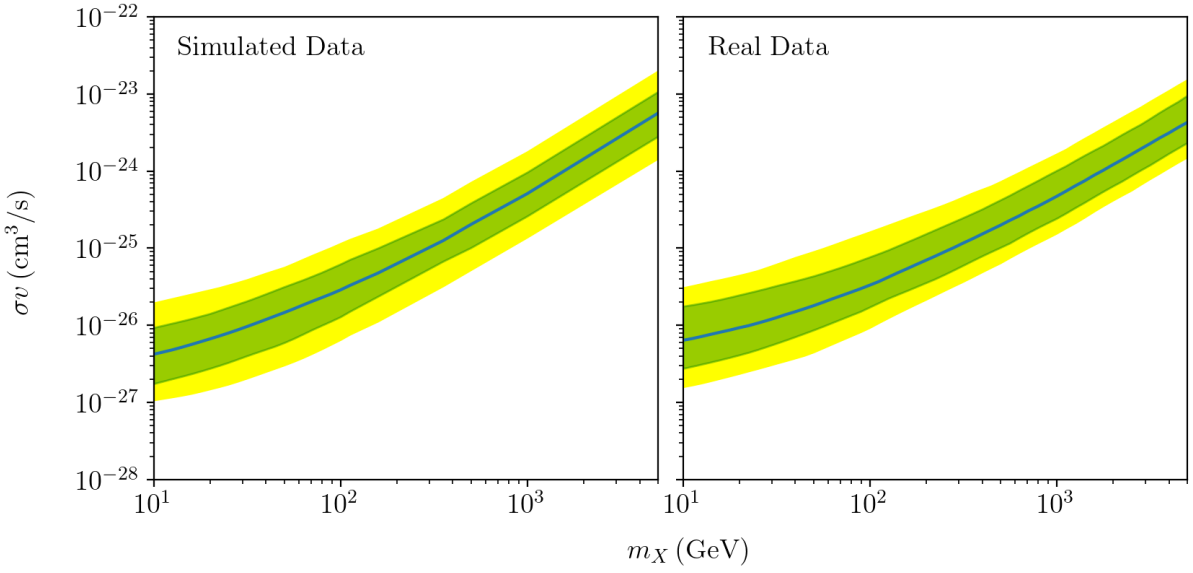

Figure 2.1: A comparison of the constraints on the DM annihilation cross section (to $b\bar{b}$) attained from four years of simulated (left) or real (right) Fermi data, from the directions of 15 dwarf galaxies. The solid lines and the surrounding green and yellow bands denote the median constraint and the range of constraints attained in 68% and 95% of the simulated realizations, respectively. In the right frame, we show the results from Ref. [Ackermann et al., 2014], which were derived from four years of real Fermi data. The similarity between the simulated and real constraints demonstrates that our model provides an adequate description of the relevant backgrounds.

Dwarf galaxies are attractive targets for DM searches due to their low astrophysical backgrounds. As gamma-ray telescopes become larger and more capable of detecting fainter sources, however, even modest backgrounds will become increasingly important. In our analysis, we have adopted a background model that consists of three components: 1) the gamma rays associated with unresolved point sources, 2) the background of isotropically distributed gamma rays, and 3) the diffuse emission associated with cosmic ray interactions in the interstellar medium. Note that these backgrounds do not originate from the dwarf galaxies themselves, but rather are associated with emission that is coincidentally produced along the lines-of-sight to these systems. Although millisecond pulsars in dwarf galaxies could potentially represent another background for DM searches, the gamma-ray fluxes arising from such objects are not expected to significantly impact such efforts [Winter et al., 2016].

Possible exceptions are the Fornax and Sagittarius dwarf galaxies, which are known to contain globular clusters [Pace et al., 2021, Evans et al., 2023], making it more likely that they harbor a significant population of millisecond pulsars. To be conservative, we have not included Fornax or Sagittarius in our main analysis.

Far away from the Galactic Plane, the gamma-ray emission from unresolved point sources is dominated by blazars, and we take the source count distribution of this population to follow the triply-broken power-law model described in Ref. [Marcotulli et al., 2020]. For each simulated observation of a dwarf galaxy, we draw from this distribution (up to sources as bright as $S \sim 10^{-6}\,\mathrm{ph\,cm^{-2}\,s^{-1}}$ and extrapolated down to $S \sim 10^{-13}$, where S is the photon flux integrated above 0.1 GeV) to determine whether any such sources are present in that direction and, if so, their fluxes. We take the spectral shape of each blazar to be the same as that of the measured extragalactic gamma-ray background [Ackermann et al., 2015b]. Note this component of the gamma-ray background is fundamentally non-Poissonian in nature. The integral of this distribution constitutes approximately 60% of the total extragalactic gamma-ray background. We take the remaining 40% of this background to be isotropic, arising from diffuse mechanisms or from sources that produce no more than one photon in the data sets we will consider here. For the Galactic diffuse emission, we adopt the model $gll iemv05.fit$, as provided in Ref. [Ackermann et al., 2014]. Unlike contributions from unresolved blazars and the isotropic background, the spectrum and intensity of the Galactic diffuse emission depends on the location of a given dwarf galaxy on the sky.

Once we have determined the total gamma-ray flux from the direction of a given dwarf galaxy, we integrate over each energy bin and multiply by the instrumental exposure (using the acceptance evaluated at the average energy of that bin) to determine the mean number of photons that are observed in each energy bin and from within 0.5° of the dwarf galaxy's center. We then draw from a Poisson distribution in each bin to determine the number of photons that are observed in that realization, and use this information to calculate the

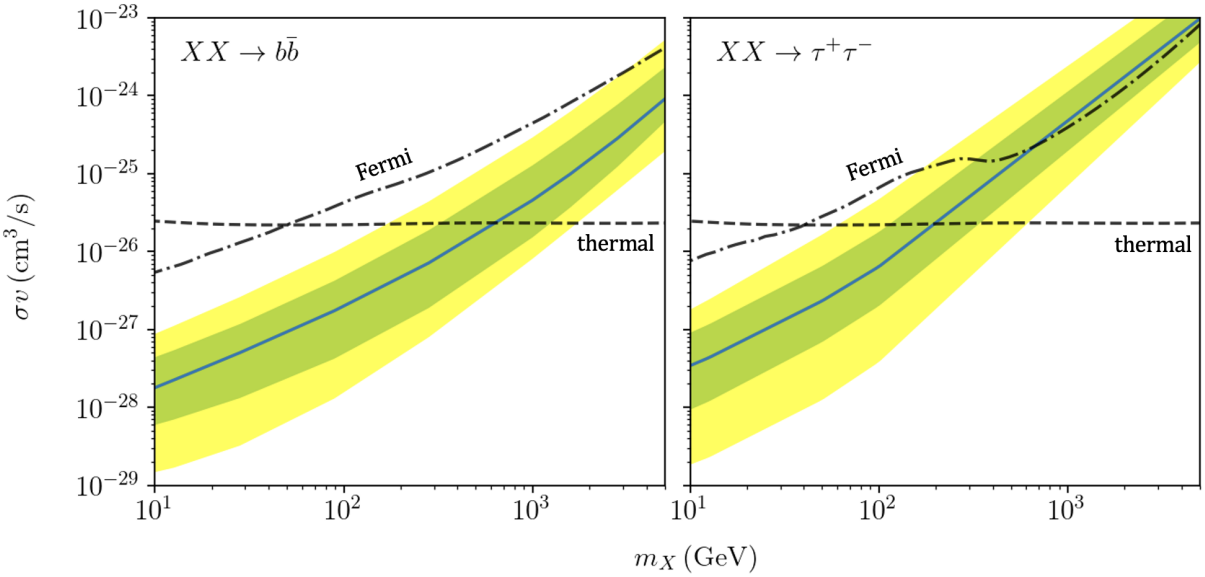

Figure 2.2: The projected constraints on the DM annihilation cross section (to $b\bar{b}$ or $\tau^+\tau^-$) for 10 years of APT data from the directions of 30 Milky Way dwarf galaxies (see Table 2.1). The solid lines and the surrounding green and yellow bands denote the median constraint and the range of constraints attained in 68% and 95% of the simulated realizations, respectively. The dashed curve is the annihilation cross section predicted for a DM candidate that is a (velocity-independent) thermal relic [Steigman et al., 2012], while the dot-dashed line is the current constraint from Fermi data, as presented in Ref. [Di Mauro et al., 2022].

likelihood of attaining the simulated data as a function of $\langle\sigma v\rangle$ (for a given value of the DM mass and annihilation channel). Furthermore, for each simulated dwarf, we draw the value of $\log_{10}(J)$ from a Gaussian distribution with a central value and width equal to the quoted best-fit value and uncertainty [Pace and Strigari, 2019]. In evaluating the stacked likelihood, we follow the approach described in Ref. [Ackermann et al., 2014]. We repeat this procedure 1000 times for each DM mass, cross-section, and channel in order to attain the resulting statistical distribution.

To assess the adequacy of our simulation and background model, we simulated four years of Fermi data from the directions of 15 dwarf galaxies and compared the resulting constraints to those attained by the Fermi Collaboration from four years of real data [Ackermann et al., 2014]. In performing this comparison, we adopted the same J-factors (and their uncertainties) as in Ref. [Ackermann et al., 2014], and used the energy-dependent acceptance as given

in Ref. [Ajello et al., 2021]. For each realization, we calculated the 95% confidence-level upper limit on the annihilation cross-section, corresponding to a change in the log-likelihood (relative to $\langle \sigma v \rangle = 0$) of $2\Delta \ln \mathcal{L} = -3.84$. As can be seen in Fig. 2.1, our simulated constraints are very similar to those found using real Fermi data, demonstrating that our model provides a good description of the backgrounds relevant to such an analysis.

2.3 The Projected Sensitivity of APT to Annihilating Dark Matter

To assess the projected sensitivity of the APT [Alnussirat et al., 2021, Buckley et al., 2021], as mentioned in Section 1.2.1, to DM particles annihilating in Milky Way dwarf galaxies, we simulated 10 years of APT data, adopting an acceptance as given in Ref. [Alnussirat et al., 2021], considering the 30 dwarf galaxies listed in Table 2.1 (exempting Fornax), and using the J-factor determinations from Ref. [Pace and Strigari, 2019].

We show the results of this exercise in Fig. 2.2, for the cases of annihilation to $b\bar{b}$ or $\tau^+\tau^-$. Due to the much larger acceptance of APT, these projected constraints are significantly more stringent than those derived from Fermi data [Albert et al., 2017, Di Mauro et al., 2022]. For comparison, we also include in these frames the annihilation cross section for a DM candidate that is a (velocity-independent) thermal relic [Steigman et al., 2012], as well as the latest constraints derived from Fermi data [Di Mauro et al., 2022]. The constraints projected for other annihilation channels are shown in Fig. 2.3.

2.4 Testing the Origin of the Galactic Center Gamma-Ray Excess

In the previous section, we carried out our simulations under the assumption that there is no signal from annihilating DM, and derived the constraints that could be attained by an instrument such as APT. It is possible, however, that such a signal could be found in the

data, in particular in light of the long-standing Galactic Center Gamma-Ray Excess [Cholis et al., 2021, Di Mauro, 2021, Goodenough and Hooper, 2009, Hooper and Goodenough, 2011, Hooper and Linden, 2011, Abazajian and Kaplinghat, 2012, Hooper and Slatyer, 2013, Gordon and Macias, 2013, Daylan et al., 2016, Calore et al., 2015, Ajello et al., 2016]. Motivated by this excess, we consider in this section a scenario in which the Galactic Center excess is generated by annihilating DM, evaluating the sensitivity of APT to a DM candidate that is capable of generating this signal.

For concreteness, we will consider a DM particle with a mass of $m_X = 45\,\mathrm{GeV}$ and that annihilates to $b\bar{b}$ with a cross-section of $\langle\sigma v\rangle = 2 \times 10^{-26}\,\mathrm{cm}^3/\mathrm{s}$. We again perform a simulation of 10 years of data from the directions of 30 dwarf galaxies, but calculate the change in the log-likelihood relative to the best fit value of m_X and $\langle\sigma v\rangle$. The results of this exercise are shown in Fig. 2.4. Relative to the best-fit parameter values, $\langle\sigma v\rangle = 0$ is disfavored in this scenario at a level of $2\Delta \ln \mathcal{L} \approx -200$, ruling out the null hypothesis with a significance of approximately 14σ.

The gamma-ray signal from DM annihilating in a given dwarf galaxy is proportional to that galaxy's J-factor, providing us with a powerful way to distinguish DM annihilation products from astrophysical backgrounds (which would not be expected to scale with J). In a scenario with $m_X = 45\,\mathrm{GeV}$ and $\langle\sigma v\rangle = 2 \times 10^{-26}\,\mathrm{cm}^3/\mathrm{s}$ (to $b\bar{b}$), we find (in our median simulation) that will detect 7 dwarf galaxies at $> 2\sigma$ significance, 4 at $> 3\sigma$, and 3 at $> 5\sigma$. This data would allow us to test the whether the the gamma-ray fluxes from these galaxies are, in fact, proportional to the corresponding J-factors. In Fig. 2.5, we show the results of a representative realization of our simulation, showing the gamma-ray fluxes from each of the 7 dwarfs that were detected with greater than 2σ significance.

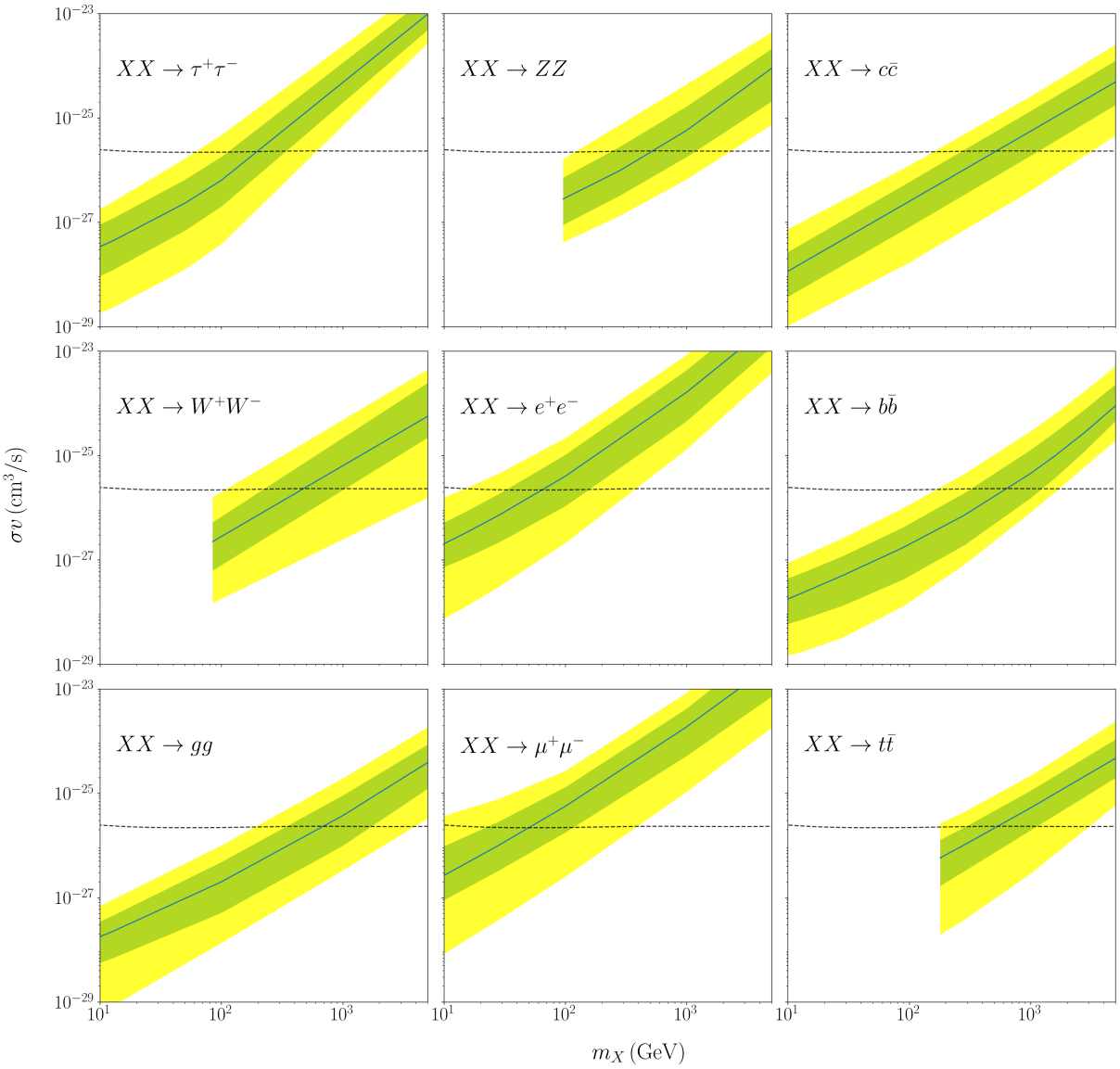

Figure 2.3: As in Fig. 2.2 but for other annihilation channels. These projected constraints are based on 10 years of simulated APT data from the directions of 30 Milky Way dwarf galaxies (see Table 2.1). The solid lines and the surrounding green and yellow bands denote the median constraint and the range of constraints attained in 68% and 95% of the simulated realizations, respectively. The dashed curve is the annihilation cross section predicted for a DM candidate that is a (velocity-independent) thermal relic [Steigman et al., 2012].

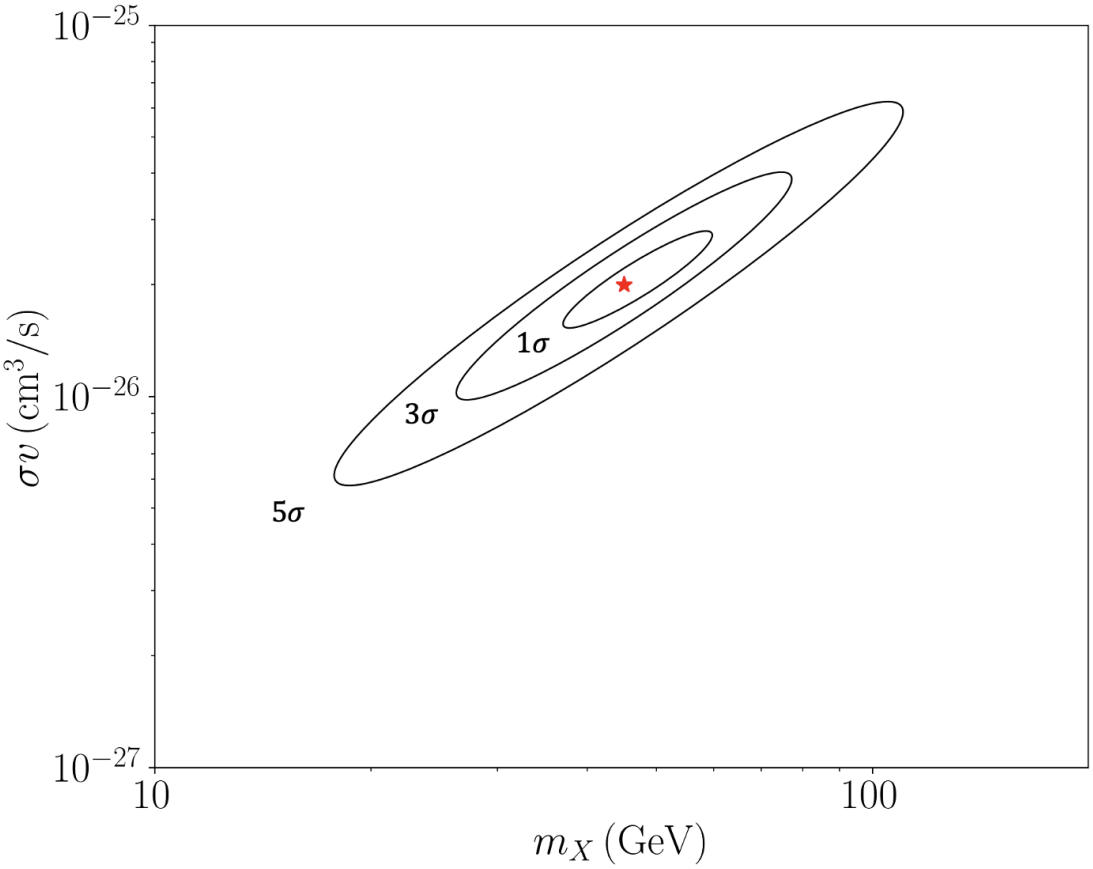

Figure 2.4: The projected ability of APT (with 10 years of data) to measure the DM mass and annihilation cross section in a scenario with $m_X = 45\,\mathrm{GeV}$ and $\langle\sigma v\rangle = 2 \times 10^{-26}\,\mathrm{cm}^3/\mathrm{s}$ (to $b\bar{b}$), as motivated by the Galactic Center Gamma-Ray Excess. The star and surrounding contours represent the best-fit value and the 1, 3 and 5σ confidence intervals, respectively. In such a scenario, we project that APT could exclude the null hypothesis at a level of $2\Delta \ln \mathcal{L} \approx -200$, corresponding to a significance of 14σ.

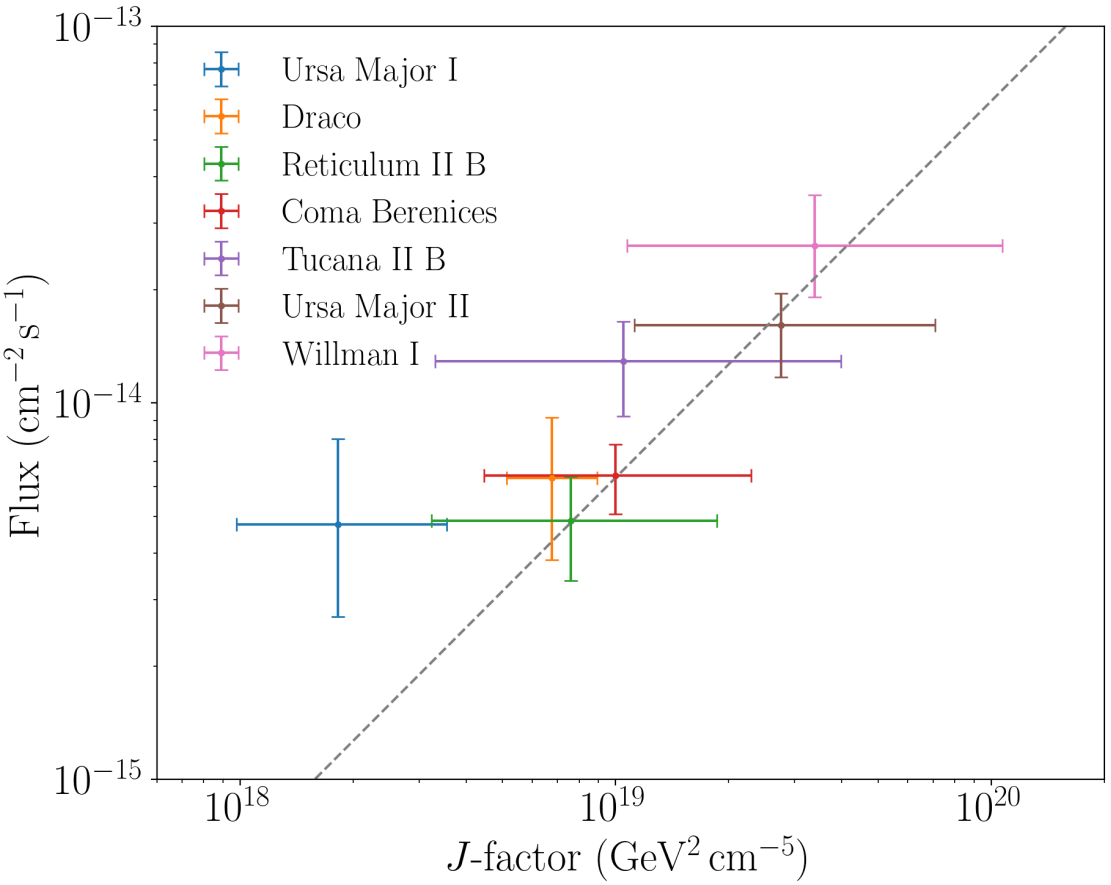

Figure 2.5: The projected ability of APT (with 10 years of data) to measure the gamma-ray fluxes (integrated above 0.1 GeV) from individual dwarf galaxies in a scenario with $m_X = 45\,\mathrm{GeV}$ and $\langle\sigma v\rangle = 2 \times 10^{-26}\,\mathrm{cm}^3/\mathrm{s}$ (to $b\bar{b}$), as motivated by the Galactic Center Gamma-Ray Excess. These fluxes are compared to the J-factors of the dwarfs, as integrated within a radius of 0.5°. These results were attained in a single (but representative) realization of our simulation, showing each dwarf that was detected with a significance of 2σ or higher. Such a data set would allow us to test whether the gamma-ray fluxes from dwarf galaxies are proportional to the corresponding J-factors, providing an unambiguous test of DM interpretations of the Galactic Center Gamma-Ray Excess.

CHAPTER 3

CONTRIBUTION OF TEV HALOS TO THE GAMMA-RAY BACKGROUND

3.1 Introduction

Observations with the HAWC Hooper et al. [2017], Linden et al. [2017], Abeysekara et al. [2017, 2020], Albert et al. [2020b], Milagro [Abdo et al., 2009, Linden and Buckman, 2018], and HESS [Abdalla et al., 2018b,a] telescopes have revealed that pulsars are surrounded by spatially extended "TeV halos" [Albert et al., 2021]. The multi-TeV gamma-ray emission that is associated with these halos is the result of ICS, and is powered by the rotational kinetic energy of the host pulsar [Sudoh et al., 2021]. These objects represent a new class of high-energy sources, which are responsible for a significant fraction of the Milky Way's TeV-scale gamma-ray emission.

From the measured abundance of pulsars and the efficiency with which they are observed to generate TeV halos, it can be shown that these objects dominate the diffuse TeV-scale emission that is observed along the plane of the Milky Way [Linden and Buckman, 2018]. On similar grounds, one can deduce that this class of sources must contribute significantly to the total IGRB, in particular at TeV-scale energies. In this sense, TeV halos appear to be an important means by which star formation leads to the production of very high-energy radiation.

In this chapter, we use the observed characteristics of the TeV halos detected by HAWC to estimate the TeV-scale gamma-ray emission from the TeV halo population in the Andromeda Galaxy (M31), as well as to calculate the contribution from this source class to the total IGRB. While we conclude that the gamma-ray emission from the TeV halos in M31 should be below current constraints, we predict that this signal will be detectable in the future by the CTA. Furthermore, we predict that the TeV halos distributed throughout the observable

universe contribute significantly to the IGRB, being responsible for up to ∼20% of this background at 100 GeV, and perhaps even a larger fraction at TeV-scale energies. Furthermore, if the total spin-down power of the millisecond pulsar population is comparable to or larger than that associated with young and middle-aged pulsars, this would significantly increase our estimates for these gamma-ray fluxes.

3.2 Gamma-Ray Emission From TeV Halos

Pulsars generate the gamma-ray emission associated with TeV halos by transferring their rotational kinetic energy into the acceleration of very high-energy electrons and positrons. These particles then diffuse outward and undergo ICS. The integrated energy budget for the resulting emission is, therefore, limited by the pulsar's initial rotational kinetic energy, which is given in Equation (1.21) in Section 1.2.3.

By extension, the time-averaged, total energy budget for a population of TeV halos is given by the product of the pulsar birth rate and the average initial rotational kinetic energy of an individual pulsar. With this in mind, we will consider the value of $E_{\rm rot}$ averaged over an ensemble of newly formed pulsars:

$$\langle E_{\rm rot,0} \rangle \approx \frac{4\pi^2 M R^2}{5} \left\langle \frac{1}{P_0^2} \right\rangle \tag{3.1}$$

The pulsar-to-pulsar variations in M and R are each small compared to those associated with a pulsar's initial period. Throughout this study, we adopt $M = 1.28 M_{\odot}$ The initial period of a pulsar, P_0, can be difficult to determine directly from observations [Kaspi et al., 2001, Popov and Turolla, 2012, Igoshev and Popov, 2013]. To estimate the value of $\langle P_0^{-2} \rangle$, we have performed an average of this quantity over the youngest pulsars contained within the Australia Telescope National Facility (ATNF) pulsar catalog [Manchester et al., 2005].

The evolution of a pulsar's period is described by

$$P(t) = P_0\left(1 + \frac{t}{\tau}\right)^{1/(n-1)}, \tag{3.2}$$

where n is the braking index ($n = 3$ in the case that the pulsar's spin-down torque arises entirely from dipole radiation [Ostriker and Gunn, 1969, Johnston and Galloway, 1999]) and τ is the spindown timescale:

$$\begin{aligned}\tau &= \frac{3c^2 I P_0^2}{4\pi^2 B^2 R^6} \\ &\approx 3.5 \times 10^4\,\mathrm{yr} \times \left(\frac{2 \times 10^{12}\,\mathrm{G}}{B}\right)^2 \left(\frac{P_0}{0.065\,\mathrm{s}}\right)^2.\end{aligned} \tag{3.3}$$

With this timescale for spindown in mind, we performed an average of P^{-2} over the 32 (non-binary) pulsars in the ATNF catalog with a characteristic age of 10^4 years or less, defined as $t_c \equiv P/2\dot{P} = (n-1)(t_{\mathrm{age}} + \tau)/2 < 10^4\,\mathrm{yr}$, finding $\langle P^{-2}\rangle = (65\,\mathrm{ms})^{-2}$. From this, we estimate that the initial rotational kinetic energy of an average pulsar is $E_{\mathrm{rot},0} \approx 7 \times 10^{48}\,\mathrm{erg}$. Note that among this sample, there is no discernible correlation between the pulsars' period and distance, suggesting that no sizable bias is likely to have resulted from selection effects. If we expand our sample to consider the 151 pulsars with $t_c < 10^5\,\mathrm{yr}$, we obtain a somewhat lower average rate of rotation, $\langle P^{-2}\rangle = (95\,\mathrm{ms})^{-2}$, indicative of a non-negligible reduction in the average pulsar's rotational kinetic energy.

Only a fraction of a given pulsar's total rotational kinetic goes into the gamma-ray emission associated with a TeV halo. We define the efficiency of a TeV halo, η, which is given in Equation (1.22) in Section 1.2.3, where F_γ is the flux of the gamma-ray emission bewteen 0.1-100 TeV, $\dot{E}_{\mathrm{rot}}$ is the time derivative of the pulsar's rotational kinetic energy, and d is the distance to the pulsar. Once again, we are interested here in the value of η averaged across a large sample of pulsars. We determine this quantity by comparing the current spindown flux of a given pulsar, $\dot{E}_{\mathrm{rot}}/4\pi d^2$, as reported in the ATNF catalog, to the

gamma-ray flux reported by the HAWC Collaboration, as obtained using the tool available at `https://data.hawc-observatory.org/datasets/3hwc-survey/index.php`. In making this comparison, we have restricted our sample to those pulsars that are located within HAWC's field-of-view ($-10^\circ < \text{dec} < 50^\circ$), and for which $t_c > 10^4$ years. This latter requirement is intended to avoid contaminating our sample with sources that might be better classified as pulsar wind nebulae or supernova remnants. We also restrict our analysis to those pulsars with a spindown flux greater than $\dot{E}/4\pi d^2 > 10^{-10}\,\text{TeV}\,\text{cm}^{-2}\,\text{s}^{-1}$, in an effort to minimize any bias that might result from selection effects. We have identified 26 pulsars in the ATNF catalog which satisfy these criteria.

The HAWC online tool allows one to obtain a measurement of the gamma-ray flux from a given source, as evaluated at an energy of 7 TeV, assuming a power-law spectrum with an index of -2.5. For each pulsar, we integrate over this spectral shape between 0.1 and 100 TeV to obtain an estimate for F_γ. Following Refs. [Hooper and Linden, 2021, 2018], we adopt the point-like template for pulsars located at $d > 2$ kpc, the template with 0.5° extension for pulsars between 0.75 kpc $< d <$ 2 kpc, the 1° extension template for those within 0.375 kpc $< d <$ 0.75 kpc, and the 2° extension template for pulsars closer than $d <$0.375 kpc. Averaging over this sample, we obtain an average gamma-ray efficiency of $\langle\eta\rangle = 0.054$.

We note that the HAWC online tool is not very flexible in the respect that it only constrains the flux from a given source assuming that its spectrum is described by a power-law with an index of -2.5, and thus is not optimally suited for the application at hand. In particular, while the detailed spectral shape of the gamma-ray emission from a TeV halo has been measured only in a few cases, these sources appear to exhibit spectra that are significantly harder than that of a -2.5 index power law. More specifically, the gamma-ray emission from TeV halos is observed to be quite hard up to energies on the order of $\mathcal{O}(10\,\text{TeV})$, above which the spectrum becomes much softer. On theoretical grounds, one expects such a spectral break to appear, positioned near the energy at which the timescale

for electron/positron energy losses are comparable to the age of the pulsar [Sudoh et al., 2021]. In light of these considerations, it is plausible that the harder spectra indices of TeV halos may have led us to somewhat overestimate the value of $\langle \eta \rangle$ in the approach taken in the previous paragraph.

In the 3HWC catalog presented by the HAWC Collaboration, the flux and spectral index of each source is provided, as evaluated at an energy of 7 TeV [Albert et al., 2020b]. More information, however, is provided for some of these sources in HAWC's catalog of TeV halos detected at energies above 56 TeV [Abeysekara et al., 2020]. Averaging the value of η over this collection of 9 sources (see Table 1 of Ref. [Sudoh et al., 2021]), we obtain $\langle \eta \rangle \approx 0.063$, which is only slightly higher than the value found using the approach described in the previous paragraph. In light of these considerations, we will adopt a range of $\langle \eta \rangle = 0.04 - 0.06$ throughout the remainder of this study.

To assess the spectral shape of the gamma-ray emission from a typical TeV halo, we consider three sources which have had their spectra measured in some detail [Abeysekara et al., 2020]. In particular, we will base our results on the spectral shapes of the emission observed from eHWC J1825-134 (PSR J1826-1256), eHWC J1907+063 (PSR J1907+0602), and eHWC J2019+368 (PSR J2021+3651), as reported in Ref. [Abeysekara et al., 2020] (see also, Ref. [Sudoh et al., 2021]). These sources each exhibit a spectrum that can be reasonably well described by a smoothly broken power-law, which we parameterize as follows:

$$\frac{dN_\gamma}{dE_\gamma} \propto \left(\frac{E_\gamma}{E_b}\right)^{-\alpha} \left[1 + \left(\frac{E_\gamma}{E_b}\right)\right]^{\alpha-\beta}. \tag{3.4}$$

For the three above mentioned TeV halos, the spectrum of ICS given in Fig. 3 of Ref. [Sudoh et al., 2021] is best fit by $(\alpha,\ \beta,\ E_b) = (1.65, 3.36, 5.9\,\text{TeV})$, $(1.58, 3.08, 6.2\,\text{TeV})$, and $(1.66, 3.12, 23.6\,\text{TeV})$, respectively. Based on these selected sources, we adopt $\alpha = 1.63$, $\beta = 3.18$, and $E_b = 10\,\text{TeV}$ as our estimate for the spectral shape of a typical TeV halo.

3.3 Gamma-Ray Emission from Andromeda's TeV Halo Population

Before moving forward to calculate the total gamma-ray emission from the TeV halos found throughout the volume of the observable universe, we will consider in this section the prospects for detecting such a signal from the TeV halos located within the Andromeda Galaxy. The Andromeda galaxy, or M31, is a spiral galaxy located at a distance of $d_{\rm M31}$ =765±28 kpc from the Milky Way [Riess et al., 2012]. By comparing its current rate of star formation to that of the Milky Way's, we will estimate the total gamma-ray emission from M31's TeV halo population and compare this to the sensitivity of existing and future gamma-ray telescopes.

To estimate the current pulsar birth rate in M31, $\Gamma_{p,\rm M31}$, we assume that this quantity scales with the overall star-formation rate, $\Gamma_{\star}$, and thereby relate the pulsar birth rate in M31 to that in the Milky Way as follows:

$$\Gamma_{p,\rm M31} = \frac{\Gamma_{\star,\rm M31}}{\Gamma_{\star,\rm MW}} \times \Gamma_{p,\rm MW}. \tag{3.5}$$

While this relationship is only expected to apply to galaxies which produce stars with a similar initial mass function, it should be safely applicable in the particular case of Andromeda and the Milky Way.

Many methods are used to determine or constrain the star-formation rate of a given galaxy, including those based on observations of Lyman continuum photons, infrared emission, Hα lines, ultra-violet emission, supernovae rates, and counts of resolved stellar populations (for reviews, see Refs. [Kennicutt and Evans, 2012, Madau and Dickinson, 2014]). Many of these techniques are sensitive to the rate of massive star formation, which can be extrapolated to determine the total star-formation rate for a given choice of the inital mass function. Some of these techniques can be applied to the case of the Milky Way,

while others are more suitable to other galaxies [Chomiuk and Povich, 2011]. For example, Hα emission is often used to estimate the star-formation rates of galaxies, but is not useful in the plane of the Milky Way due to the effects of dust extinction [Chomiuk and Povich, 2011]. In this chapter, we adopt for the Milky Way a star-formation rate given by $\Gamma_{\star,\rm MW} = 1.65 \pm 0.19\, M_{\odot}{\rm yr}^{-1}$, based on a combination of measurements including the Lyman continuum photon flux, supernovae rates, massive star counts, and infrared emission [Licquia and Newman, 2015]. For the case of M31, we follow Ref. [Rahmani et al., 2016], which describes three methods for measuring the star-formation rate of Andromeda. Using a combination of far-UV and 24 μm emission, Hα emission and 24 μm emission, and the total infrared emission, that study obtained $\Gamma_{\star,\rm M31} = 0.31 \pm 0.04\, M_{\odot}{\rm yr}^{-1}$, $0.35 \pm 0.01\, M_{\odot}{\rm yr}^{-1}$, and $0.40 \pm 0.04\, M_{\odot}{\rm yr}^{-1}$, respectively. With these results in hand, we adopt a range for $\Gamma_{\star,\rm M31}/\Gamma_{\star,\rm MW}$ that is given by 0.21 ± 0.04. After combining this in quadrature with a value of 1.4 ± 0.2 pulsars per century for the Milky Way's pulsar birth rate [Lorimer et al., 2006], this yields a birth rate of 0.29 ± 0.07 pulsars per century in M31. Alternatively, the observed rates for core-collapse supernovae (CCSN) can be used to estimate the ratio of pulsar birth rates in the Milky Way and Andromeda. Based on Ref. [Rozwadowska et al., 2021], this yields ${\rm CCSN_{M31}/CCSN_{MW}} \sim 0.25 - 0.75$, corresponding to a pulsar birth rate of $\sim 0.3 - 1.2$ per century for M31, consistent with our previous determination.

Using this calculation for the pulsar rate in M31, we can now estimate the total TeV halo emission from this galaxy. We will proceed under the reasonable assumption that the TeV halos in M31 generate gamma-ray emission that is similar in overall intensity and spectral shape to those found in the Milky Way. The total TeV-scale luminosity of the TeV halos in M31 can thus be expressed as $L_{\rm M31} = \Gamma_{p,\rm M31} \langle \eta \rangle \langle E_{\rm rot,0} \rangle / 4\pi d^2$.

In Fig. 3.1, we plot our estimate for the gamma-ray emission from the TeV halo population of M31. The width of this band reflects the uncertainties in the gamma-ray efficiency and pulsar birth rate. We compare this result to the upper limits reported by the HAWC [Albert

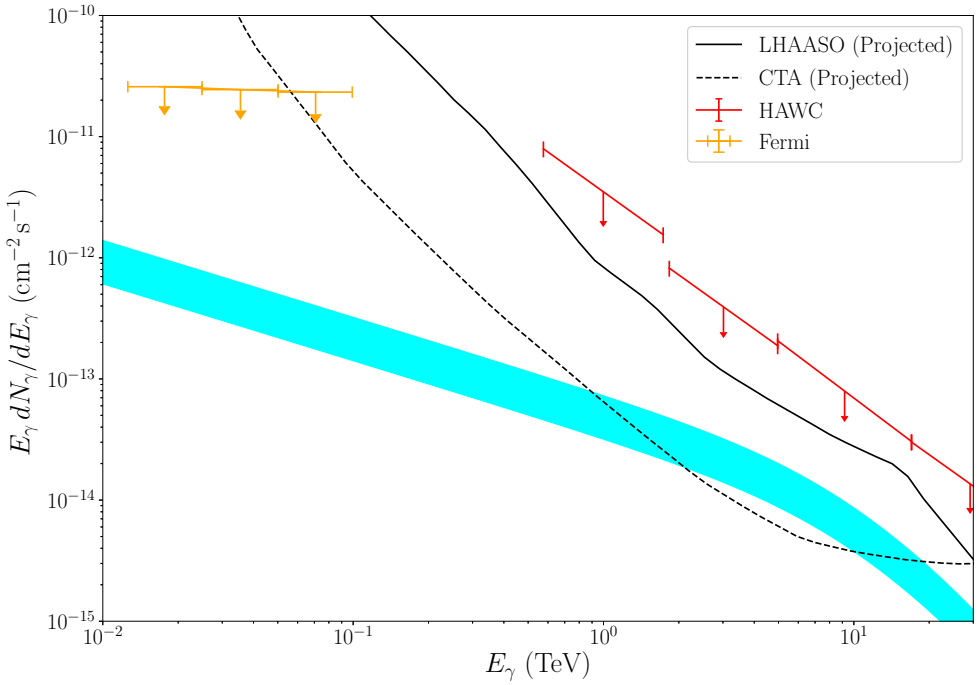

Figure 3.1: The gamma-ray emission from the population of TeV halos in the Andromeda Galaxy (M31) is shown as a cyan band. The width of this band reflects the uncertainties in the gamma-ray efficiency and pulsar birth rate, for which we have adopted the following ranges: $\langle \eta \rangle = 0.04 - 0.06$ and $\Gamma_{p,\mathrm{M31}} = 0.23 - 0.35$ per century. These results are compared to the upper limits reported by the HAWC [Albert et al., 2020a] and Fermi [Ackermann et al., 2017] Collaborations, as well as the projected sensitivity of LHAASO [Bai et al., 2019] and CTA [Acharya et al., 2013] (for 1 year and 50 hours of observation, respectively). While our range of estimates for this emission are consistent with current constraints, the prospects for detecting this emission with future telescopes appear promising.

et al., 2020a] and Fermi [Ackermann et al., 2017] (see also, Refs. [Karwin et al., 2021a,b]) Collaborations, as well as the projected sensitivity of LHAASO [Bai et al., 2019] and CTA [Acharya et al., 2013]. These projected sensitivities were each calculated by simulating the detector response to a Crab Nebula-like point source, and adopting an observation time of 1 year (LHAASO) or 50 hours (CTA). While our projections for this emission are consistent with current constraints, the prospects for detecting this emission with future telescopes seem promising. Note that we expect TeV halos to provide the dominant contribution to the $\gtrsim$ TeV gamma-ray emission from galaxies such as the Milky Way and M31 [Linden and Buckman, 2018].

In addition to characterizing the gamma-ray emission originating from TeV halos, future gamma-ray observations of M31 will also provide valuable information pertaining to cosmic ray transport in that system, and will constrain more exotic signals, such as emission from Andromeda supermassive black hole, emission analogous to the Milky Way's "Fermi Bubbles", and the products of DM annihilation or decay [Aharonian et al., 2003, McDaniel et al., 2019, Ackermann et al., 2017, Albert et al., 2020a].

3.4 TeV Halos and the Isotropic Gamma-Ray Background

In the previous section, we calculated the emission from TeV halos in the nearby galaxy M31. In this section, we will proceed to calculate the total emission from TeV halos throughout the observable universe, determining their contribution to the IGRB as measured by the Fermi telescope [Ackermann et al., 2015a].

Neglecting the effects of attenuation for the moment, the spectrum of gamma rays per area per time per solid angle from the integrated population of extragalactic TeV halos is

given by:

$$\frac{dN_\gamma}{dE_\gamma}(E_\gamma) = \frac{c}{4\pi}\int \frac{dz}{H(z)(1+z)^3} \times \frac{d\Gamma_p}{dV}(z)\langle E_{\rm rot,0}\rangle \, \langle \eta \rangle \left(A\frac{dN_\gamma}{dE'}\right)_{E'=E_\gamma(1+z)}, \tag{3.6}$$

where $H(z) = H_0\left[\Omega_M(1+z)^3 + \Omega_\Lambda\right]^{0.5}$ is the rate of Hubble expansion, $d\Gamma_p/dV(z)$ is the average pulsar birth rate per volume as a function of redshift, the quantity $\langle E_{\rm rot,0}\rangle \times \langle \eta \rangle$ is the average total energy emitted from a pulsar in TeV-scale gamma-rays, and dN_γ/dE' is the average spectrum of the gamma-ray emission from an individual pulsar, after accounting for the effects of cosmological redshift. The normalization constant, A, has units of inverse energy, and is set such that

$$\int_{0.1\,{\rm TeV}}^{100\,{\rm TeV}} A\frac{dN_\gamma}{dE'}E'dE' = 1. \tag{3.7}$$

Throughout this study, we will adopt $\Omega_M = 0.31$, $\Omega_\Lambda = 0.69$, and $H_0 = 67.7\,{\rm km/s/Mpc}$, as reported by the Planck Collaboration [Aghanim et al., 2020].

As we did in the case of M31, we will base our estimate for the emission from the sum of all cosmologically distributed TeV halos on that observed from these objects in the Milky Way, scaling the relative intensities with the pulsar birth rate. To estimate the pulsar birth rate as a function of redshift, we adopt three different approaches. First, we estimate the pulsar birth rate as a function of redshift by scaling this function to the measured rate of star formation. More specifically, we adopt the cosmic star-formation rate (per comoving volume) as reported in Ref. [Hopkins and Beacom, 2006] (and using the parametric form of Ref. [Cole et al., 2001]):

$$\dot{\rho_*}(z) = \frac{(0.017+0.13z)h}{1+(z/3.3)^{5.3}}\,{\rm M_\odot\,Mpc^{-3}\,yr^{-1}}, \tag{3.8}$$

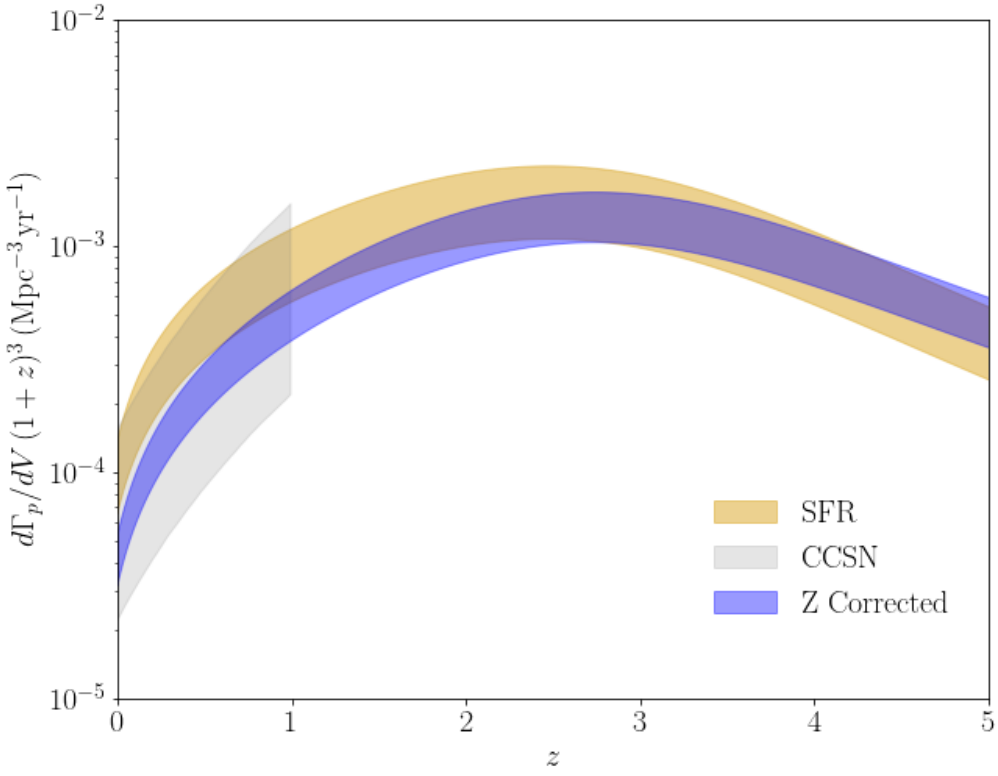

Figure 3.2: The comoving pulsar birth rate density as a function of redshift, calculated based on the star-formation rate density (yellow), the core collapse supernova rate density (grey), and using the metallicity corrected method described in the text (blue). The bands reflect the 1σ uncertainties in the measurements of the star-formation rate density and the core collapse supernova rate.

where $h = 0.677$. The 1σ uncertainty associated with this quantity is approximately $\pm 25\%$ [Horiuchi et al., 2011]. Assuming that the pulsar birth rate is proportional to the star-formation rate, we can relate $d\Gamma_p/dV(z)$ to this function, and to the local pulsar birth rate to star-forming rate ratio:

$$\frac{d\Gamma_p}{dV}(z) = \frac{\rho_*(z)}{(1+z)^3} \frac{\Gamma_{p,\rm MW}}{\Gamma_{\star,\rm MW}}. \tag{3.9}$$

Alternatively, we could instead scale the pulsar birth rate to the rate of core collapse supernovae as measured, for example, by the Lick Observatory Supernova Search (LOSS) Leaman et al. [2011], Li et al. [2011b,a], Maoz et al. [2011], and then normalize this to the rate of core collapse supernovae in the Milky Way, $R_{\rm CCSN,MW} = 1.9 \pm 1.1$ per century Diehl et al. [2006]. This approach has the advantage of being less sensitive to variations in the initial mass function, but suffers from larger overall uncertainties and is limited to modest redshifts, $z \lesssim 1$.

As a third method, we have estimated the pulsar birth rate over cosmic history from the evolution of the initial mass function as a function of mass and metallicity. From the initial mass function, we can calculate the number of neutron stars that are formed per unit mass of star formation:

$$f_{\rm NS} = \frac{\int_{M_{\rm min}}^{M_{\rm max}} \phi \, dM}{\int_{0.1 M_\odot}^{100 M_\odot} \phi \, M dM}, \tag{3.10}$$

where $M_{\rm min}$ and $M_{\rm max}$ represent the mass range of stellar progenitors that ultimately lead to the formation of a neutron star. The function ϕ is the initial mass function, for which we adopt the following [Marks et al., 2012]:

$$\phi(M,Z) \propto \begin{cases} M^{-1.3} & 0.1 M_\odot < M < 0.5 M_\odot \\ M^{0.66 \log_{10}(Z/Z_\odot)+2.63} & 0.5 M_\odot < M < 100 M_\odot \end{cases}$$

where $Z/Z_{\odot}$ is the metallicity in solar units. Notice that the slope at low masses follows the canonical behavior of the Kroupa [2001] initial mass function.

Depending on the mass of the final remnant, a core collapse supernova can produce a neutron star or a black hole. We set the threshold for this distinction to $2.5 M_{\odot}$, which we then relate to the maximum initial stellar mass, $M_{\rm max}$, as a function of metallicity according to Eqns. (5)-(9) in Ref. Fryer et al. [2012]. We then determine as follows the minimum initial stellar mass, $M_{\rm min}$, that can result the formation of a neutron star Fryer et al. [2012]:

$$M_{\rm min} = \begin{cases} [9.0 + 0.9 \, \log_{10}(Z/Z_{\odot})] \, M_{\odot} & \log_{10}(Z/Z_{\odot}) > -3 \\ 6.3 \, M_{\odot} & \log_{10}(Z/Z_{\odot}) \leq -3 \end{cases}$$

Since the quantities ϕ, $M_{\rm max}$ and $M_{\rm min}$ each depend on metallicity, we need to quantify the distribution of Z as a function of redshift. To this end, we follow Ref. Langer and Norman [2006], which provides a function for the fraction of the star-formation rate density that has a metallicity less than Z at given redshift, z:

$$\Lambda(z, Z) = \frac{\hat{\Gamma}[0.84, (Z/Z_{\odot})^2 10^{0.3z}]}{\Gamma(0.84)}, \tag{3.11}$$

where $\hat{\Gamma}$ and Γ are the incomplete and complete gamma functions, respectively.

Putting this all together, the final cosmic pulsar birth rate density is given by

$$\frac{d\Gamma_p}{dV}(z) = \dot{\rho}_*(z) \int \frac{d\Lambda}{dZ}(z, Z) \, f_{\rm NS}(Z) \, dZ. \tag{3.12}$$

In Fig. 3.2, we plot the pulsar birth rate density as a function of redshift, using each of the three methods described in this section. The results are broadly consistent across these three methods, although the distribution based on the star-formation rate alone is somewhat larger at low redshifts than is found when using the metallicity corrected approach. The rate based on the rate of core collapse supernovae is consistent with both other methods, although

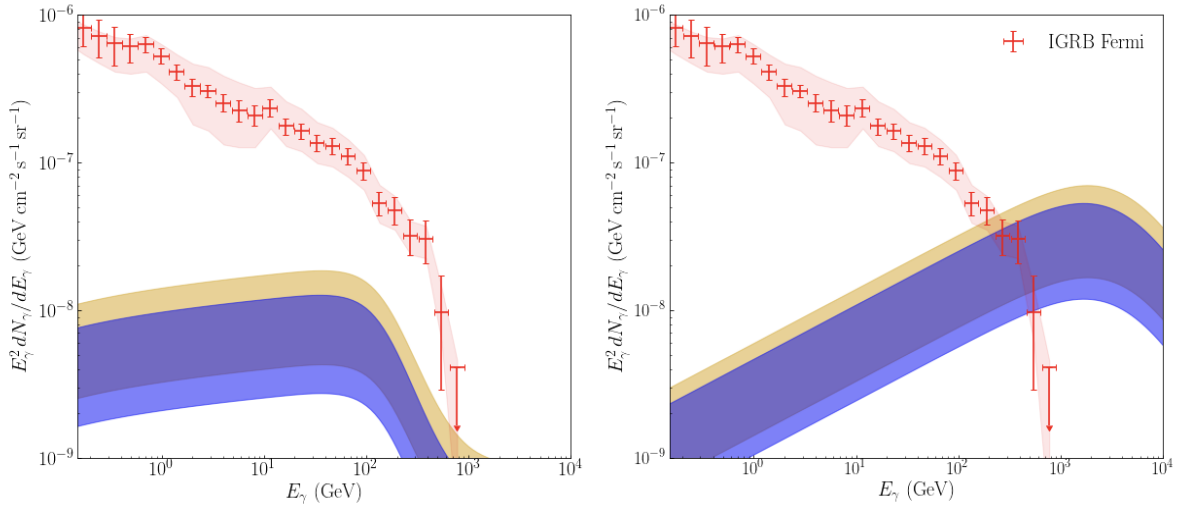

Figure 3.3: The predicted contribution from TeV halos to the isotropic gamma-ray background, compared to the spectrum as measured and reported by the Fermi Collaboration [Ackermann et al., 2015a]. These results were derived using pulsar birth rates based on the measured star-formation rate, with (blue) and without (yellow) corrections for metallicity. The grey bands around the Fermi error bars represent the systematic uncertainty associated with the modelling of the Galactic foreground emission. In the left (right) frame, we show our results including (neglecting) the important effects of attenuation and EM cascades.

with large uncertainties. In our main results, we will show the gamma-ray spectra predicted using cosmic pulsar birth rates as calculated using both the star-forming rate scaling, and the metallicity-corrected approach.

In calculating the contribution from TeV halos to the isotropic gamma-ray background, it is necessary to take into account the effects of attenuation and the EM cascades that result from these interactions. In particular, TeV-scale photons can efficiently scatter with the infrared background to produce electron-positron pairs which then generate lower energy photons as they cool through the process of ICS. To account for this, we use the publicly available code γ-Cascade [Blanco, 2019], which fully models the effects of pair production, ICS, and synchrotron losses (see also, Refs. [Murase, 2012, Murase and Beacom, 2012, Murase et al., 2012, Murase et al., 2012, Berezinsky and Kalashev, 2016, Blanco and Hooper, 2017]). This code adopts a background radiation field based on the model of Ref. [DomÃ-nguez et al., 2010], and adopts an extragalactic magnetic field of 10^{-13} G. In the case of the

emission from TeV halos in M31 (as shown in Fig. 3.1), the effects of attenuation are negligible due to the proximity of this source. In contrast, in our calculation of the contribution to the IGRB from this class of sources, these interactions very substantially suppress the amount of emission that is predicted at energies above $\sim$100 GeV. In addition, the gamma rays that are produced through EM cascades significantly enhance the gamma-ray emission that is expected at lower energies.

In the left frame of Fig. 3.3, we show the main result of this chapter, which is our estimate for the contribution from TeV halos to the IGRB. In the right frame of Fig. 3.3, we show the same thing but, for comparison, neglecting the effects of attenuation and the subsequent contribution from EM cascades. While TeV halos produce very little of the emission that is observed by Fermi at low energies, this class of sources could be responsible for up to $\sim$20% of the IGRB at 100 GeV, and perhaps even an larger fraction at TeV-scale energies.

3.5 Implications for Millisecond Pulsar Populations

Thus far, we have focused in this chapter on the TeV halos associated with young and middle aged pulsars. In addition to these source classes, there exist pulsars with millisecond-scale periods which have obtained their angular momentum through interactions with a binary companion. Such "recycled" pulsars have lower magnetic fields, are much longer lived than their young and middle aged counterparts.

Recent analyses of HAWC data have provisionally indicated that millisecond pulsars (MSPs) generate TeV halos with an efficiency and other characteristics that are similar to those associated with young and middle-aged pulsars [Hooper and Linden, 2021, 2018]. In our calculation of the contribution from TeV halos to the IGRB, we have not yet included any contribution from MSPs. If, however, the total spindown power of the MSP population is comparable to or larger than that associated with the young and middle aged pulsar population, these sources could significantly increase our estimate for the contribution of

TeV halos to the IGRB.

The total spindown power of the Milky Way's MSP population is somewhat uncertain, in particular in regards to those pulsars located in the Inner Galaxy. Among the 283 MSPs in the ATNF catalog with a reported value of $\dot{E}$, the total spindown power is $2.2 \times 10^{37}\,\mathrm{erg/s}$. Given the highly incomplete nature of this catalog, the total spindown power of all MSPs in the Milky Way is likely to be larger than this number by a factor of at least several, and perhaps significantly more. Comparing this to the total spindown power of the young and middle aged pulsars in the Milky Way, $\langle E_{\rm rot,0} \rangle \, \Gamma_{p,\rm MW} \sim (7 \times 10^{48}\,\mathrm{erg/s})\,(1.4\,\mathrm{century}^{-1}) \sim 3 \times 10^{39}\,\mathrm{erg/s}$, we consider it plausible that MSPs could constitute a significant fraction of the total spindown power of the overall pulsar population. If it is robustly confirmed that MSPs generate TeV halos [Hooper and Linden, 2021, 2018], this would lead us to potentially increase our estimate for the contribution of TeV halos to the IGRB (and from the TeV halo emission from M31).

Further complicating this calculation is the fact that the MSP population density is not expected to scale with the current star-formation rate. Instead, the number of MSPs in a given galaxy will reflect the integrated star-formation history and the subsequent rate of stellar encounters within that environment (for example, see Ref. [Bahramian et al., 2013]).

With these uncertainties acknowledged and in mind, we will proceed to estimate the gamma-ray emission from all TeV halos (including those associated with MSPs) by simply scaling our previous results by a factor that is equal to the total spindown power in all pulsars (including MSPs) divided by the total spindown power neglecting MSPs. Using the Milky Way pulsar populations to base this estimate, we note that the median MSP in the ATNF catalog is located only 3.6 kpc from Earth (considering only those MSPs with a reported distance measurement), corresponding to only the nearest 5% of the Galactic Plane, and clearly indicating that most of the MSPs in the Milky Way have not yet been detected. With this in mind, we estimate that including MSPs would increase the fluxes shown in

Figs. 3.1 and 3.3 by a factor of roughly $\sim 1 + [(2.2 \times 10^{37})/0.05]/(3 \times 10^{39}\, f_{\rm beam}) \sim 1.5$, where $f_{\rm beam} \sim 0.3$ is the beaming fraction of a typical MSP.

3.6 Implications for IceCube's Diffuse Neutrino Flux

The results presented in the previous sections have potentially significant implications for the fields of high-energy gamma-ray and neutrino astrophysics. Studies utilizing observed correlations between gamma-ray and multi-wavelength emission have concluded that the IGRB is dominated by emission from a combination of star-forming galaxies and non-blazar active galactic nuclei (sometimes referred to as misaligned AGN). In particular, a recent study by Blanco and Linden concluded that star-forming galaxies produce $56^{+40}_{-23}\%$ of the IGRB at 10 GeV, while non-blazar AGN contribute $18^{+38}_{-12}\%$ of this signal at the same energy [Blanco and Linden, 2021]. In contrast, the contributions to the IGRB from blazars (including both BL Lacs and flat-spectrum radio quasars) [Cuoco et al., 2012, Harding and Abazajian, 2012, Ajello et al., 2012, Abdo et al., 2010], mergering galaxy clusters [Keshet et al., 2003, Gabici and Blasi, 2003, 2004], cosmic-ray interactions with circum-galactic gas [Feldmann et al., 2012], and ultra-high energy cosmic ray propagation [Taylor et al., 2015, Ahlers and Salvado, 2011, Gelmini et al., 2012] are each relatively small in comparison to these two source classes (see also, Refs. [Hooper et al., 2016, Linden, 2017, Tamborra et al., 2014, Di Mauro et al., 2014, Inoue, 2011]).

The diffuse flux of high-energy astrophysical neutrinos reported by the IceCube Collaboration features an approximately power-law form over energies between tens of TeV and several PeV [Aartsen et al., 2015a,b, 2014, 2013], and exhibits flavor ratios that are consistent with the predictions of pion decay [Aartsen et al., 2015c]. The lack of observed correlations in direction or time with known gamma-ray bursts [GRB, 2012] or blazars [Smith et al., 2021, Hooper et al., 2019, Glüsenkamp, 2016] has strongly disfavored the possibility that many of these events originate from members of these source classes. This leaves star-forming galaxies

and non-blazar AGN as the leading candidates for the origin of IceCube's diffuse high-energy neutrino flux. If any combination of these two source classes is responsible for generating the signal reported by IceCube, then these objects must also contribute significantly to the IGRB as measured by Fermi. More specifically, if cosmic-ray interactions in these sources produce pions in optically thin environments, the decaying pions will produce neutrinos, $\pi^+ \rightarrow \mu^+ \nu_\mu \rightarrow e^+ \nu_e \bar{\nu}_e \nu_\mu$, and gamma rays, $\pi^0 \rightarrow \gamma\gamma$, in a calculable ratio. Based on this relationship, quantitative studies have shown that if these source classes are responsible for IceCube's diffuse neutrino flux, they will also approximately saturate the IGRB, in particular at energies above several GeV (see, for example, Ref. [Hooper, 2016]).

The results presented in this study indicate that TeV halos contribute significantly to the IGRB at the highest energies measured by Fermi. On similar grounds, TeV halos have previously been shown to dominate the diffuse TeV-scale emission observed along the Galactic Plane by the Milagro telescope [Linden and Buckman, 2018]. In this sense, it appears that TeV halos are a significant vector by which the process of star formation leads to the production of very high-energy gamma-ray radiation.

A critical point in this context is that TeV halos are leptonic sources, relying on ICS rather than pion production to generate their observed gamma-ray emission [Sudoh et al., 2021, Hooper et al., 2017]. This forces us to conclude that a significant fraction of the highest energy gamma-ray emission observed from star-forming galaxies is not hadronic in origin, but is instead leptonic, suppressing the degree to which this class of sources could potentially contribute to IceCube's diffuse neutrino flux. By comparing the gamma-ray emission from star-forming galaxies [Blanco and Linden, 2021] to that predicted in this study from the TeV halos, one can place an upper limit on the hadronic component of the emission from star-forming galaxies. Although the relevant uncertainties remain quite large at this time, this comparison is suggestive of a significantly leptonic origin of the TeV-scale emission from this class of sources. This conclusion would only be further strengthened if we were

to include an estimated contribution from the TeV halos associated with MSPs. If future observations continue to support the conclusion that MSPs produce TeV halos, this could potentially disfavor star-forming galaxies as the primary source of IceCube's diffuse flux, and (by default) favor non-blazar AGN as the main sources of these mysterious particles.

CHAPTER 4

GRAVITATIONAL-WAVE LENSING AS A NOVEL PROBE

4.1 Introduction

Strong gravitational lensing is a fundamental measurable property of the universe. Lensing observables include the fraction of sources that are multiply imaged, as well as statistical distributions of lensing properties such as the image separations and time delays. These are related to the values of the cosmological parameters, as well as the distribution and properties of the matter inhomogeneities which constitute the lenses, ranging from MAssive Compact Halo Objects (MACHOs) and stars to clusters of galaxies. By observing strong lensing, one is able to probe the evolution of the universe and all matter within it, as well as test the predictions of general relativity.

Observational samples of lensed systems also depend on properties of the sources, and in particular, the number density (for continuous sources such as quasars) or the rate density (for transient sources such as Type Ia supernovae) of the sources as a function of mass and redshift. These samples are also sensitive to observational selection effects, which can cause dramatic differences between the observed and intrinsic lensing distributions.

In the EM band, strong gravitational lensing is not only widely used in probing cosmological parameters [Turner et al., 1984, Cao et al., 2012, Liu et al., 2020b], but also in understanding the nature of DM halos [Davis et al., 2003, Chae, 2003, Chae and Mao, 2003, Sohn et al., 2017, Smail et al., 1994, Schneider, 1996, Keeton and Madau, 2001, Oguri et al., 2002, Hoekstra et al., 2004, Corless and King, 2007, Massey et al., 2010, Collett, 2015, Diego et al., 2018, Meneghetti et al., 2020]. One of the most basic properties that one can probe are the masses of the lensing halos, as traced by their velocity dispersions, σ. For example, Davis et al. [2003] studied 13 lenses provided by the Cosmic Lens All-Sky Survey/Jodrell Very Large Array Astrometric Survey data to constrain the characteristic velocity disper-

sion distribution of elliptical galaxies, σ_*, to $168 \leq \sigma_* \leq 200$ kms^{-1} at 68 % confidence level. Similarly, Chae [2005] selected ∼15 multiply-imaged systems from the same surveys and studied the distribution of the angular separation of these lensing images. By fixing the shape of the galaxy velocity dispersion function either using the Sloan Digital Sky Survey (SDSS) or the Second Southern Sky Redshift Survey (SSRS2), Chae [2005] constrained σ_* to ∼80 km/s for the case of SDSS, and ∼190 km/s for the case of SSRS2. In addition, the time delay between lensed images can be used to investigate the density profile of the lens halos as well as the Hubble parameter, H_0 [Oguri et al., 2002, Li et al., 2012]. Weak lensing surveys, e.g. [To et al., 2021], provide a complementary probe of the matter distribution at larger scales. We note that the distribution of strong lensing of supernovae offers an additional powerful probe [Holz, 2001], but complete and uniformly selected samples of lensed supernovae continue to pose a challenge. This may change with upcoming surveys, such as those from the Vera Rubin Observatory and *Euclid*.

Like EM waves, gravitational waves (GWs) can also be strongly lensed and form multiple images. These images appear as separate GW sources with consistent sky positions and binary parameters such as total mass and mass ratio, but with different magnifications and arrival times. The waveforms of multiply-imaged GW sources may also show different phase shifts depending on whether the image is at the minimum, saddle point or maximum of the Fermat potential [Schneider et al., 1992, Dai et al., 2020]. The magnification changes the overall amplitude of the signal, biasing the inference of the luminosity distance and, as a consequence, the source-frame masses. The time delay affects the arrival time of the lensed signal. Lastly, the phase shift associated to saddle-point images could introduce waveform distortions for signals with higher modes, precession or eccentricity [Dai and Venumadhav, 2017, Ezquiaga et al., 2020], leading to waveforms which appear to violate general relativity [Ezquiaga et al., 2020]. All these properties can be used to identify multiple GW events as strongly lensed images of the same source.

Strong lensing of GWs will provide a novel and independent way to study the matter distribution in the universe. One advantage over EM studies is that GWs do not suffer from dust extinction or anything else that might compromise the signal; GWs propagate directly from source to observer without any intervening impact (except for the curvature of space-time). The correction of dust attenuation in EM observation is a challenging and non-trivial task due to the uncertainty in dust physics [Calzetti, 1997, Calzetti et al., 2000]. Comparing to EM surveys, where it is difficult to guarantee both uniform depth and breadth even for surveys in the radio band [Adams and van Leeuwen, 2019], GW detections "hear" lensing events happening on the entire sky simultaneously, allowing us to study a clean lensing sample with well-understood and characterized selection effects. Furthermore, unlike EM sources which can be obscured or time variable, the noise power spectrum of GW detectors can be measured and the source properties are well characterized, further reducing selection effects on the lensing sample. Strong lensing of GW events are sensitive to a wide range of lensing masses, ranging from stellar mass black holes (BHs) to galaxy clusters [Takahashi and Nakamura, 2003, Li et al., 2012, Smith et al., 2018], and will provide important constraints on the underlying DM halo distribution in the universe. In this chapter, we focus on lenses at the scale of massive elliptical galaxies, since these are expected to be the dominant strong lenses. For these systems, the Schwarzschild radius is significantly larger than the wavelength of the GWs emitted by stellar-mass binary black holes (BBHs), and we can therefore adopt the geometric optics limit.

As mentioned above, EM surveys can use the angular separation between images to constrain the lens population [Davis et al., 2003, Chae, 2005]. However, this method does not work for GW detectors due to the large localization errors [Abbott et al., 2018]. On the contrary, GW facilities have exquisite time resolution (to fractions of a second) which is difficult to achieve in EM surveys even with time variable sources such as quasars or supernovae. We note that the angular separation is proportional to σ^2 where σ is the

velocity dispersion of the lens galaxies, while the time delay is proportional to σ^4. Therefore, time delay distributions are potentially more sensitive to the lens population than angular separation distributions. In what follows we use the time delay distribution between strongly lensed GW events as one of the primary lensing observables.

A fundamental aspect of statistical lensing is the rate of strong lensing, which depends both on the properties of the lenses and sources. Several studies have provided theoretical predictions for this rate. For present 2G aLIGO, the strong lensing event rate was found to be up to 0.5–1 yr^{-1} (Oguri [2018], Li et al. [2018], Yang et al. [2021]). These results are consistent with the current non-detection of lensing events during the first two observing runs [Hannuksela et al., 2019, McIsaac et al., 2020, Kim et al., 2020] and the first half of the third one [Abbott et al., 2021].[1] The chances of strong lensing will increase with future sensitivity upgrades, as a higher redshift implies a larger probability of lensing. 2G detectors are expected to be upgraded beyond design sensitivity (A+), which will allow the detection of GW source out to redshift of $z \sim 3$ [see Fig. 3 of The LIGO Scientific collaboration, 2019b]. Future 3G instruments, such as ET and CE, will be able to detect BBH sources with masses up to $10^4 M_\odot$ and at redshifts as high as $z \sim 100$ [see Fig. 2 left panel in Maggiore et al., 2020]. The enhancement in the detectable cosmological volume will greatly increase the lensing event rate, to as high as 40–$10^3\,\mathrm{yr}^{-1}$ for ET [Piórkowska et al., 2013, Biesiada et al., 2014, Ding et al., 2015, Oguri, 2018, Li et al., 2018].

In this work, we explore the capabilities of current and future GW detectors to constrain both the properties of the lens galaxies and the source population. We first compute the lensing optical depth, and calculate the lensing event rates for aLIGO, A+, ET, and CE. We further perform MC sampling to simulate the gravitational lensing of BBHs and calculate the

1. Dai et al. [2020] and Liu et al. [2020a] have found an intriguing pair, GW170104–GW170814, with masses, sky positions, and phases a priori consistent with the strong lensing hypothesis. However, other properties of the pair such as the large time delay and image type configuration make this association unlikely [Dai et al., 2020, Liu et al., 2020a]. The analysis of Abbott et al. [2021] confirms that the inclusion of selection effect and source and lens population priors drastically reduce the likelihood that this is a lensing event.

lensing properties including the time delay and magnification distributions. We then estimate our ability to constrain the typical lens velocity dispersion assuming different observation duration times and detector sensitivities. Furthermore, since the strong lensing event rate of GWs is also affected by the number of sources in the universe, we show that this information can be used as a complementary probe of the population of BBH mergers. Both detection and non-detection of GW lensing events will provide insights on the formation channels of these binaries as well as the star formation rate (SFR) and delay-time distributions.[2]

The chapter is organized as follows. In Section 4.2 we present the methods to calculate the lensing optical depth, lensing event rate, and lensing simulation, describing in detail our assumptions for both the lens and source population. In Section 4.3 we show the results for the time delay distributions and lensing rates, discussing their implications to constrain the properties of the lenses and BBH merger sources. We conclude the main results and future prospects in Section **??**. We adopt the *Planck* values for the cosmological parameters [Planck Collaboration et al., 2020].

4.2 Methods

The gravitational lensing of GWs depends both on the population of sources and lenses. In this section we describe the methodology to compute the rate of lensed signals and their properties. We begin in Section 4.2.1 with computing the probability of strong lensing as determined by the optical depth $\tau(z)$. In Section 4.2.2 we provide a prescription for the rate of the BBH merger which acts as GW sources. Fixing the lens model and the source population, we describe the simulation of lensed signals in Section 4.2.3. Finally, in Section 4.2.4 we compute the expected strong lensing event rates taking into account the effect of

2. It is important to note the distinction between the time-delay distribution and the delay-time distribution. The former refers to the amount of time between multiple images of a given strongly-lensed source, designated by δt. The latter refers to the amount of time which elapses between the formation of a binary black hole and the merger of the system, designated by Δt.

lensing magnification.

4.2.1 Lensing optical depth

The probability of a given source at $z_{\rm s}$ being strongly lensed and generating multiple images is determined by the optical depth $\tau(z_{\rm s})$ [see e.g. Schneider et al., 1992][3]. For a given lens model described by a set of parameters X, $\tau(z_{\rm s})$ depends on the multiple-image cross section $\hat{\sigma}_{\rm multiple}(z_{\rm s}, z_{\rm L}, X)$ and the density of lenses $n(z_{\rm L}, X)$ with properties X at the lens redshift $z_{\rm L}$. The lens density at redshift $z_{\rm L}$ is simply $\int n(z_{\rm L}, X)dX$. The optical depth is computed directly by adding-up the cross-sections weighted by the density at different redshifts, i.e.

$$\tau(z_{\rm s}) = \int_0^{z_{\rm s}} \int \frac{dV_c}{\delta\Omega dz_{\rm L}} n(z_{\rm L}, X)\hat{\sigma}_{\rm multiple}(z_{\rm s}, z_{\rm L}, X)\ dX dz_L \tag{4.1}$$

where $dV_c/(\delta\Omega dz_{\rm L}) = c(1+z)^2 D_{\rm L}^2/H(z)$ where $D_{\rm L}$ the angular diameter distance to the lens and $H(z)$ is the Hubble parameter.

In this chapter, we choose the singular isothermal ellipsoids (SIE) [Kormann et al., 1994, Narayan and Bartelmann, 1996, Peter Schneider, 2006] as our lens model whose lensing cross-section is determined by their velocity dispersion σ and axis ratio q_g of the galaxy. The singular isothermal sphere (SIS) model corresponds to the limit $q_g \to 1$. We neglect the shear field since we are less interested in the anisotropic distortion of the signal. Qualitatively speaking, the SIE model defines three distinct regions in terms of the number of lensing images in order of increasing area [Kormann et al., 1994]: (1) within the caustic area $\hat{\sigma}_{\rm caustic}$ 4 images form, (2) within the cut region $\hat{\sigma}_{\rm cut}$ 2 images form and (3) in any other region only 1 image forms. Therefore, we set $\hat{\sigma}_{\rm multiple} = \hat{\sigma}_{\rm cut}$.

The number density of the lens galaxies at redshift z having σ and q_g can be described

3. It is to be noted that in the limit where the cross-sections significantly overlap with each other $\hat{\sigma}_{\rm multiple}$, when $\tau > 1$, the probability of lensing is given by $P(z_s) = 1 - \exp(-\tau(z_s))$ [Cusin et al., 2019].

by:

$$n(z_L, X = (\sigma, q_g)) = \phi(\sigma|z_L)p(q_g|\sigma) \tag{4.2}$$

where $\phi(\sigma|z_L)$ is the number density of the galaxies at a given interval of σ at z_L, and $p(q_g|\sigma)$ is the distribution of the lens axis ratio for a given σ. We model $\phi(\sigma|z_L)$, with a Schechter function [Press and Schechter, 1974]:

$$\phi(\sigma|z_L) = \phi_*(z_L)\left(\frac{\sigma}{\sigma_*}\right)^{\alpha_{\rm g}} e^{-\left(\frac{\sigma}{\sigma_*}\right)^{\beta_{\rm g}}} \frac{\beta_{\rm g}}{\Gamma(\alpha_{\rm g}/\beta_{\rm g})}\frac{1}{\sigma} \tag{4.3}$$

where $\phi_*(z_L)$ is the number density of galaxies at redshift z_L. In this work, we will consider the case in which the density of galaxies is constant, $\phi_* = 8 \times 10^{-3} h^3 Mpc^{-3}$ as measured by Choi et al. [2007], but our methodology could be extended to include redshift dependence. The power-law index $\alpha_{\rm g}$ and $\beta_{\rm g}$ describe the shape of the distribution [Faber and Jackson, 1976, Tully and Fisher, 1977]. We set $\alpha_{\rm g} = 2.32$ and $\beta_{\rm g} = 2.67$ also according to the measurement of Choi et al. [2007].

For a given σ, the distribution of the lens axis ratio $p(q_g|\sigma)$ which tells the ellipticity of the lens galaxies can be described by a Rayleigh distribution [Collett, 2015, Haris et al., 2018]:

$$p(q_g|s = A + B\sigma) = \frac{1 - q_g}{s^2} \exp\left[\frac{-(1-q_g)^2}{2s^2}\right] \tag{4.4}$$

where $A = 0.38$, $B = -5.7 \times 10^{-4} (\mathrm{km/s})^{-1}$ [Collett, 2015], implying that more massive galaxies are more spherical. We set the minimum $q_{\rm g,min} = 0.2$.

The angular scale of the lensing cross-section is determined by the angular Einstein radius:

$$\theta_E = 4\pi \left(\frac{\sigma}{c}\right)^2 \frac{D_{\rm LS}}{\rm D_S}\,, \tag{4.5}$$

where $D_{\rm LS}$ is the angular diameter distance between the lens and the source, and $D_{\rm S}$ is the

angular diameter distance between the observer and the source. Apart from the geometrical configuration of the source-lens system, the Einstein radius is fully determined by the galaxy velocity dispersion, σ. This scale is the same for both SIS and SIE. The multiply-lensed cross-section for SIE is then given by:

$$\hat{\sigma}_{\rm multiple}(z_{\rm s}, z_{\rm L}, \sigma, q_g) = \theta_E^2(z_{\rm s}, z_{\rm L}, \sigma)\tilde{\sigma}_{\rm cut}(q_g), \tag{4.6}$$

where $\tilde{\sigma}_{\rm cut}(q_g)$ is the dimensionless cut cross-section given by [Kormann et al., 1994] in units of θ_E:

$$\tilde{\sigma}_{\rm cut}(q_g) \ = \frac{4q_g}{1-q_g^2}\int_{q_g}^{1}\frac{\arccos\Delta}{\sqrt{\Delta^2-q_g^2}}d\Delta. \tag{4.7}$$

This quantity depends only on q_g. Note that in the limit of a spherical lens, $q_g \to 1$, we find that $\tilde{\sigma}_{\rm cut} \to \pi$ and we recover the usual SIS cross-section. The SIS model has two regions delimited by the Einstein radius, where 2 images form inside and 1 outside; its cross-section does not depend on q_g.

Combining all of the ingredients above, we now define the optical depth for multiple images:

$$\tau(z_{\rm s}) = \int_0^{z_{\rm s}}\int_{\sigma_{\rm min}}^{\sigma_{\rm max}}\int_{0.2}^{1} 16\pi^3\frac{c(1+z_L)^2}{H(z_L)}\left(\frac{D_L D_{LS}}{D_S}\right)^2\left(\frac{\sigma}{c}\right)^4\phi(\sigma|z_L)p(q_g|\sigma)\tilde{\sigma}_{\rm cut}(q_g)dq_g d\sigma dz_{\rm L} \tag{4.8}$$

which integrates all the cross-sections of the lens galaxies between the observer and the source.

Note that in the SIS limit, the dependence on q_g disappears and one can get a closed form result by integrating in terms of Gamma functions. This result is subject to $\sigma_{\rm max}$ and $\sigma_{\rm min}$, the upper and lower bounds of the velocity dispersion of the lens galaxies. For

simplicity, we fix $\sigma_{\rm max} = \infty$ and $\sigma_{\rm min} = 0$. However, other values are possible. For example, $\sigma_{\rm min} \sim 70$km/s might be more consistent with observations [Choi et al., 2007, McConnell and Ma, 2013]. We discuss the effect of changing $\sigma_{\rm max}$ and $\sigma_{\rm min}$ on $\tau(z_s)$ in Appendix 4.4.

Adding all the pieces together, Figure 4.1 shows the optical depth $\tau(z_s)$ assuming 3 different values of σ_*. In general, $\tau(z_s)$ increases with z_s because there are more intervening galaxies between the source and the observer at higher z_s. At a given z_s, $\tau(z_s)$ increases with increasing σ_* since the lensing cross-section of the galaxy population increases with σ_*. We also find that $\tau(z_s)$ can be well-approximated by the optical depth of the SIS model ($\tau_{\rm SIS}$) multiplied by a constant factor ~ 0.96. We elaborate more on these differences in the optical depth between SIS and SIE lens model in Appendix 4.4.

4.2.2 Source population: binary black holes

Once we know how to compute the probability of strong lensing, the next ingredient is to model the population of sources. This information will be later used to simulate lensed events and to compute the lensing rates and distributions. We begin with the differential merger rate as a function of observing time t (in detectors frame) is given by

$$\frac{d\dot{N}(z)}{dz} \equiv \frac{d^2N}{dzdt}(z) = \frac{\mathcal{R}(z)}{1+z}\frac{dV(z)}{dz} \tag{4.9}$$

where $\mathcal{R}(z)$ describes the source-frame merger rate density, $\frac{dV}{dz} = 4\pi c\frac{r_c^2(z)}{H(z)}$ is the differential comoving volume, and the $(1+z)$ factor converts from source frame to detector frame. In this work, we fix the local merger rate density $\mathcal{R}(z=0) \equiv \mathcal{R}_0 = 64.9^{+75.5}_{-33.6} Gpc^{-3}yr^{-1}$ [Abbott et al., 2019].

In order to model the redshift evolution of the merger rate we will follow two complementary approaches. First, we will consider a model in which the BBHs are assumed to follow the SFR with an additional delay time. The delay time Δt is the time between the binary

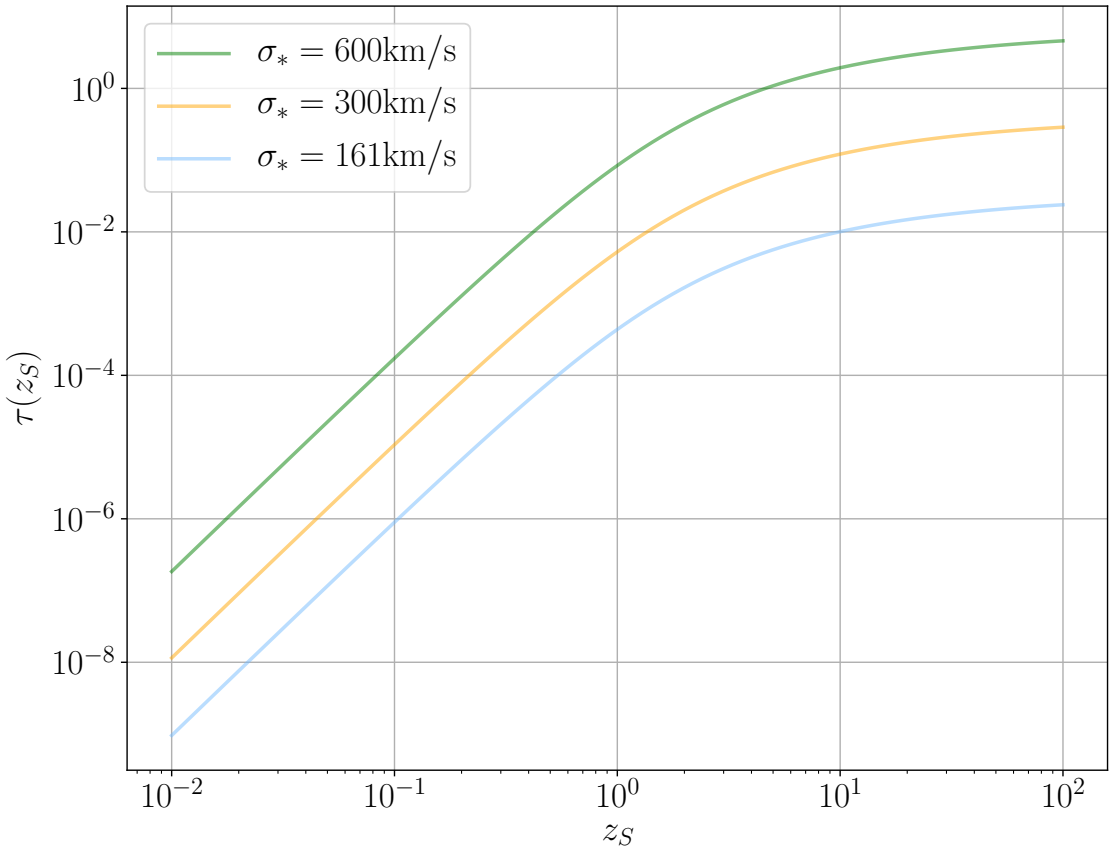

Figure 4.1: Optical depth τ as a function of source redshift z_s with different σ_* represented by different colors. Increasing σ_* will increase the velocity dispersion of the whole galaxy population, hence increase the lensing cross-sections.

formation and the final merger. This is motivated by the assumption that BBHs are formed from stars in the field and has been studied thoroughly using population synthesis codes [Belczynski et al., 2002, Postnov and Yungelson, 2014]. Observations of strongly lensed events will provide constraints on both the SFR and the delay-time. If one believes we already know the SFR, then our results probe the delay-time distribution directly. These constraints would be complementary to the ones obtained with unlensed, low-redshift binaries [Fishbach and Kalogera, 2021]. Alternatively, prior knowledge of the delay-time distribution would allow for direct constraints on the SFR of the sources. In our analysis, we consider three different scenarios for the SFR and delay-time distribution, to explore the impact that these have on our results. In the main text of the chapter, we adopt the SFR model from Madau and Dickinson [2014] (MD14) with minimal delay time $\Delta t_{\rm min}$= 50 Myr. We discuss two additional scenarios in the Appendix 4.5: MD14 SFR model with a different delay time of $\Delta t_{\rm min}$= 1 Gyr, and a different SFR density which is constant throughout the redshift evolution $\dot{\rho_*} = 0.004, M_\odot Mpc^{-3} yr^{-1}$ with $\Delta t_{\rm min}$= 50 Myr. The detailed calculation of the rate from the SFR to detector-frame merger rate is described in Appendix 4.5.

Our second approach will be to extend this fixed model by varying its elements in a convenient parametrization from Callister et al. [2020]:

$$\mathcal{R}(z|z_p, \alpha, \beta) = \mathcal{C}(\alpha, \beta, z_p) \frac{\mathcal{R}_0 (1+z)^\alpha}{1 + (\frac{1+z}{1+z_p})^{\alpha+\beta}} \tag{4.10}$$

where $\mathcal{C}(\alpha, \beta, z_p) = 1 + (1+z_p)^{-\alpha-\beta}$. Equation 4.10 is proportional to $(1+z)^\alpha$ at low redshift and $(1+z)^\beta$ at high redshift. z_p is the redshift at the peak of the distribution, and the local merger rate $\mathcal{R}(z=0) = \mathcal{R}_0 = 64.9^{+75.5}_{-33.6} Gpc^{-3} yr^{-1}$ is fixed [Abbott et al., 2019]. The second approach will be relevant when quantifying how the source population affects the lensing rate, as discussed in Section 4.3.4. We note that alternate formation channels might be described with differing values of α, β, z_p, and $\mathcal{R}_0$, or with entirely different functional

forms. These could be combined to generalize our approach; for this chapter we describe the aggregate population with a single distribution shown in Equation 4.10.

In order to calculate how many of these BBH mergers are detected, we need to consider the detection probability, $p_{\rm det}(\mathcal{M}, q, z)$, which takes into account the detector sensitivity and selection bias for binaries with different masses and redshifts. We parametrize the source masses in terms of the chirp mass, $\mathcal{M} = (m_1 m_2)^{3/5}/(m_1 + m_2)^{1/5}$, and mass ratio, $q = m_2/m_1$, where m_1 is the mass of the heavier BH, $m_1 > m_2$. The detected merger event rate within redshift z is given by:

$$\dot{N}_{\rm BBH}(z) = \int_0^z \int_{\mathcal{M}_{min}}^{\mathcal{M}_{max}} \int_0^1 \frac{d\dot{N}(z)}{dz} p(\mathcal{M}, q) p_{\rm det}(\mathcal{M}, q, z)\, dq\, d\mathcal{M}\, dz\,, \tag{4.11}$$

where $p(\mathcal{M}, q)$ is the 2-dimensional distribution of $\mathcal{M}$ and q. We assume m_1 follows a power-law distribution $p(m_1) \propto m_1^{-0.4}$ and m_2 is uniformly distributed in range $m_{\rm min} < m_2 < m_1$. We fix $m_{\rm min} = 5M_\odot$ and $m_{\rm max} = 41.6M_\odot$ following the results of the first and the second observing run of Advanced LIGO and Advanced Virgo [Abbott et al., 2019]. We derive the distribution of $\mathcal{M}$ and q by randomly drawing m_1 and m_2 and then linearly interpolate the 2-dimensional probability density function (PDF) to get $p(\mathcal{M}, q)$, and also the corresponding minimum and maximum $\mathcal{M}$, $\mathcal{M}_{\rm min}$ and $\mathcal{M}_{\rm max}$. We note that the latest LIGO–Virgo catalog, GWTC-2, provides a more complex description of the mass distribution [Abbott et al., 2020b] and in fact this simple power-law model is disfavored by observations. However, for the purposes of our analysis this simplified description is sufficient.

We determine the probability of detecting a given source by the fraction of events across all possible sky-locations, orientations, and inclinations that are above a given signal to noise threshold $\rho_{\rm thr}$. For a particular detector/detector network this is a known function [Dominik et al., 2015]:

$$p_{\rm det}(\mathcal{M}, q, z) = P(w = \rho_{\rm thr}/\rho_{\rm opt}(\mathcal{M}, q, z))\,, \tag{4.12}$$

where $\rho_{\rm opt}(\mathcal{M}, q, z)$ is the S/N for an optimally located and oriented binary. The function $P(w)$ is a cumulative distribution function which gives the fraction of the sources with a given $\mathcal{M}, q$ and at a given redshift z that can be detected, assuming the sky location and the orientation angles are uniformly distributed. We take the interpolated function in Dominik et al. [2015] fitted from the numerically generated Monte Carlo sample of 10^9 binaries. We focus on a single detector with threshold of $\rho_{\rm thr} = 8$ and consider 4 sensitivies: aLIGO [Abbott et al., 2015], aLIGO at upgraded sensitivity (A+) [The LIGO Scientific collaboration, 2019a] and the third generation detector Einstein Telescope (ET) [Maggiore et al., 2020] and Cosmic Explorer (CE) [Reitze and Adhikari, 2019].[4] We do not take into account the duty cycle and assume that the detectors are always online.

4.2.3 Simulating strongly lensed GW events

Having fixed the lens model (SIE model) and the source population (BBHs consistent with LIGO/Virgo O2), we now describe our method for generating the sample of strong lensing events. We adopt a semi-analytical approach similar to that in Haris et al. [2018] which randomly generates lens systems and solves the corresponding lens equations. The detailed procedure of the MC simulation can be found in Section 2 of Appendix A in Haris et al. [2018]. We highlight the differences in our simulation below:

1. We sample the BBH mass m_1 and m_2 using the distribution described in Section 4.2.2.

2. We pick the source redshift (z_s) based on the PDF normalized from the BBH merger rate as a function of redshift $\dot{N}_{\rm BBH}(z)$ calculated in Section 4.2.2.

3. Since we want to constrain lens parameter σ_*, we directly pick velocity dispersions of the galaxy lenses based on the PDF normalized from the Schechter function in

4. The sensitivity curve ($S_h(\mathrm{Hz}^{-1/2})$) for different detectors are from: https://dcc.ligo.org/LIGO-T1500293-v11/public

Equation 4.3 with varying σ_* values instead of setting $\sigma_* = 161$km/s as in Haris et al. [2018].

4. Our lensing simulation assumes that multiple images of the same source have independent detector selection effects. Since lensed images of the same source arrive at different times, the relative angles between the detector and the source will have changed, and thus the detector response will be different for the two images. We note, however, that since the images come from the same binary source, the intrinsic angles of the binary source will be the same. It is computationally expensive to incorporate this, and since we do not expect these correlations to qualitatively impact any of our results, we neglect them. To determine whether a lensing image can be detected or not, we generate one random number for each image respectively. If the random number is smaller than $P(w = \rho_{\rm thr}/\sqrt{\mu}\rho_{\rm opt})$, we consider the image have been detected. Yang et al. [2019] show that incorporating the Earth's rotation decreases the lensing event rate by $\sim 10\%$ for the case of BBHs.

After picking the parameters for the sources and the lens galaxies, we follow the procedure in Haris et al. [2018] and randomly draw $z_{\rm L}$ and pick the source-plane location where we can find multiple images. We obtain the image positions $x_{1,i}$ and $x_{2,i}$ for the i-th image (i=1, 2 for the case with 2 images, or i=1, 2, 3, 4 for case with 4 images) by solving the lens equations (see Equations 11–14 in Haris et al. [2018]) and calculate the magnification for each image:

$$\mu_i = \left(1 - \sqrt{\frac{q_g}{x_{1,i}^2 + q_g^2 x_{2,i}^2}}\right)^{-1} \tag{4.13}$$

and the time delay for ith image relative to a reference time (see more details in Kormann et al. [1994]):

$$\delta t_i = 16\pi^2 \frac{D_c(z_L)}{c} \left(\frac{\sigma}{c}\right)^4 \left(1 - \frac{D_c(z_L)}{D_c(z_s)}\right) \Phi_i \tag{4.14}$$

where $D_c(z_s)$ is the comoving distance of the source, $D_c(z_L)$ is the comoving distance of the lens, and Φ_i is the Fermat potential [Blandford and Narayan, 1986].

One of the goals of this work is to explore the ability of GW detectors to constrain the characteristic galaxy velocity σ_* by observing the time delay (δt) distribution of multiply-lensed events. In particular, we focus on the time delay between two detected lensing images from the same source:

$$\delta t = |\delta t_1 - \delta t_2| \propto \sigma^4 \,. \tag{4.15}$$

In most of the cases, these two images correspond to the primary (the brightest image, or the one with the highest magnification) and the secondary image (the second-brightest image) except for some very rare cases. This time delay δt should not be confused with the delay time Δt between the formation and merger of binary black holes introduced in Section 4.2.2.

Since δt_i is proportional to σ^4 according to Equation 4.14, the time delay distribution is very sensitive to the value of σ_*. By comparing the observed δt distribution with the theoretical prediction for different σ_*, we can then constrain the value of σ_*. We present the PDF distribution of δt for 3 different σ_* in Figure 4.4. When σ_* is high, the δt distribution extends to higher values. For the case of $\sigma_* = 600$km/s the tail of the δt distribution extends to even 15 years. To facilitate the visualization, we zoom in to the range < 1 year in the inset of the same figure. In general, higher σ_* has a higher probability of high δt values. The cumulative distribution function (CDF) also has noticeable differences. The δt at which 90 % of the events are included for $\sigma_* = 161, 300, 600$km/s are 0.16, 1.77, and 25.72 years.

To constrain σ_* using GW lensing events, we perform a Kolmogorov-Smirnov (KS) test which is a widely used statistical technique to quantify the difference between the model and the data. The KS test computes the distance between the CDF of the model and the empirical probability distribution (EDF) of the data [Kolmogorov, 1933, Smirnov, 1948]. The maximum distance is defined as the KS statistic value. Bigger KS statistic indicates that the 2 input distributions may have different origins. If a continuous expression for the

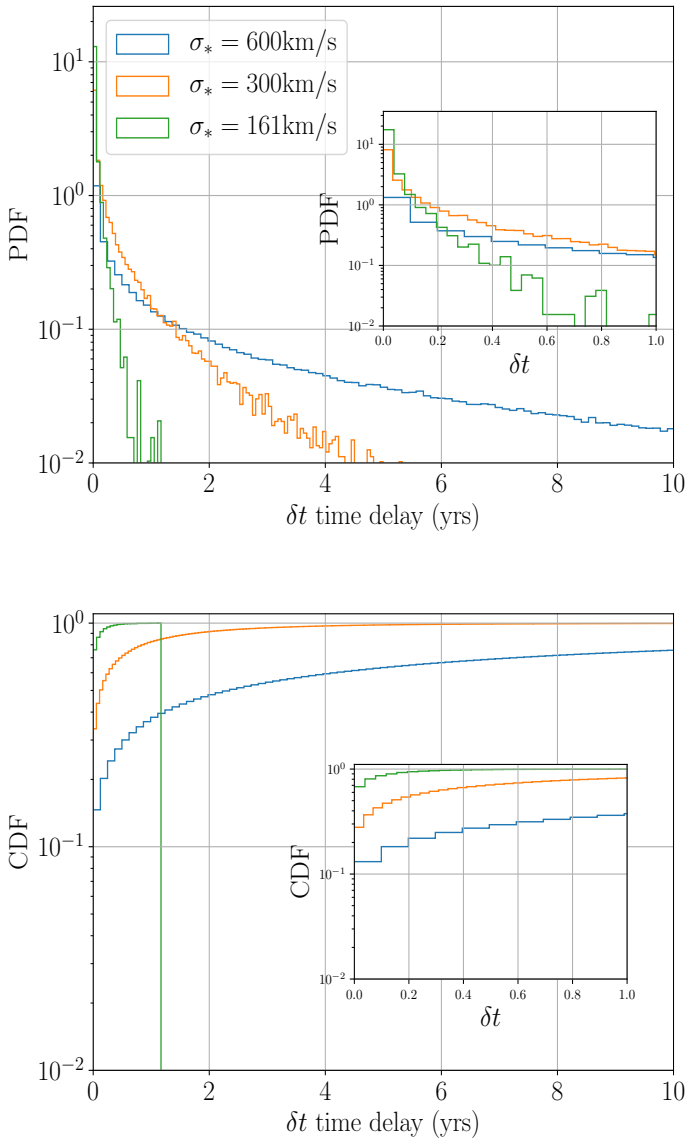

Figure 4.2: Lensing time delay δt distribution for strong lensing pairs observed by ET for $\sigma_* = 161, 300, 600$ km/s assuming 10^7 BBH sources. The top panel displays the PDF, while the bottom one plots the CDF. Time delay extends to higher values when we increase σ_*. The proportionality between time delay and σ is described in Equation (4.14). The green CDF ($\sigma_* = 161$km/s) truncates at the maximum δt. We generate the BBH population using the MD14 SFR model [Madau and Dickinson, 2014] assuming merger delay time distribution $P(\Delta t) \propto 1/\Delta t$ ranging from 50 Myr to 13.5 Gyr (See more details in Section 4.2.2).

model CDF is not available, we can apply the two-sample KS test which uses EDF of the theoretical data set instead of the CDF. Since we do not have an analytical expression for the lensing δt distribution and we do not want to add additional uncertainties by fitting the theoretical δt distribution from the simulations, we adopt two-sample KS test in the following analysis.

Operationally, we generate mock observation samples and compare them with the theoretical δt distribution to get a distribution of KS test statistics. We denote the σ_* used for generating the theoretical δt distribution as $\sigma_{*,A}$, and for the mock observation distribution as $\sigma_{*,B}$. The KS statistic distribution from comparing the theoretical distribution with $\sigma_{*,A}$ and the mock observation distribution with $\sigma_{*,B}$ is expressed as KS($\sigma_{*,A}$, $\sigma_{*,B}$). We use the KS statistics when $\sigma_{*,A} = \sigma_{*,B}$ (i.e. KS($\sigma_{*,B}$, $\sigma_{*,B}$)) as a reference. If the majority of the KS($\sigma_{*,A}$, $\sigma_{*,B}$) derived from observation samples are greater than the majority of KS($\sigma_{*,B}$, $\sigma_{*,B}$), then it indicates that $\sigma_{*,B}$ is actually quite different from $\sigma_{*,A}$, implying the observed σ_* is inconsistent with the theoretical prediction.

The size of each lensing δt distribution sample is determined by the BBH merger rate, the optical depth, the observation duration time, and the detector sensitivity. Due to the low lensing event rate of aLIGO and A+, we only discuss the possibility of using δt distribution to constrain galaxy population using 3G detectors. In particular we concentrate on ET as an example, although similar results are expected for CE. The lensing time delay can sometimes be larger than the observation duration time. In order to make the sample realistic, we exclude the sources that have time delay greater than the observation duration time.

We generate the theoretical δt distributions by simulating a large (10^7) number of sources. For the mock observation samples, we set the number of sources going into our simulation using the product of the BBH merger rate per year as calculated in Section 4.2.2 and the observation duration time ranging from 1 year, 5 years, and 10 years.

As a summary, we follow the procedure below to test the consistency of the model and

the mock sample:

1. For a given observation duration time, we generate 500 mock δt distribution samples for a given lens galaxy population with $\sigma_{*,B}$. We exclude the sources that have time delay greater than the observation duration time.

2. We compare these mock samples with the theoretical δt distribution using the KS test. For a given observation time, $\sigma_{*,A}$, and $\sigma_{*,B}$, we can get 500 KS statistic values and derive their corresponding PDF.

3. We use the PDF of the KS test values for the case where $\sigma_{*,A} = \sigma_{*,B}$ as the reference distribution. The distribution of KS test statistics shifts to larger values when $\sigma_{*,A} \neq \sigma_{*,B}$. We can also compute the distribution of the ratio of the KS statistics $\mathrm{KS}(\sigma_{*,A} = \sigma_{*,B},\ \sigma_{*,B})/\mathrm{KS}(\sigma_{*,A},\ \sigma_{*,B})$. Most of the time the ratio should be smaller than 1 because the mock samples are usually closer to the theoretical models with the same value of σ_*. However, sometimes due to the limitation of the observation time, the observation sample may appear closer to the wrong model. We define the area where the PDF of this ratio is smaller than 1 as the probability of correct inference. We show how the probability of correct inference evolves with the observation duration time in Section 4.3.3.

In addition to the δt distribution, another interesting observable is the relative magnification distribution: the ratio of the magnification of the secondary image μ_2 and the primary image μ_1, μ_2/μ_1. Since it is not directly related with σ_* but more sensitive to the ellipticity of the lenses, we discuss them in the Appendix 4.7. It would be interesting to combine both observables in future analyses to constrain the lens population more comprehensively.

4.2.4 Computing strong lensing event rates

In this section, we focus on the calculation of the *observed* GW strong lensing event rate $\dot{N}_{\rm lensing}$. To achieve this, we need to take into account how many merging sources are multiply-imaged, as well as which of these sources are detectable. We thus include both the optical depth $\tau(z)$ and the magnification distribution $P(\mu)$ into the integration in Equation (4.11):

$$\dot{N}_{\rm lensing}(z) = \int_0^z \int_{\mathcal{M}_{min}}^{\mathcal{M}_{max}} \int_0^1 \int_{\mu_{min}}^{\mu_{max}} \tau(z) \frac{d\dot{N}(z)}{dz} p(\mathcal{M}, q) p_{\rm det}(\mu, \mathcal{M}, q, z) P(\mu) d\mu dq d\mathcal{M} dz \tag{4.16}$$

where $p_{\rm det}(\mu, \mathcal{M}, q, z)$ is modified due to the magnification factor μ as follows:

$$p_{\rm det}(\mu, \mathcal{M}, q, z) = P\left(w = \frac{\rho_{\rm thr}}{\sqrt{\mu}\rho_{\rm opt}(\mathcal{M}, q, z)}\right) , \tag{4.17}$$

where we have changed $\rho_{\rm opt}$ to $\sqrt{\mu}\rho_{\rm opt}$. This is because magnifying a source with factor μ is equivalent to decreasing the source luminosity distance by a factor of $1/\sqrt{\mu}$, and the luminosity distance enters in the signal-to-noise via $\rho \propto 1/d_L$.

The values and meaning of the strong lensing event rate depends critically on the choice of the magnification distribution $P(\mu)$. For example, Oguri [2018] uses two differing magnification distribution when calculating $\dot{N}_{\rm lensing}$. The first way is treating all the images from the same BBH source as a single group and use the sum of the magnification values as the total magnification. Another way is treating individual images differently which means defining $P(\mu)$ using the magnification value of each image regardless of the source. Dai et al. [2017] propose a fitting to the magnification PDF at different redshifts based on the simulations in Hilbert et al. [2008] and Takahashi et al. [2011]. Li et al. [2018] adopts the magnification of the fainter image in the case of double images and that of the third brightest image in

the case of four lensing images. Many other works (e.g. Ng et al. [2018], Diego [2019], etc) prefer using a simple analytical form of $P(\mu) \propto \mu^{-3}$ to describe the tail of the magnification distribution at high values, typically applied for $\mu > 2$.

In real observations, the identification of strongly lensed GW events is not an easy task. One needs to statistically asses if the parameters of each possible image favor the lensing hypothesis over the non-lensed hypothesis [Hannuksela et al., 2019]. This is typically achieved by searching for overlaps in the sky maps, masses, and spins. However, this overlap in binary paramter space can also happen in non-lensed events due to selection effects and observational errors. In addition, one could also identify lensed GW event alone without associating it with other events by measuring the phase distortion with respect to the unlensed predictions in general relativity. However, this is only applicable for type II images which are created at the saddle points of the time delay surface. They have a phase shift of $\pi/2$ which modifies the phase evolution when higher modes, precession or eccentricity are present [Dai and Venumadhav, 2017, Ezquiaga et al., 2020]. 3G detectors could be sensitive to these distortions, identifying type II images directly [Wang et al., 2021]. Although identifying type II images individually could help constraining the optical depth, in order to measure the time delay distribution we need to identify at least two images of the same source. It is important to remember that the first image, typically the brightest one, is always at the minimum of the time delay surface (type I) [Blandford and Narayan, 1986] and thus cannot be identified individually.

Considering above, we calculate two kinds of lensing event rates. The first one is the number of lensed systems whose primary images are detected per year, denoted as $\dot{N}_{\rm lensing,1st}$. The second one is the lensing event rate when at least 2 images are detected for each lensing system, $\dot{N}_{\rm lensing,2nd}$. The first quantity $\dot{N}_{\rm lensing,1st}$ is useful to understand how the observed BBH population is "polluted" by magnified events, since the primary images with the largest magnification are the most likely ones that can be detected but may not be identified

as lensing events if we miss the other images associated with the same source. To calculate $\dot{N}_{\rm lensing,1st}$, we use the magnification distribution of the primary image $P(\mu)_{\rm 1st}$ when doing the integration in Equation 4.16. The second quantity $\dot{N}_{\rm lensing,2nd}$ is useful to know how many multiply-lensed events we can detect for studying δt distribution. To estimate this one, we use the magnification distribution of the secondary image $P(\mu)_{\rm 2nd}$. The idea is that if the secondary image can be detected, then the primary image is very likely to be detected as well since by definition the primary image should have a higher $\sqrt{\mu}\rho_{\rm opt}$. Nevertheless, we notice that due to the difference in arrival times, the orientation angle of the detector will change before the second image arrives. There is a possibility that we detect the secondary image but the first one arrives when the orientation of the detector network is less favorable. It is also likely that the first one is missed because the detector is not online but in this chapter we assume the detector observes whole year. However, we show in Appendix 4.6 that this procedure still gives a very good estimation of $\dot{N}_{\rm lensing,2nd}$ when comparing to our lensing simulations.

In practice, we obtain $P(\mu)_{\rm 1st}$ and $P(\mu)_{\rm 2nd}$ from our lensing simulation by recording the magnification of the brightest image and the second-brightest image of each lensing system. We compute the histograms of μ_1 and μ_2 and linearly interpolate them for $\mu < 3$. We smoothly connect them with a power law μ^{-3} for $\mu > 3$, as it is universally expected for large magnifications. Figure 4.3 shows the results. It is to be noted that the distribution of secondary images extends to $\mu_2 < 1$. This is because the secondary images of SIE model are very close to the lens center and thus are highly de-magnified [Kormann et al., 1994]. On the other hand, the primary image magnification distribution peaks at $\mu \sim 2$. We summarize our results in Section 4.3.1.

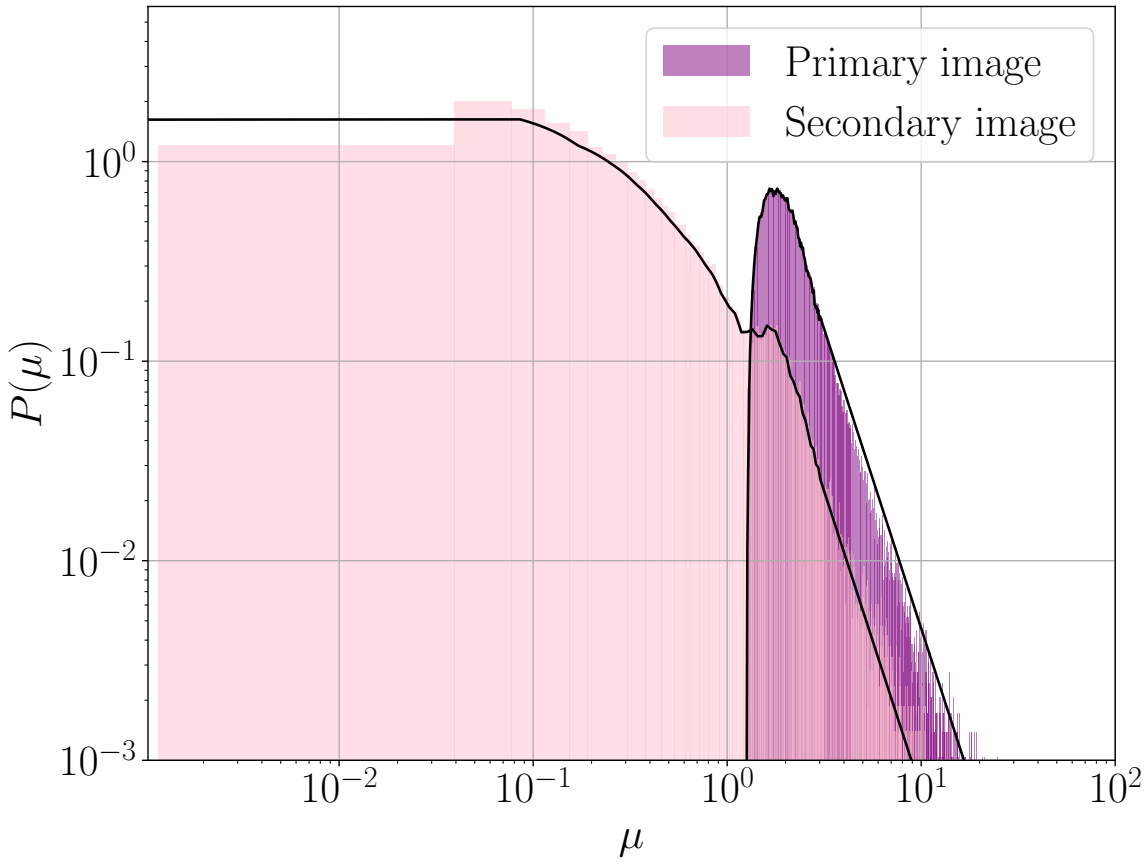

Figure 4.3: Magnification distribution, $P(\mu)$, obtained from our MC simulations of GWs lensed by SIE lenses. Purple and pink histograms correspond to the primary ($P(\mu)_{\rm 1st}$) and secondary ($P(\mu)_{\rm 2nd}$) images, which correspond to the brightest and second-brightest images respectively. We compute $P(\mu)$ by linearly interpolating the histogram for $\mu < 3$ and smoothly connect it with a power-law function $P \propto \mu^{-3}$ for $\mu > 3$. The final $P(\mu)$ we use in Equation 4.16 are marked by black solid lines. We set $\mu_{\rm min}$ and $\mu_{\rm max}$ based on the $P(\mu)$ derived from the lensing simulation.

4.3 Results

In the previous section we have introduced our procedure for calculating lensing event rates and lensing distributions given a lens and source population and a detector sensitivity. In this section we present our results and discuss how the lens and source populations affect the lensing observables, particularly the lensing event rate as a function of redshift and the lensing time delay distribution. We also examine the capacity of present and future detectors to probe these lens and source parameters.

We show the calculation of the lensing rates and its dependence on lens velocity dispersion parametrized by σ_* in Section 4.3.1. In Section 4.3.2 we show how the detectable cosmological volume is expanded by the detection of lensing events. Section 4.3.3 demonstrates the potential constraints on σ_* from the time delay distribution. Lastly, we discuss how the lensing event rate is affected by variations in the source population in Section 4.3.4.

4.3.1 Lensing event rate

As we can see from the calculation in Sections 4.2.1, 4.2.2, and 4.2.4, when fixing the SFR, the local merger rate density $\mathcal{R}_0$, and the lens galaxy density ϕ_*, the lensing event rate will be primarily determined by σ_*. We show the dependence of $\dot{N}_{\text{lensing, 1st}}$ and $\dot{N}_{\text{lensing, 2nd}}$ on σ_* for both 2G and 3G detectors in Figure 4.5 and summarize the lensing event rate for the case of $\sigma_* = 161\text{km/s}$ in Table 4.1.

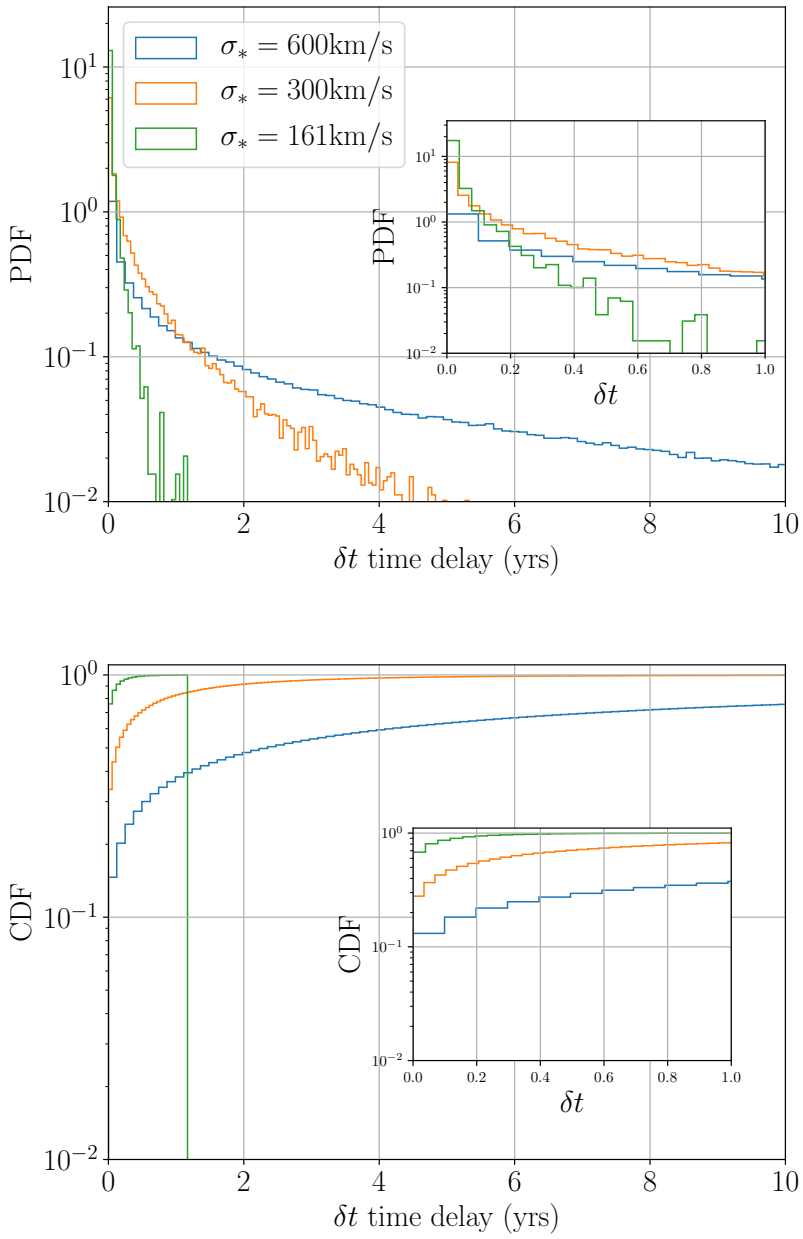

Figure 4.4: Lensing time delay δt distribution for strong lensing pairs observed by ET for $\sigma_* = 161, 300, 600$ km/s assuming 10^7 BBH sources. The top panel displays the PDF, while the bottom one plots the CDF. Time delay extends to higher values when we increase σ_*. The proportionality between time delay and σ is described in Equation (4.14). The green CDF ($\sigma_* = 161$km/s) truncates at the maximum δt. We generate the BBH population using the MD14 SFR model [Madau and Dickinson, 2014] assuming merger delay time distribution $P(\Delta t) \propto 1/\Delta t$ ranging from 50 Myr to 13.5 Gyr (See more details in Section 4.2.2).

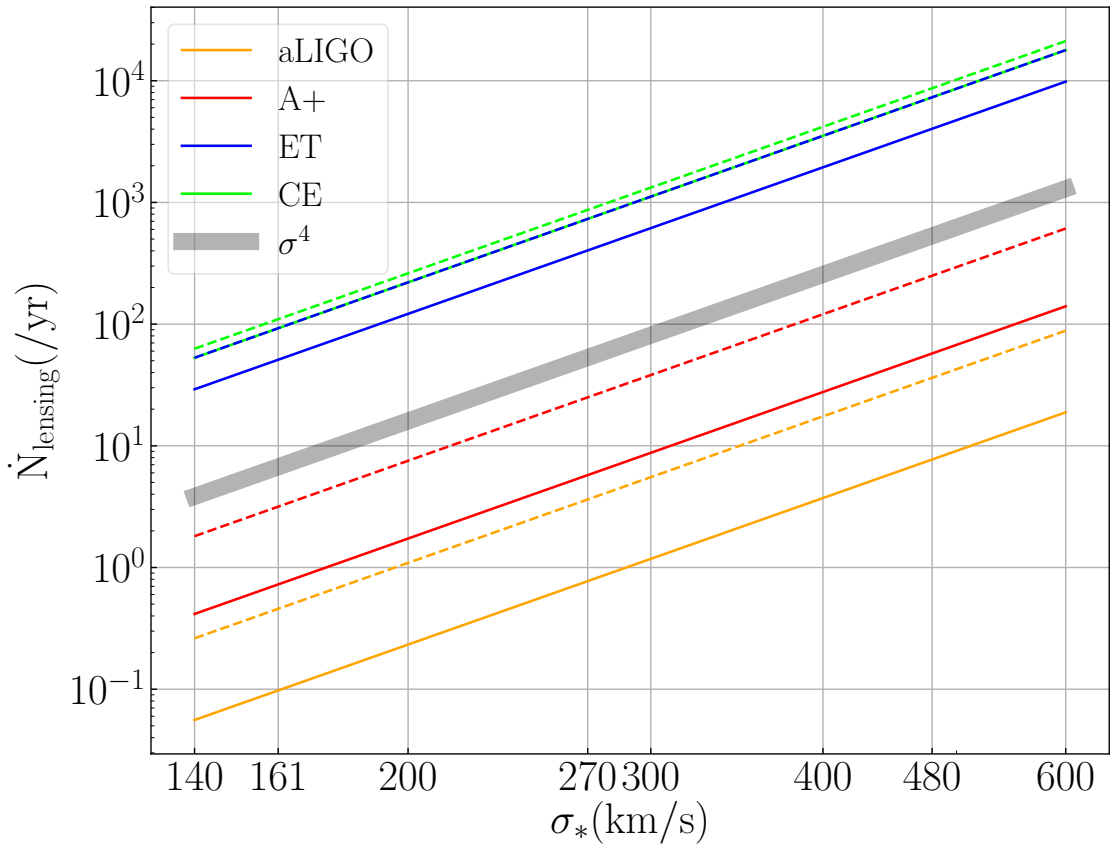

Figure 4.5: Predictions for the observed rate of the primary images $\dot{N}_{\rm lensing,1st}$ (dashed lines) and events with multiple images $\dot{N}_{\rm lensing,2nd}$ (solid lines). Different colors represent different detectors. We set the SFR model to MD14 (Madau and Dickinson [2014]) with a minimum merger delay time $\Delta t_{\rm min} = 50$ Myr, the galaxy number density to $\phi_* = 8 \times 10^{-3} h^3 Mpc^{-3}$ [Choi et al., 2007], and use local BBH merger rate constrained by LIGO O2 $\mathcal{R}_0 = 64.9^{+75.5}_{-33.6} {\rm Gpc^{-3} yr^{-1}}$ [The LIGO Scientific collaboration, 2019a]. $\dot{N}_{\rm lensing}$ is linearly dependent on ϕ_* and $\mathcal{R}_0$, and is proportional to σ_*^4. We also plot the grey line to mark the σ_*^4 trend.

	Primary image ($\dot{N}_{\rm lensing,1st}$)	Multiply-imaged events ($\dot{N}_{\rm lensing,2nd}$)	Unlensed BBH merger events ($\dot{N}_{\rm BBH}$)
aLIGO	0.45	0.1	6.3×10^2
A+	3.4	0.7	3.7×10^3
ET	93	51	1.2×10^5
CE	110	92	1.5×10^5

Table 4.1: Lensing event rate ($\dot{N}_{\rm lensing}$, yr^{-1}) assuming $\sigma_* = 161$ km/s [Choi et al., 2007]. We use SIE lens model for the calculation. We use MD14 as SFR model and set $\Delta t_{\rm min} = 50$ Myr. The 3 columns correspond to the lensing event rate of the primary image detected ($\dot{N}_{\rm lensing,1st}$), the lensing event rate with at least 2 images detected($\dot{N}_{\rm lensing,2nd}$), and the expected observed BBH merger event per year $\dot{N}_{\rm BBH}$ without considering magnification.

Figure 4.5 shows that both $\dot{N}_{\rm lensing,\ 1st}$ and $\dot{N}_{\rm lensing,\ 2nd}$ increase with σ_*, and are almost linearly dependent in log-space, $\log \dot{N}_{\rm lensing} \propto 4 \log \sigma_*$. This is mainly because $\tau(z) \propto \sigma_*^4$. By increasing the value of σ_*, the σ of the whole lens galaxy population increases. Therefore, the overall cross-sections of lensing increases which results in higher $\dot{N}_{\rm lensing}$. Moreover, $\dot{N}_{\rm lensing}$ grows with the detector sensitivity since more sensitive detectors can observe a larger cosmological volume. We discuss the redshift distribution of lensed and unlensed events in more detail in Section 4.3.2.

Table 4.1 summarizes the expected $\dot{N}_{\rm lensing}$ using velocity dispersion $\sigma_* = 161$ km/s constrained from SDSS in the EM band [Choi et al., 2007]. We assume the MD14 SFR model and a minimum delay time of $\Delta t_{\rm min} = 50$ Myr. Our calculation shows that the contribution of the lensing events to the overall merger events is small, with a fraction of $\lesssim 0.1\%$. The majority of the events that we detect should be unlensed events. Since we want to measure the time delay distribution, we are interested in events that have at least 2 images detected. The second column shows the estimation of $\dot{N}_{\rm lensing,\ 2nd}$. According to these results, a statistical study of GW lensed events will happen with 3G detectors. Moreover, Appendix 4.5 shows results for two alternate SFR scenarios: MD14 SFR model with a different delay time of $\Delta t_{\rm min}$= 1 Gyr, and a different SFR density which is constant throughout the redshift evolution $\dot{\rho_*} = 0.004 M_\odot Mpc^{-3} yr^{-1}$ with the same $\Delta t_{\rm min}$= 50 Myr. As an additional check, in Appendix 4.6 we compare the results in Table 4.1 with the lensing event rates directly obtained from a lensing simulation. We find consistent results.

4.3.2 Detectable cosmological volume increased by lensing magnification

Since some of the BBH merger events at high redshift, which were previously too faint to be detected, can be magnified above the detection threshold, the detection volume of the GW detectors will increase due to lensing. Figure 4.6 shows the redshift distribution of the unlensed events, the primary images ($\dot{N}_{\rm lensing,1st}$) which trace events with only one

	Unlensed events	Primary images	Multiple images
aLIGO	0.9	2.8	2.7
A+	1.4	3.1	3.0
ET	3.8	5.1	4.8
CE	4.1	5.2	5.1

Table 4.2: Redshift within which 90 % of the unlensed events, $\dot{N}_{\rm lensing,1st}$ and $\dot{N}_{\rm lensing,2nd}$ are included.

image detected, and the secondary images ($\dot{N}_{\rm lensing,2nd}$) which trace the events with multiple images. Table **??** summarizes the characteristic redshift within which 90% of the events are included. The characteristic redshifts for aLIGO and A+ increase from ~ 1 to ~ 3, indicating that the detectable cosmological volume is drastically increased by lensing events, although as shown before, lensed events will only represent a very small fraction of the catalog. The same effect, however, is less significant for 3G detectors. The characteristic redshift for ET and CE increases from ~ 4 to ~ 5. This is mainly because: 1) GW sources at high redshift need higher magnification to be brought within the horizon than their low-redshift counterparts; and 2) since star formation generally peaks at $z \sim 2$ and drops at higher redshift, there are fewer BBH sources at $z > 5$ as seen in Figure 4.13, and therefore the increase in detectable volume due to lensing is slight. Moreover, the redshift distributions are insensitive to the change in σ_*, since we assume the lens galaxy population does not evolve with redshift in this chapter. Therefore σ_* mainly affects the normalization of the lensing rate rather than the shape of the lensing optical depth with redshift. We leave the incorporation of the redshift evolution of the lens galaxy population to future work.

4.3.3 Constraining galaxy populations using time delay distributions

As mentioned in Section 4.2.3, the lensing time delay δt is directly related to the galaxy velocity dispersion σ according to Equation 4.14, and thus can be used as a probe of the lensing population. The δt distribution has a stronger dependence on σ_* than the lensing rate, $\dot{N}_{\rm lensing}$, because $\dot{N}_{\rm lensing}$ is also affected by the number density of the lens galaxy

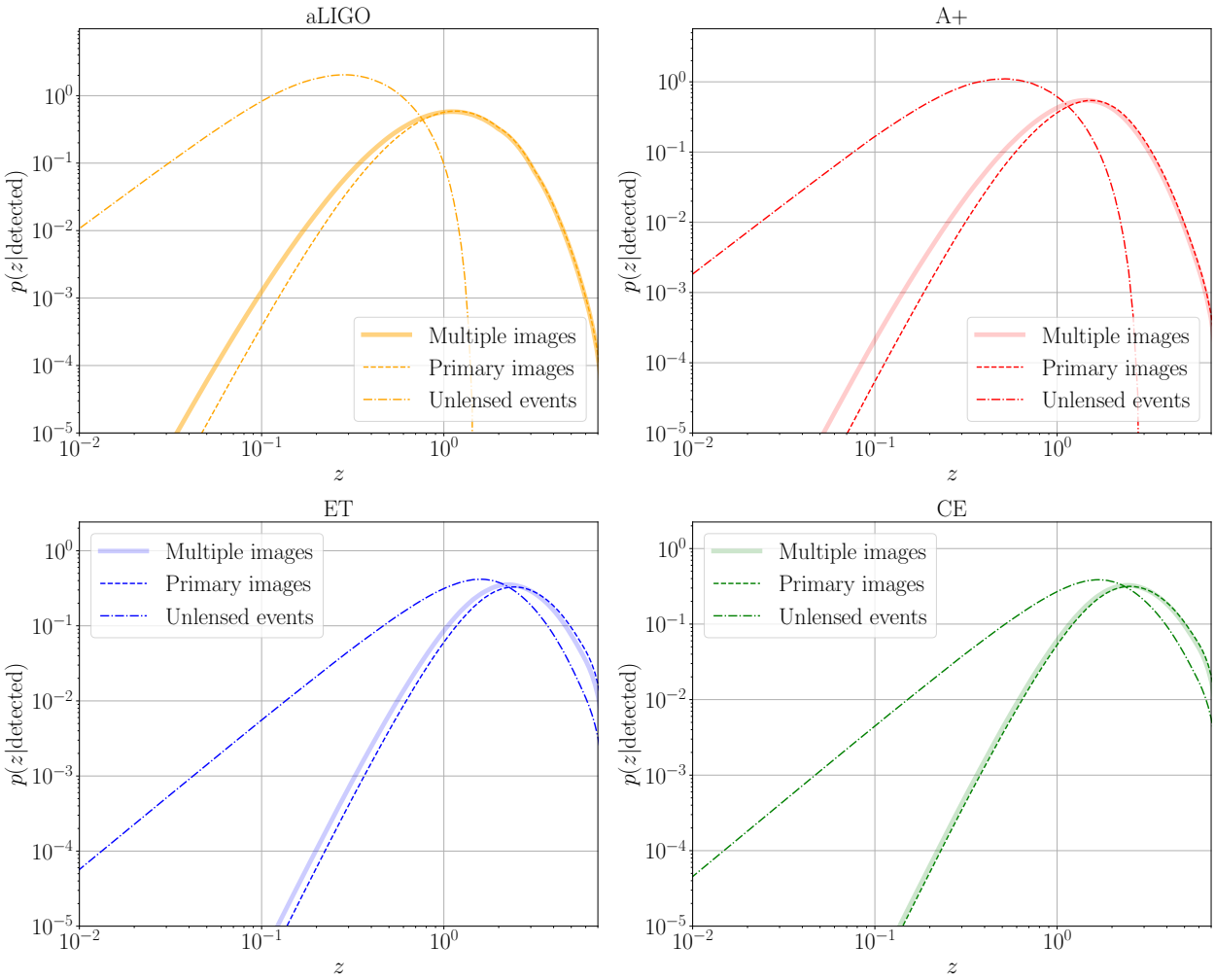

Figure 4.6: The redshift distribution of the unlensed images (dashed-dotted line, distribution of $\dot{N}_{\mathrm{BBH}}$), primary images (dashed line, distribution of $\dot{N}_{\mathrm{lensing,1st}}$), and multiple lensed images (solid line, distribution of $\dot{N}_{\mathrm{lensing,2nd}}$). We set $\sigma_* = 161\mathrm{km/s}$ but the redshift distribution is not sensitive to σ_*. The characteristic redshifts within which 90 % of the events are included for different scenarios are summarized in Table **??**.

(ϕ_*) and the BBH source population. Since different galaxy populations give different δt distribution, we can use this fact to inversely constrain σ_* from measuring the δt distribution. As described in Section 4.2.3, we simulate the lensing process assuming a range of values for σ_*, and record the output time delay for each lensing system. Our simulations show that for aLIGO and A+ only a few lensing events will be detectable per year. Therefore, we only consider the measurements of the time delay distribution for 3G detectors, using ET as an example.

Figure 4.7 provides an example of constraining galaxy properties using the time delay distribution. We generate 500 mock observation samples with $\sigma_{*,B} = 161$ km/s for 3 different observational durations (1 year, 5 years, and 10 years), and compare them with two theoretical models ($\sigma_{*,A} = 161\,\mathrm{km/s}$ and $\sigma_{*,A} = 171\,\mathrm{km/s}$). The corresponding KS test statistics are denoted as KS($\sigma_{*,A} = 161$ km/s, $\sigma_{*,B} = 161\,\mathrm{km/s}$) and KS($\sigma_{*,A} = 171$ km/s, $\sigma_{*,B} = 161\,\mathrm{km/s}$) whose distributions are shown in the green and cyan histograms in the upper panels of Figure 4.7. Since the green histogram shows the case where $\sigma_{*,A} = \sigma_{*,B}$, we use it as a reference. We can see that when ET only observes for 1 year, the green and cyan histograms almost overlap and hence it is hard to distinguish $\sigma_{*,A} = 161\,\mathrm{km/s}$ from $171\,\mathrm{km/s}$. However, as we gradually increase the observation time to 10 years, the green and the cyan histograms separate, indicating that a KS test is able to distinguish 161 km/s and 171 km/s using the observed time delay distributions.

The lower panel of Figure 4.7 shows the ratio of KS($\sigma_{*,A} = 161$ km/s, $\sigma_{*,B} = 161$ km/s) over KS($\sigma_{*,A} = 171$ km/s, $\sigma_{*,B} = 161$ km/s). As mentioned before, this ratio should always be smaller than 1 because the δt distribution with $\sigma_{*,B} = 161$ km/s should be closer to theoretical model with $\sigma_{*,A} = 161$ than $\sigma_{*,A} = 171$ km/s. Nevertheless, due to the randomness of the sampling, and the limitation of the observation duration, the ratio may be bigger than 1 in some cases. This expectation is consistent with the lower panel of Figure 4.7 where we can see that the majority of the area of the histogram is smaller than 1. We can

consider the area smaller than 1 as the probability of having correct inference for the true underlying σ_*. As expected, Figure 4.7 shows that when we increase the observation time, the area of the histogram at values < 1 gets larger while the area > 1 gets smaller, indicating that increasing observing time enhances the probability of having correct inference for the underlying lens model.

We demonstrate how this procedure can be applied to other values of σ_* in Figure 4.8 which shows $\sigma_{*,A}$ versus the probability of having correct inference assuming three different observation times: 1 year, 5 years and 10 years. Similar to Figure 4.7, we use mock observational samples with $\sigma_{*,B} = 161$ km/s but now compare them with theoretical models in the range of $\sigma_{*,A} = 161 \pm 20$ km/s with an increment of 2 km/s, instead of just $\sigma_{*,A} = 171$ km/s. We repeat this procedure 30 times and compute the average KS statistics and the maximum and minimum values as the bounds of the error bars. As expected, the probability of a correct inference improves when $\sigma_{*,A}$ is further away from the $\sigma_{*,B}$. It is easier to distinguish models which are further apart. As shown in Figure 4.8, for the case of $\sigma_{*,B} = 161$ km/s, we can exclude $\sigma_* <$ 161-12 km/s and $\sigma_* >$ 161+16 km/s after 1 year of observation at 68 % confidence. Similarly, we are able to exclude $\sigma_* <$161-16 km/s and $\sigma_* >$ 161+18 km/s after 5 years of observation, and exclude $\sigma_* <$ 161-10 km/s and $\sigma_* >$ 161+14 km/s after 10 years of observation at 90 % confidence.

4.3.4 The effect of source population on the lensing rate

As described in Section 4.2.4, $\dot{N}_{\rm lensing}$ depends not only on the lens population, but also the source population. The distribution of sources is determined by the particular BBH formation channel. In this section, we focus on how the assumptions related to binary formation evolution affect $\dot{N}_{\rm lensing}$.

We calculate the rate of multiple images, $\dot{N}_{\rm lensing,2nd}$, for different values of the BBH merger rate parametrization described in Equation 4.10, assuming a wide range of α, β, and

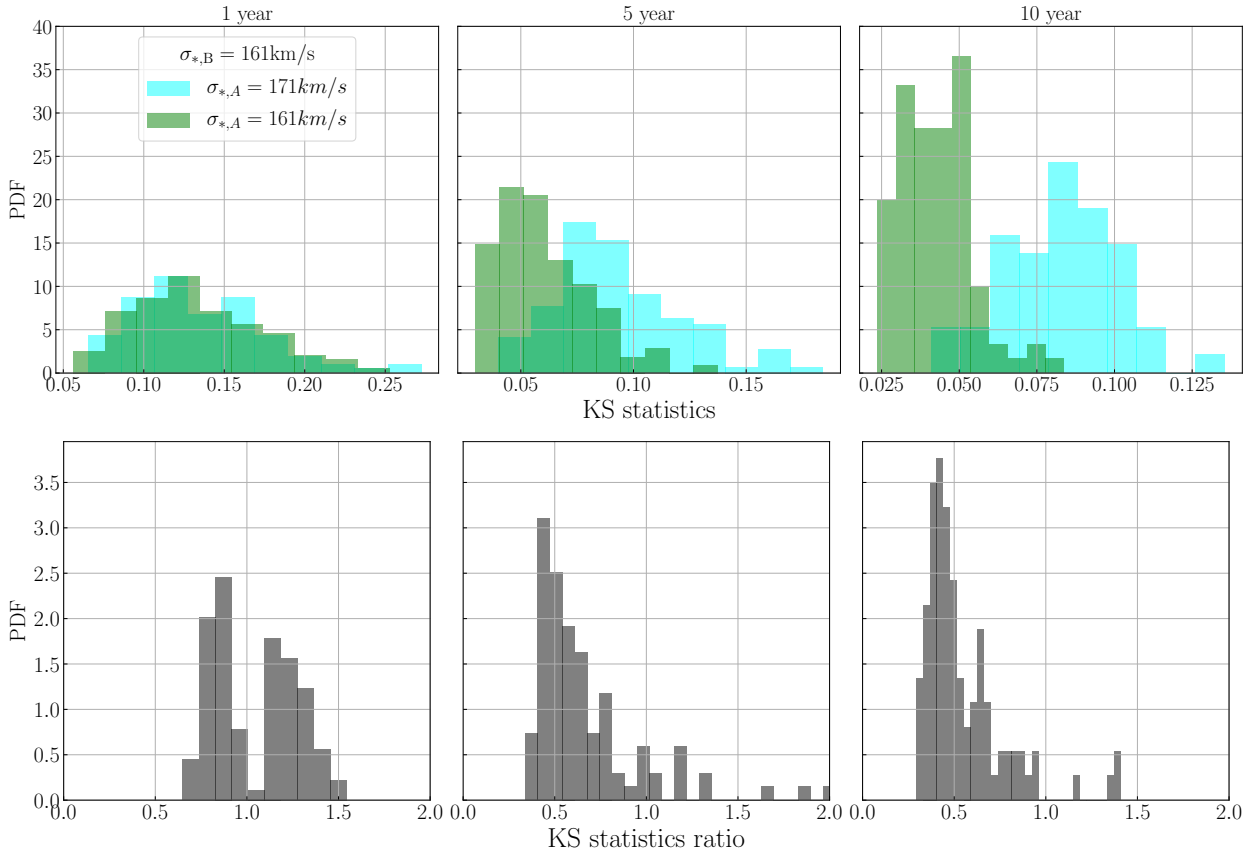

Figure 4.7: KS statistics for 1 year, 5 years, and 10 years. We use ET as the detector in this plot. Upper panels: The PDFs of KS values from comparing samples generated from a model with $\sigma_{*,\mathrm{B}} = 161$km/s and a model with $\sigma_{*,A} = 161$km/s (i.e., $\mathrm{KS}(\sigma_{*,\mathrm{A}} = 161\mathrm{km/s}, \sigma_{*,\mathrm{B}} = 161\mathrm{km/s})$, green histogram) and from comparing samples generated from a model with $\sigma_{*,\mathrm{A}} = 171$km/s and a model with $\sigma_{*,B} = 161$km/s (i.e., $\mathrm{KS}(\sigma_{*,\mathrm{A}} = 171\mathrm{km/s}, \sigma_{*,\mathrm{B}} = 161\mathrm{km/s})$, cyan histogram). The 2 distributions diverge away from each other as the detection duration time increases, meaning we can better distinguish between models with $\sigma_* = 171$km/s and with $\sigma_* = 161$km/s. Lower panels: The ratio of $\mathrm{KS}(\sigma_{*,\mathrm{A}} = 161\mathrm{km/s}, \sigma_{*,\mathrm{B}} = 161\mathrm{km/s})$ over $\mathrm{KS}(\sigma_{*,\mathrm{A}} = 171\mathrm{km/s}, \sigma_{*,\mathrm{B}} = 161\mathrm{km/s})$. The PDF area where the ratio is smaller than 1 is the probability of having correct inference which increases as we observe for a longer time.

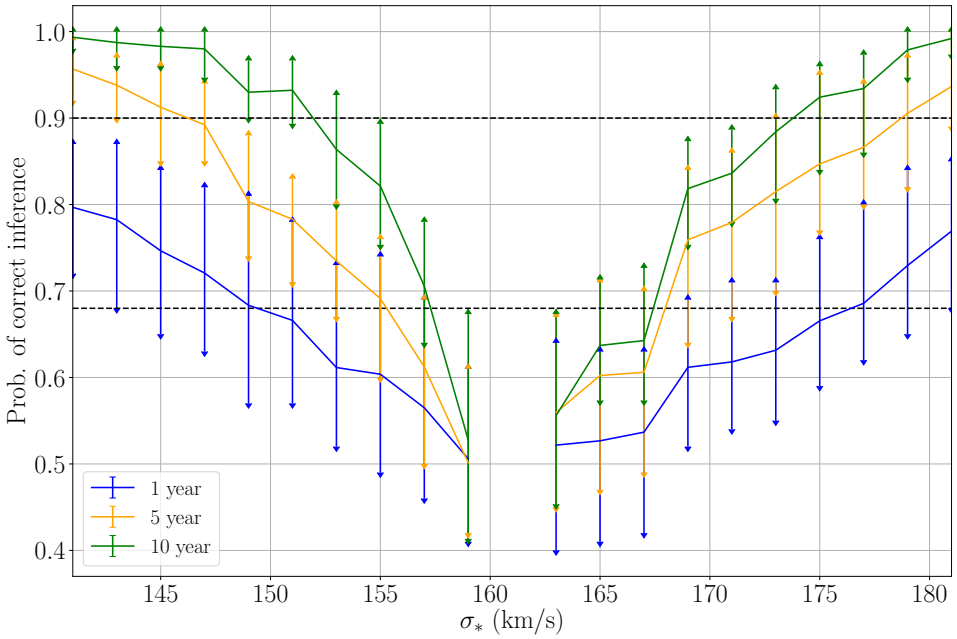

Figure 4.8: Probability of correct inference as a function of $\sigma_{*,A}$ for the case of ET. We set the characteristic lens galaxy velocity dispersion of the mock observation sample to $\sigma_{*,B} = 161$ km/s. Solid line with different colors represent the average probability of correct inference for observation time from 1 year, 5 years, and 10 years. The bars show the minimum and the maximum probability of correct inference at the given $\sigma_{*,A}$. The black dashed lines mark the place where the probability of having correct inference equals to 68 % and 90%. We assume ET is always online within the observation duration time.

z_p. The results for 2G and 3G detectors are presented in Figure 4.9 and 4.10, respectively. We can see the following features from the contour plot for aLIGO and A+: First, at constant z_p, $\dot{N}_{\rm lensing,2nd}$ increases as α increases. This is because when increasing α, the slope at low redshift gets steeper and the maximum value of $\dot{N}_{\rm BBH}$ becomes higher since the local merger rate is fixed. $\dot{N}_{\rm lensing,2nd}$ increases as there are more BBH sources for larger α. Second, at constant α, $\dot{N}_{\rm lensing,2nd}$ increases as z_p increases. This is because the original BBH merger rate increases when we increase z_p when fixing the local merger rate and the slope α. Third, it is difficult for aLIGO to probe the region where $\dot{N}_{\rm lensing,2nd} < 1{\rm yr}^{-1}$ because it requires a long observation time to achieve a precise constraint on the lensing event rate. Finally, when $z_p > 5$, $\dot{N}_{\rm lensing,2nd}$ stays roughly constant since aLIGO and A+ are mostly sensitive to BBHs at low redshift, thus any variations of z_p at high redshift $z \gtrsim 6$ has minimal impact on the observed $\dot{N}_{\rm lensing,2nd}$ for aLIGO. For ET and CE, as shown in Figure 4.10, their detection ability is significantly deeper and the expected $\dot{N}_{\rm lensing,2nd}$ is higher than for aLIGO and A+. Most of the region has $\dot{N}_{\rm lensing,2nd} > 1{\rm yr}^{-1}$, and thus 3G detectors are sensitive to a wider parameter space than 2G detectors.

Similarly, we can also draw contour plots for $\dot{N}_{\rm lensing,2nd}$ as a function of z_p and β, as shown in the right column of Figures 4.9 and 4.10. We can see that at low z_p, $\dot{N}_{\rm lensing,2nd}$ decreases with increasing β and then stays constant. This is because when β becomes large, the slope at higher redshift gets steeper but the general shape of the $\dot{N}_{\rm BBH}$ does not change significantly, hence $\dot{N}_{\rm lensing,2nd}$ stays relatively constant. The contours for $\dot{N}_{\rm lensing,2nd}$ become sparse when z_p is high, due to similar reasons to those mentioned above regarding the sensitive cosmological volumes for different detectors. However, since we are considering BBHs formed following star formation, z_p is unlikely to be greater than $z \sim 6$, so we only show results for cosmological distances within this.

These results show the potential for constraining the BBH source population with GW strong lensing observations. Even the non-detection of strong lensing, and accompanying

upper limits on the lensing event rate (e.g., $\dot{N}_{\rm lensing,2nd} < 1{\rm yr}^{-1}$) provide constraints on parameters of the phenomenological model (Equation 4.10) as shown in the contour plots in Figures 4.9 and 4.10. We mark the contour where $\dot{N}_{\rm lensing,2nd} = 1\,{\rm yr}^{-1}$. Alternatively, when fixing the formation scenario, strong lensing observations (or lack thereof) can be used to constrain the SFR and delay-time distribution, as we show in Appendix 4.5. As mentioned before, the lensing event rate in the region where $\dot{N}_{\rm lensing,2nd} < 1{\rm yr}^{-1}$ is difficult to constrain unless the observational duration is long. Therefore, 3G detectors provide better constraints on the source population than 2G detectors, not only because they are sensitive to higher redshift, but also because they have higher lensing event rates and the regions where $\dot{N}_{\rm lensing,2nd} > 1\,{\rm yr}^{-1}$ are wider. A realistic analysis of actual data would require a Bayesian population study so that all possible variables are varied at the same time. These analyses of individual events could be complemented with constraints from the stochastic background [Buscicchio et al., 2020, Mukherjee et al., 2021].

4.4 Optical depth for different lens models

In this appendix, we compare the optical depth τ derived using a Singular Isothermal Ellipsoid (SIE) model as in the main text (τ) with the Singular Isothermal Sphere (SIS) model ($\tau_{\rm SIS}$). The cross section of the SIS lens model is simply given by the Einstein radius θ_E of the lensing system in Equation 4.5. Apart from the geometrical configuration of the source-lens system, the Einstein radius is fully determined by the galaxy velocity dispersion σ.

Similarly as in Section 4.2.1, the differential optical depth is given by:

$$\begin{aligned}\frac{d\tau_{\rm SIS}}{dz_{\rm L}} &= \int_{\sigma_{\rm min}}^{\sigma_{\rm max}} \frac{dV_c}{\delta\Omega dz_{\rm L}} n(z_{\rm L},\sigma)\pi\theta_E^2(z_s,z_L,\sigma)\; d\sigma \\ &= \int_{\sigma_{\rm min}}^{\sigma_{\rm max}} 16\pi^3 \frac{c(1+z_{\rm L})^2}{H(z_{\rm L})}\left(\frac{D_{\rm L}D_{\rm LS}}{D_{\rm S}}\right)^2\left(\frac{\sigma}{c}\right)^4\phi(\sigma|z_L)d\sigma\end{aligned} \tag{4.18}$$

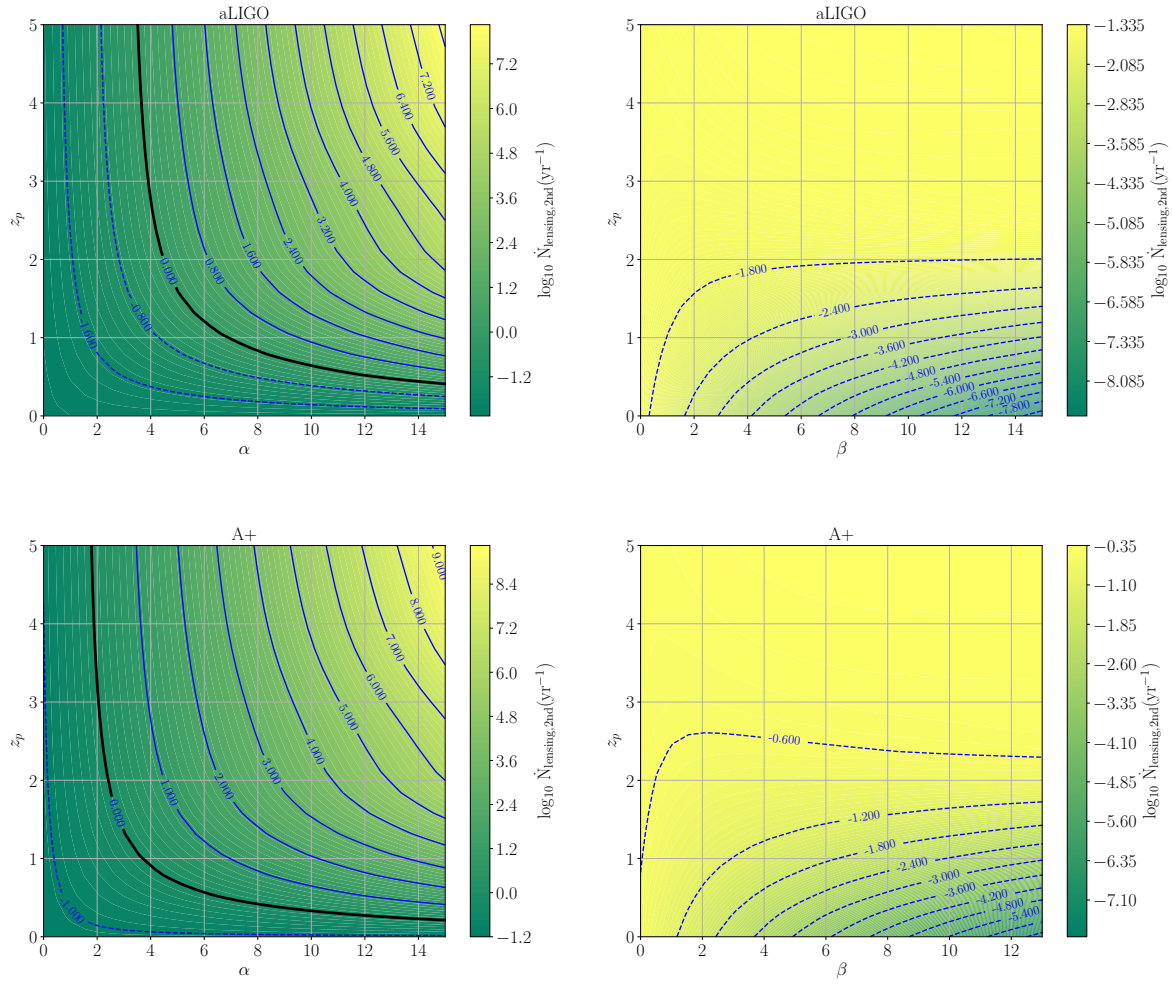

Figure 4.9: Lensing event rate $\dot{N}_{\rm lensing,2nd}$ distributions (number of the lensing pairs per year) for 2G detectors aLIGO and A+ still assuming $\sigma_* = 161$km/s. Contours are in $\log_{10}$ scale. Left column: $\dot{N}_{\rm lensing,2nd}$ contour plot in $z_p - \alpha$ parameter space. We fix $\beta = 1$. The black solid line represents the parameter regime that will likely have 1 event per year. Right column: $\dot{N}_{\rm lensing}$ contour plot in $z_p - \beta$ parameter space. We fix $\alpha = 1$ which is roughly at the peak of the constraint in O2 (See Figure 15 in Abbott et al. [2020a].)

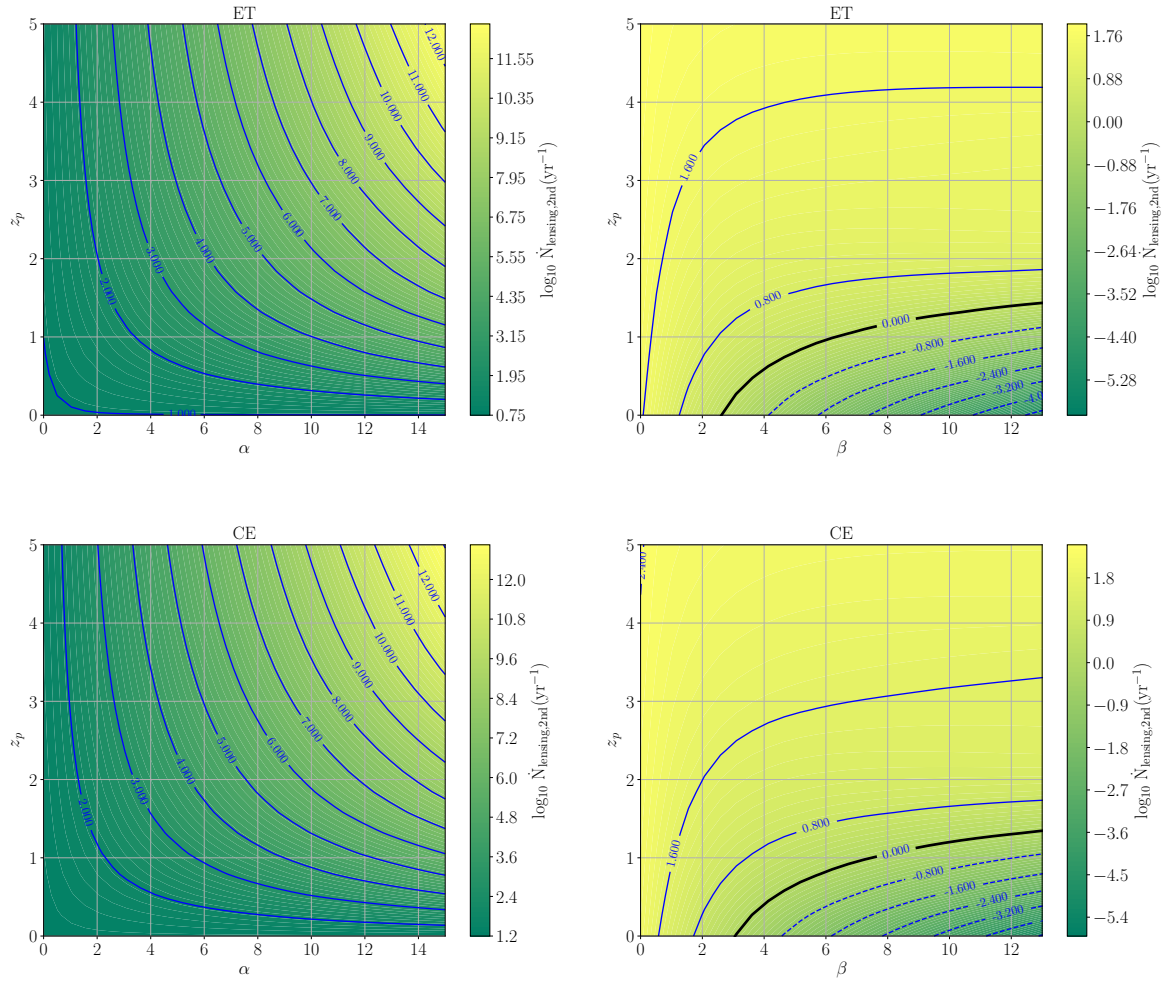

Figure 4.10: Lensing event rate $\dot{N}_{\rm lensing,2nd}$ (number of the lensing pairs per year) distributions for 3G detectors ET and CE assuming $\sigma_* = 161$km/s. Contours are in $\log_{10}$ scale. Left column: $\dot{N}_{\rm lensing,2nd}$ contour plot in $z_p - \alpha$ parameter space. We fix $\beta = 1$. Right column: $\dot{N}_{\rm lensing,2nd}$ contour plot in $z_p - \beta$ parameter space. We fix $\alpha = 1$ which is roughly at the peak of the constraint in O2 (See Figure 15 in Abbott et al. [2020a].)

where $\sigma_{\rm min}$ and $\sigma_{\rm max}$ are the lower and upper bound of σ. We substitute the differential comoving volume per solid angle in the second line. When setting $\sigma_{\rm min} = 0$ and $\sigma_{\rm max} = \infty$ and fixing the Schecter function for the number density of the lenses $\phi(\sigma|z_L)$, the expression of $\tau_{\rm SIS}$ can be integrated analytically [Haris et al., 2018]:

$$\tau_{\rm SIS} = 16\pi^3 (\frac{\sigma_*}{c})^4 \frac{\Gamma(\frac{4+\alpha}{\beta})}{\Gamma(\alpha/\beta)} \frac{n D_c(z_s)^3}{30} \,. \tag{4.19}$$

We can generalize the above expression to arbitrary integration bounds $\sigma_{\rm min}$ and $\sigma_{\rm max}$. Again, this can be integrated analytically. We obtain:

$$\tau_{\rm SIS}(z_S) = 16\pi^3 (\frac{{\sigma_*}^4}{c}) \frac{n D_c(z_s)^3}{30} \frac{\Gamma(\frac{\alpha+4}{\beta}, \frac{\sigma_{\rm max}}{\sigma_*}) - \Gamma(\frac{\alpha+4}{\beta}, \frac{\sigma_{\rm min}}{\sigma_*})}{\Gamma(\frac{\alpha}{\beta})} \,. \tag{4.20}$$

When comparing this calculation with the one in the main text, we find that the ratio of optical depths is $\tau/\tau_{\rm SIS} \approx 0.96$ and almost stays constant throughout the redshift range $z = 1 \sim 100$. This can be seen in Figure 4.11 where we plot both optical depths for different values of σ_*. The product $\tau_{\rm SIS} \times 0.96$ gives a good approximation to the SIE optical depth τ with a difference of only $\sim 0.5\%$, when $\sigma_{\rm min} = 0$, $\sigma_{\rm max} = \infty$. The factor of 0.96, however, does not apply to other scenarios.

The optical depth of the SIE model is subject to the choice of the multiple-image cross section. Across this work we fixed it to be determined by the "cut region" in Kormann et al. [1994]. This region determines the area in which at least two images are formed and it typically encloses the "caustic region" where four images are formed. Nonetheless, as displayed in Figure 2 of Kormann et al. [1994], when the lens axis ratio q_g is small, for example $q_g = 0.2$, the caustic region sticks out the cut which increases the overall cross section by a bit. Given the fact that most lenses have larger axis ratios, we believe this effect is negligible.

In addition, we also explore the impact of integration limits on the optical depth for the

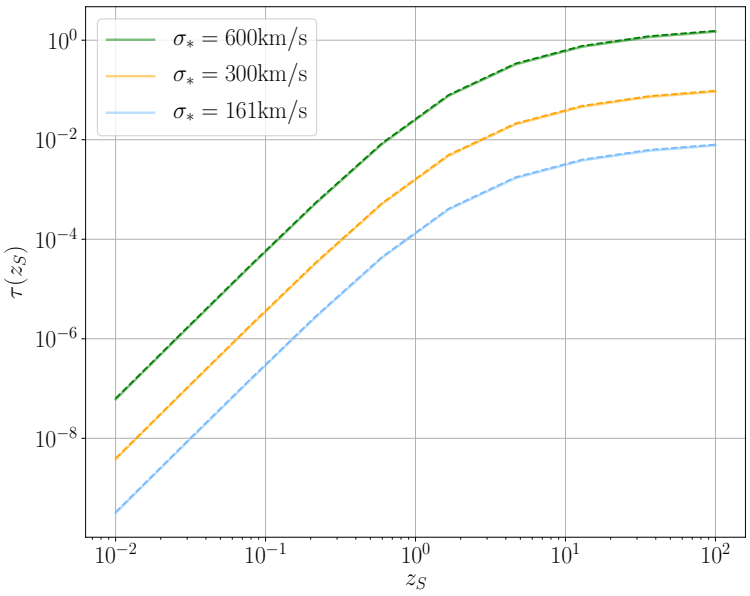

Figure 4.11: The optical depth as a function of source redshift $z_{\rm S}$. Solid and dashed lines represent τ assuming SIE model and SIS model respectively. Different colors represent different σ_*.

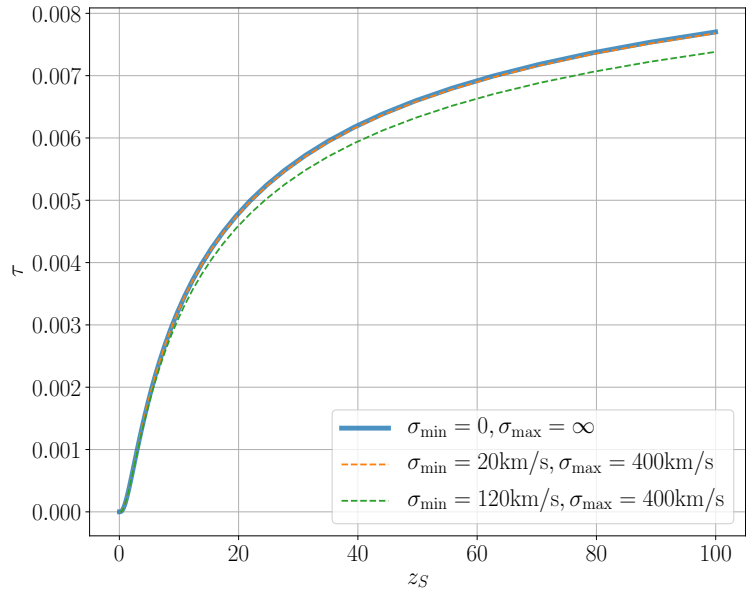

Figure 4.12: SIE optical depth assuming different upper and lower bounds for the velocity dispersion σ. The sky-blue solid line is the one we use in the main text of the chapter. We fix $\sigma_* = 161$ km/s in this plot.

case of SIE lens. Figure 4.12 shows the comparison using different $\sigma_{\rm min}$ and $\sigma_{\rm max}$. In the main text, we set $\sigma_{\rm min} = 0$ km/s and $\sigma_{\rm max} = \infty$ (in practice we set it to a large number, 10^5km s^{-1}, around which the number density of the galaxies is approximately equals to 0), which is shown in the sky-blue solid line. In reality, the upper and lower velocity dispersion might be different [Choi et al., 2007, McConnell and Ma, 2013], which would have an effect on $\tau(z)$. We tried different choices and, as shown in Figure 4.12 with dashed lines, the difference is not very significant when changing the upper and the lower bounds.

4.5 BBH merger rate history

In this appendix we provide further details about our choices for the merger rate history of BBHs. We parametrize the merger rate in the detector frame as:

$$\frac{d\dot{N}(z)}{dz} \equiv \mathcal{R}_0 e(z) \frac{dV(z)}{dz}\,, \tag{4.21}$$

where $\mathcal{R}(z=0) \equiv \mathcal{R}_0 = 64.9^{+75.5}_{-33.6} Gpc^{-3} yr^{-1}$ is the local merger rate density [Abbott et al., 2019], and $e(z)$ encapsulates all the redshift information [Zhu et al., 2011]. The definition of $e(z)$ is then:

$$e(z) = \frac{\mathcal{R}(z)}{\mathcal{R}_0(1+z)}\,, \tag{4.22}$$

which describes the evolution of the BBH merger relative to the local value. The factor $(1+z)$ converts the source-frame merger rate to the observer-frame merger rate. The numerator $\mathcal{R}(z)$ is given by:

$$\mathcal{R}(z) = \int_{\Delta t_{min}}^{t_H(z)} \dot{\rho}_*(z_f)\Phi(z_f,\xi)P(\Delta t)d\Delta t\,, \tag{4.23}$$

where z_f is the redshift at the binary formation. In this expression $\dot{\rho}_*(z_f)$ is the star formation rate, $\Phi(z_f,\xi)$ the metallicity cut and $P(\Delta t)$ the delay time distribution. The

delay time Δt is the look back time between binary formation and final merger:

$$\Delta t = \int_z^{z_f} \frac{dz'}{(1+z')H(z')}\,, \tag{4.24}$$

where $H(z)$ is the Hubble rate. We take $P(\Delta t) \propto \frac{1}{\Delta t}$ as the probability distribution of Δt. This distribution is integrated from a minimum delay time $\Delta t_{\rm min}$ to a maximum one which is equal the age of the universe at a given redshift $t_H(z)$.

The SFR density $\dot{\rho_*}$ determines the number of stars that form per unit time and volume. Its unit is $\mathrm{M_\odot Mpc^{-3} yr^{-1}}$. We follow the parametrization of Madau and Dickinson [2014] (MD14):

$$\dot{\rho_*}(z) = 0.015 \frac{(1+z)^{2.7}}{1+[(1+z)/2.9]^{5.6}} M_\odot Mpc^{-3} yr^{-1}\,. \tag{4.25}$$

Note that we do not convert $\dot{\rho}_*(z_f)$ from the source frame to the detector frame $\dot{\rho}_*(z_f)/(1+z_f)$ when integrating Equation 4.23 [Vitale et al., 2019, Callister et al., 2020]. The binary evolves in its own local frame with its own clock and thus does not have time dilation. However, we do need to convert $\mathcal{R}(z)$ from the source frame to the detector frame: $e(z) = \mathcal{R}(z) \times 1/(1+z)$ as in Equation 4.22.

Since BBH formation favors low metallicity, we include a metallicity dependence factor $\Phi(z_f, \xi)$ which is the fraction of the star formation rate density with metallicity less than ξ, where we set $\xi = Z/Z_\odot = 0.3$ [Langer and Norman, 2006]. The final SFR density is thus $\Phi(z_f, \xi = 0.3)\dot{\rho_*}(z)$.

We assume three kinds of SFR models and test how these SFR parameters affect the lensing event rate: (1) MD14 SFR with minimal delay time $\Delta t_{\rm min} = 50$ Myr (the one used in the main text); (2) MD14 SFR with $\Delta t_{\rm min} = 1$ Gyr; (3) a constant SFR model $\dot{\rho_*} = 0.004 M_\odot Mpc^{-3} \mathrm{yr}^{-1}$ with $\Delta t_{\rm min} = 50$ Myr. The $\Delta t_{\rm min}$ is set based on the result in population synthesis studies [Belczynski et al., 2002, Postnov and Yungelson, 2006, Dominik et al., 2013], and the maximal delay time to $t_H(z)$ introduced by the finite age of the universe.

constant SFR, $\Delta t_{\rm min} = 50$ Myr	$\dot{N}_{\rm lensing,1st}$	$\dot{N}_{\rm lensing,2nd}$	$\dot{N}_{\rm BBH}$
aLIGO	0.09	0.02	3.4×10^2
A+	0.58	0.13	1.4×10^3
ET	32	14	2.6×10^4
CE	42	31	3.5×10^4
MD 14 SFR, $\Delta t_{\rm min} = 1$ Gyr	$\dot{N}_{\rm lensing,1st}$	$\dot{N}_{\rm lensing,2nd}$	$\dot{N}_{\rm BBH}$
aLIGO	0.19	0.04	5.4×10^2
A+	1.02	0.3	2.7×10^3
ET	12	8	3.7×10^4
CE	14	13	4.1×10^4

Table 4.3: Lensing event rate ($\dot{N}_{\rm lensing}$, yr^{-1}) assuming $\sigma_* = 161$ km/s for different SFR scenarios. We assume an SIE lens model. The first table assumes constant SFR $\dot{\rho_*} = 0.004 M_\odot Mpc^{-3} yr^{-1}$ and $\Delta t_{\rm min} = 50$ Myr; the second table assumes MD14 [Madau and Dickinson, 2014] and $\Delta t_{\rm min} = 1$ Gyr. Similarly, the three columns correspond to $\dot{N}_{\rm lensing,\ 1st}$ and $\dot{N}_{\rm lensing,\ 2nd}$ derived from using $P(\mu)_{\rm 1st}$, $P(\mu)_{\rm 2nd}$ in Equation 4.16, and the expected observed BBH merger event per year $\dot{N}_{\rm BBH}$.

The comparison of the observed BBH merger rate $d\dot{N}_{\rm BBH}/dz$ assuming the above 3 SFR scenarios is shown in Figure 4.13, where we use ET as an example for the sensitivity. We can see that when $\Delta t_{\rm min}$ is small or the star formation is more uniform in the cosmic time, the BBH merger events are more extended to higher redshift.

Next we use these different prescriptions for the BBH merger rate to compute the expected rate of lensing. As in the main text we calculate the rate of detecting one strongly lensed image $\dot{N}_{\rm lensing,1st}$ and two multiply-lensed images $\dot{N}_{\rm lensing,2nd}$, comparing it with the overall (unlensed) BBH rate $\dot{N}_{\rm BBH}$. We summarize our lensing event rate results for the other two SFR scenarios in Table 4.3.

4.6 Strong lensing event rate from simulations

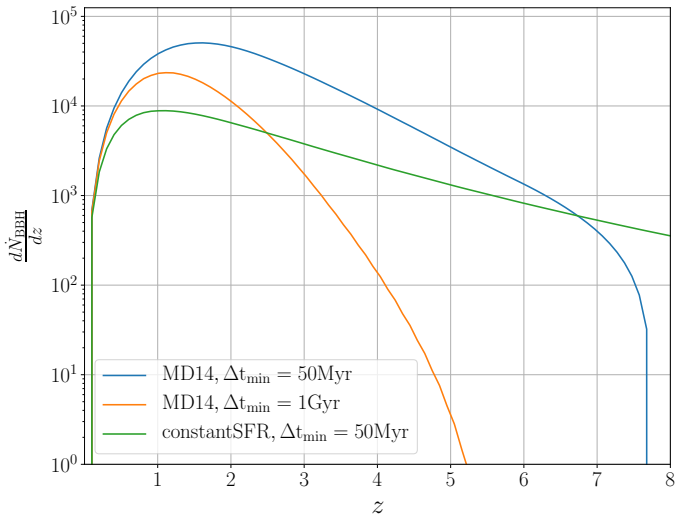

Figure 4.13: Expected BBH merger rate ($d\dot{N}_{\rm BBH}/dz$) as a function of redshift observed by ET under different assumptions of the star formation rate: SFR model in [Madau and Dickinson, 2014] with minimal binary merger delay time $\Delta t_{\rm min} = 50$ Myr (blue line), $\Delta t_{\rm min} = 1$ Gyr (orange line), and constant SFR $\dot{\rho_*} = 0.004 M_\odot Mpc^{-3}{\rm yr}^{-1}$ (green line).

	Primary image ($\dot{N}_{\rm lensing,1st}$)	$\dot{N}_{\rm lensing,2nd}$ single random number	$\dot{N}_{\rm lensing,2nd}$ 2 random numbers
aLIGO	0.36 ± 0.61	0.04 ± 0.19	0.03 ± 0.17
A+	2.87 ± 1.62	0.67 ± 0.79	0.22 ± 0.46
ET	94 ± 10	50 ± 6	45 ± 7
CE	111 ± 11	91 ± 10.0	89 ± 10

Table 4.4: We present the lensing event rate of the primary image ($\dot{N}_{\rm lensing,1st}$), and the lensing event rate with at least 2 images detected($\dot{N}_{\rm lensing,2nd}$) derived from taking the average and the standard deviation of 100 1-year mock observation samples. The first column is number of the events whose primary images are detected. The second and the third column show the number of the lensing events with at least 2 images detected but with different criterion. The second column compare one random number with the $P(w)$ for both images while the third column compare one random number for each image. These results are consistent with the analytical calculation presented in Table 4.1.

We present an alternative approach for calculating $\dot{N}_{\rm lensing,1st}$ and $\dot{N}_{\rm lensing,2nd}$. Instead of solving the integral (Equation 4.16), we now obtain the lensing rate directly from the lensing simulations. Basically we generate 100 mock observation samples as described in Section 4.2.3 and present the average lensing event rate and the standard deviation of these 100 samples in Table 4.4. To compute $\dot{N}_{\rm lensing,1st}$, we draw 1 random number and compare it with $P(w)$ of the primary image. If the random number is smaller than $P(w)$, we consider the image as detected. We use 2 ways to compute $\dot{N}_{\rm lensing,2nd}$: (1) We generate only 1 random number for each source, and compare it with the $P(w)$ of both images. If the random number is smaller than both $P(w)$, we consider the lensing pair is detected as shown in the second column of Table 4.4; (2) We generate 1 random number for each image and do the comparison with their own $P(w)$ as shown in the third column of Table 4.4. Only if both random numbers are smaller than their own $P(w)$, we consider the lensing pair is detected.

By comparing the result with Table 4.1 in Section 4.3.1, we can see that lensing event rate derived from the integration in Equation 4.16 can actually give a very good estimation. The estimation of $\dot{N}_{\rm lensing,1st}$ from the integration in Table 4.1 is very close to the average value from the simulation as shown in the first column of Table 4.4. While the estimation of $\dot{N}_{\rm lensing,2nd}$ from the integration is a bit higher than the $\dot{N}_{\rm lensing,2nd}$ in the third column of Table 4.4 but is consistent with the second column. This is because when doing the integration, we are using the magnification distribution of the secondary image $P(\mu)_{\rm 2nd}$ and thus we only take into account the $P(w)$ of the secondary image. The integral essentially gives the number of the lensing events whose secondary images are detected. Yet in some cases, due to the change in the orientation angle, we might miss the primary image but only detect the secondary one which is less loud. Therefore we think the actual lensing event rate might be lower than the prediction from Equation 4.16. The second method, however, has taken into account these scenarios, and therefore we believe the third column is more realistic. Nevertheless, the second column still gives a reasonable prediction, is less

computationally expensive, and can show the dependence of lensing event rate on σ_*.

4.7 Magnification ratio distribution

In addition to the time delay distribution studied in the main text, the magnification ratio of the secondary over the primary image μ_2/μ_1 distribution is another potential observable property for GW lensing. According to Equation 4.13, the magnification could potentially probe the axis ratio of the lens galaxies. We show the intrinsic and the observed μ_2/μ_1 ratio for aLIGO and ET as a demonstration in Figure 4.14. Due to the sensitivity, aLIGO may miss some of the secondary image with small μ_2 and therefore the observed μ_2/μ_1 distribution peaks near 1. Yet for higher sensitivity like ET, we are able to observe the full distribution. A combined analysis of both time delay distribution and magnification distribution may allow us to simultaneously constrain σ_* and q_g.

We can compare these results with the SIS model in which case the magnifications of each of the two images are known analytically: $|\mu_\pm| = 1 \pm 1/\beta$, where β indicates the angular position of the source [Schneider et al., 1992]. On the left panel of Figure 4.15 we present the magnification distribution of each of the images. This plot can be compared to the results in the main text for the SIE model in Figure 4.3. Two main differences are noticeable. In the SIS model, the brightest image always has a magnification larger than 2 for angular positions within the Einstein radius. Secondly, the magnification distribution of the parity-odd image, which is always less bright, does not have any peak as in the SIE model. This is because in the SIE model the second brightest image behaves differently when there are 4 images. With this information in hand we plot the relative magnification distribution in the right panel of Figure 4.15. This can be compared to the upper left panel of Figure 4.14.

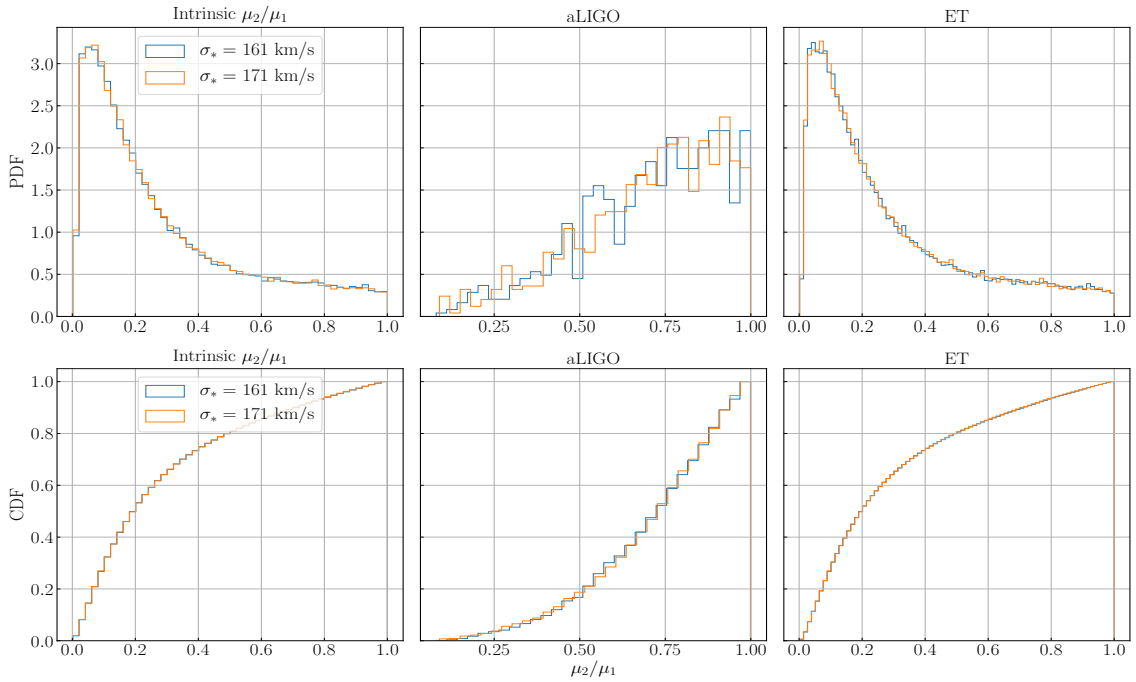

Figure 4.14: Intrinsic and the observed μ_2/μ_1 ratio. The left, middle, and right panel presents the intrinsic μ_2/μ_1, μ_2/μ_1 observed by aLIGO, and μ_2/μ_1 observed by ET. The upper panels are PDFs and lower panels are CDFs. We demonstrate 2 cases, $\sigma_* = 185$km/s and $\sigma_* = 200$km/s. The magnification ratio is not sensitive to the change in σ_*.

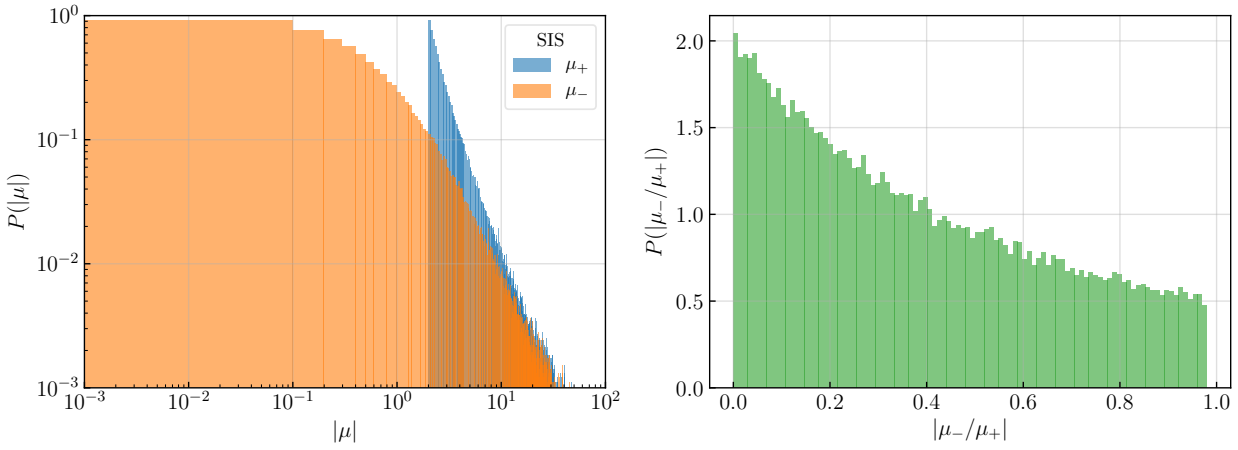

Figure 4.15: Magnification distribution for the SIS model. Left panel: we present the $P(|\mu|)$ of the individual images. Blue histogram represents the absolute magnification of the primary images, orange represents that of the secondary images. Right panel: we present the magnification ratio.

CHAPTER 5

SUMMARY AND CONCLUSIONS

In this thesis, we have explored the future of DM searches in both gamma-ray astronomy and GW astronomy. In particular, in Chapter 2, we discussed the gamma-ray observations of dwarf galaxies that can be used to place stringent constraints on annihilating DM. At present, such searches are statistically limited, and thus would significantly benefit from experiments capable of detecting more gamma-ray photons from such systems. We evaluated in this chapter the sensitivity of a future, large-acceptance, space-based gamma-ray telescope, focusing on the case of the proposed APT. As shown in Figs. 2.2 and 2.3, we project that an APT-like telescope would be very sensitive to annihilating DM particles, probing annihilation cross sections associated with thermal relics for masses up to $\sim 600\,\mathrm{GeV}$ (for the case of annihilation to $b\bar{b}$). In contrast, Fermi is currently only sensitive to such particles if they are lighter than $\sim 50\,\mathrm{GeV}$ [Albert et al., 2017, Di Mauro et al., 2022]. If the Galactic Center Gamma-Ray Excess is generated by annihilating DM, the corresponding signal from dwarf galaxies would be unambiguously detected by APT. In such a scenario, we find that APT would detect 7 dwarf galaxies with a significance of at least 2σ, and 3 dwarfs with a significance of 5σ or greater (in our median simulation). From such measurements, it could be established whether the gamma-ray fluxes from dwarf galaxies are proportional to the corresponding J-factors, providing us with a smoking gun signature of annihilating DM. In our simulations, we have considered 30 known dwarf galaxies and have used currently available determinations of their J-factors. It is anticipated, however, that many new dwarf galaxies will be discovered in the Rubin/LSST era, increasing the sensitivity of gamma-ray searches for DM annihilation products [Drlica-Wagner et al., 2019, Charles et al., 2016, He et al., 2015, Hargis et al., 2014]. Furthermore, spectroscopic measurements of stellar velocities in dwarf galaxies will continue to improve our ability to determine the J-factors of these systems, further improving the sensitivity of stacked dwarf analyses of gamma-ray

data. For these reasons, the actual sensitivity of APT to annihilating DM could plausibly exceed the projections that we have presented here.

Astrophysical backgrounds hinder our ability to study DM using gamma-ray telescopes. Understanding these backgrounds, both Galactic and extra-galactic, will aid in the detection of DM. In this Chapter 3, we have used the observed characteristics of the Milky Way's TeV halos to estimate the gamma-ray emission from the population of these objects in the Andromeda Galaxy, as well as the contribution from TeV halos to the IGRB. In the case of Andromeda, we project that the CTA will be sensitive to the diffuse, multi-TeV emission from the TeV halos in that system. We also conclude that a significant fraction of the IGRB is generated by TeV halos. In particular, we estimate that at the highest energies measured by Fermi, $E_\gamma \sim 0.1 - 1\,\text{TeV}$, on the order of 10% of the IGRB is generated by TeV halos. Taking this into account would reduce one's estimate for the neutrino flux from star-forming galaxies, potentially providing support for the hypothesis that misaligned AGN may be responsible for the diffuse neutrino flux reported by the IceCube Collaboration. If it is confirmed that millisecond pulsars also generate TeV halos, this would further increase the degree to which TeV halos are estimated to contribute to the IGRB.

This thesis work also explored the potential measurement of DM beyond the EM band. In Chapter 4, we explored the use of strong lensing of GW sources to study the distribution of galaxies and the population of BBHs in the universe. Unlike the case of strong lensing samples in the EM spectrum, GW astronomy offers the possibility of all-sky searches for lenses over a wide range of time delays, δt, with well-characterized selection functions. Furthermore, GW sources do not suffer from dust extinction, and are completely unaffected by any sources of obscuration along the line-of-sight (except for gravitational effects). We argue that future samples of multiply-imaged GW events will provide a powerful probe with which to study properties of both the lenses and the sources. The results of this analysis are summarized in Table 4.1 and Figure 4.5. We find that for typical lens parameters, the

expected number of lensing pairs per year is about 0.1 yr^{-1} for aLIGO and ~ 1 yr^{-1} for A+. We expect that hundreds of events will be detected with 3G GW detectors such as ET and CE. We demonstrate the dependence of the lensing event rate on the galaxy population, characterized by σ_*, in Figure 4.5, we demonstrate that both detection and non-detection of lensing events will provide valuable information on the lens and source population. In addition, by performing lensing simulations, we show that the distribution of time delays between multiply-imaged events provides helpful information to constrain the population of lenses, and is especially sensitive to the characteristic galaxy velocity dispersion, σ_*, defined in the Schechter function in Equation 4.3. We show that 3G detectors such as ET could constrain σ_* using the shape of the time delay δt distribution to a precision of 17% at the 68% confidence level after 1 year of observation, and ∼15–21% at $> 90\%$ confidence level after $\sim$ 5–10 years of observation.

Future lensing simulations could benefit from incorporating more detailed astrophysics, including a general halo mass function, baryonic effects, and galaxy types. For example, we could adopt a more realistic lens model, such as an NFW profile mentioned in Chapter 1.2.2 [Navarro et al., 1996] instead of a simple SIE model. We emphasize that the distributions of the lensing events presented above, such as the magnification distribution, will be able to constrain these properties of the lenses. When considering smaller scales, one can also take into account baryonic physics which will alter the sub-structure of DM halos. These effects, such as stellar or AGN feedback, may have an impact on the subhalo population, which would in turn modify the lensing optical depth and the distributions of lensing properties [Hoeft et al., 2004, Duffy et al., 2010, Chan et al., 2015, Nadler et al., 2021]. Moreover, in the current simulations we consider lenses with DM halos of mass $\sim 10^{11} M_\odot$ where hydrodynamical simulations predict the greatest probability for lensing [Robertson et al., 2020]. However, the detailed substructure of DM halos at smaller scales may as well affect the lensing optical depth, magnification distributions, and time delay distribution. We note that DM sub-

structure could also be a target for *LISA* [Takahashi and Nakamura, 2003]. Gamma-ray bursts and fast radio bursts also provide interesting source populations for lensing studies [Holz et al., 1999, Muñoz et al., 2016, Cordes et al., 2017], in a similar fashion to the GW sources discussed.

The advancement in gamma-ray astronomy along with GW astronomy will open a new door to the exploration of the inhomogeneous universe. As the sensitivity of gamma-ray telescopes and GW detectors improve, these instruments will offer important probes of the properties of DM. We very much look forward to seeing the future progress in understanding the true nature of DM.

REFERENCES

An absence of neutrinos associated with cosmic-ray acceleration in γ-ray bursts. *Nature*, 484(7394):351â354, Apr 2012. ISSN 1476-4687. doi:10.1038/nature11068. URL `http://dx.doi.org/10.1038/nature11068`.

et al. A. Acharyya. Sensitivity of the cherenkov telescope array to a dark matter signal from the galactic centre. *Journal of Cosmology and Astroparticle Physics*, 2021(01):057–057, jan 2021. doi:10.1088/1475-7516/2021/01/057. URL `https://doi.org/10.1088%2F1475-7516%2F2021%2F01%2F057`.

et al. A. De Angelis. The e-ASTROGAM mission. *Experimental Astronomy*, 44(1):25–82, jun 2017. doi:10.1007/s10686-017-9533-6. URL `https://doi.org/10.1007%2Fs10686-017-9533-6`.

J. Aalbers et al. First Dark Matter Search Results from the LUX-ZEPLIN (LZ) Experiment. 7 2022.

M. G. Aartsen et al. Evidence for High-Energy Extraterrestrial Neutrinos at the IceCube Detector. *Science*, 342:1242856, 2013. doi:10.1126/science.1242856.

M. G. Aartsen et al. Observation of High-Energy Astrophysical Neutrinos in Three Years of IceCube Data. *Phys. Rev. Lett.*, 113:101101, 2014. doi:10.1103/PhysRevLett.113.101101.

M. G. Aartsen et al. A combined maximum-likelihood analysis of the high-energy astrophysical neutrino flux measured with IceCube. *Astrophys. J.*, 809(1):98, 2015a. doi:10.1088/0004-637X/809/1/98.

M. G. Aartsen et al. Evidence for Astrophysical Muon Neutrinos from the Northern Sky with IceCube. *Phys. Rev. Lett.*, 115(8):081102, 2015b. doi:10.1103/PhysRevLett.115.081102.

M. G. Aartsen et al. Flavor Ratio of Astrophysical Neutrinos above 35 TeV in IceCube. *Phys. Rev. Lett.*, 114(17):171102, 2015c. doi:10.1103/PhysRevLett.114.171102.

Kevork N. Abazajian and Manoj Kaplinghat. Detection of a Gamma-Ray Source in the Galactic Center Consistent with Extended Emission from Dark Matter Annihilation and Concentrated Astrophysical Emission. *Phys. Rev. D*, 86:083511, 2012. doi:10.1103/PhysRevD.86.083511. [Erratum: Phys.Rev.D 87, 129902 (2013)].

B. P. Abbott et al. Prospects for Observing and Localizing Gravitational-Wave Transients with Advanced LIGO, Advanced Virgo and KAGRA. *Living Rev. Rel.*, 21(1):3, 2018. doi:10.1007/s41114-018-0012-9.

B. P. Abbott et al. Binary Black Hole Population Properties Inferred from the First and Second Observing Runs of Advanced LIGO and Advanced Virgo. , 882(2):L24, September 2019. doi:10.3847/2041-8213/ab3800.

R. Abbott et al. Advanced LIGO. *Classical and Quantum Gravity*, 32(7):074001, April 2015. doi:10.1088/0264-9381/32/7/074001.

R. Abbott et al. Population Properties of Compact Objects from the Second LIGO-Virgo Gravitational-Wave Transient Catalog. *arXiv e-prints*, art. arXiv:2010.14533, October 2020a.

R. Abbott et al. Population Properties of Compact Objects from the Second LIGO-Virgo Gravitational-Wave Transient Catalog. 10 2020b.

R. Abbott et al. Search for lensing signatures in the gravitational-wave observations from the first half of LIGO-Virgo's third observing run. 5 2021.

H. Abdalla et al. The population of TeV pulsar wind nebulae in the H.E.S.S. Galactic Plane Survey. *Astron. Astrophys.*, 612:A2, 2018a. doi:10.1051/0004-6361/201629377.

H. Abdalla et al. The H.E.S.S. Galactic plane survey. *Astron. Astrophys.*, 612:A1, 2018b. doi:10.1051/0004-6361/201732098.

A. A. Abdo, B. T. Allen, T. Aune, D. Berley, C. Chen, G. E. Christopher, T. DeYoung, B. L. Dingus, R. W. Ellsworth, M. M. Gonzalez, J. A. Goodman, E. Hays, C. M. Hoffman, P. H. Hüntemeyer, B. E. Kolterman, J. T. Linnemann, J. E. McEnery, T. Morgan, A. I. Mincer, P. Nemethy, J. Pretz, J. M. Ryan, P. M. Saz Parkinson, A. Shoup, G. Sinnis, A. J. Smith, V. Vasileiou, G. P. Walker, D. A. Williams, and G. B. Yodh. Milagro Observations of Multi-TeV Emission from Galactic Sources in the Fermi Bright Source List. *apjl*, 700 (2):L127–L131, August 2009. doi:10.1088/0004-637X/700/2/L127.

A. A. Abdo, M. Ackermann, M. Ajello, E. Antolini, L. Baldini, J. Ballet, G. Barbiellini, D. Bastieri, B. M. Baughman, K. Bechtol, and et al. Thefermi-lat high-latitude survey: Source count distributions and the origin of the extragalactic diffuse background. *The Astrophysical Journal*, 720(1):435â453, Aug 2010. ISSN 1538-4357. doi:10.1088/0004-637x/720/1/435. URL `http://dx.doi.org/10.1088/0004-637X/720/1/435`.

A. U. Abeysekara et al. Extended gamma-ray sources around pulsars constrain the origin of the positron flux at Earth. *Science*, 358(6365):911–914, 2017. doi:10.1126/science.aan4880.

A. U. Abeysekara et al. Multiple Galactic Sources with Emission Above 56 TeV Detected by HAWC. *Phys. Rev. Lett.*, 124(2):021102, 2020. doi:10.1103/PhysRevLett.124.021102.

B. S. Acharya et al. Introducing the CTA concept. *Astropart. Phys.*, 43:3–18, 2013. doi:10.1016/j.astropartphys.2013.01.007.

et al. Ackermann, M.. The Fermi Galactic Center GeV Excess and Implications for Dark Matter. , 840(1):43, May 2017. doi:10.3847/1538-4357/aa6cab.

M. Ackermann, M. Ajello, A. Albert, W. B. Atwood, L. Baldini, J. Ballet, G. Barbiellini, D. Bastieri, K. Bechtol, R. Bellazzini, and et al. The spectrum of isotropic diffuse gamma-ray emission between 100Â mev and 820Â gev. *The Astrophysical Journal*, 799(1):86, Jan

2015a. ISSN 1538-4357. doi:10.1088/0004-637x/799/1/86. URL http://dx.doi.org/10.1088/0004-637X/799/1/86.

M. Ackermann, M. Ajello, A. Albert, L. Baldini, J. Ballet, G. Barbiellini, D. Bastieri, R. Bellazzini, E. Bissaldi, E. D. Bloom, and et al. Observations of m31 and m33 with the fermi large area telescope: A galactic center excess in andromeda? *The Astrophysical Journal*, 836(2):208, Feb 2017. ISSN 1538-4357. doi:10.3847/1538-4357/aa5c3d. URL http://dx.doi.org/10.3847/1538-4357/aa5c3d.

M. Ackermann et al. Dark Matter Constraints from Observations of 25 Milky Way Satellite Galaxies with the Fermi Large Area Telescope. *Phys. Rev. D*, 89:042001, 2014. doi:10.1103/PhysRevD.89.042001.

M. Ackermann et al. The spectrum of isotropic diffuse gamma-ray emission between 100 MeV and 820 GeV. *Astrophys. J.*, 799:86, 2015b. doi:10.1088/0004-637X/799/1/86.

Elizabeth A. K. Adams and Joeri van Leeuwen. Radio surveys now both deep and wide. *Nature Astronomy*, 3:188–188, February 2019. doi:10.1038/s41550-019-0692-4.

N. Aghanim et al. Planck 2018 results. VI. Cosmological parameters. *Astron. Astrophys.*, 641:A6, 2020. doi:10.1051/0004-6361/201833910. [Erratum: Astron.Astrophys. 652, C4 (2021)].

F. A. Aharonian and A. M. Atoyan. Broad-band diffuse gamma-ray emission of the galactic disk. *Astron. Astrophys.*, 362:937, 2000.

F. A. Aharonian, A. G. Akhperjanian, M. Beilicke, K. Bernlöhr, H. Bojahr, O. Bolz, H. Börst, T. Coarasa, J. L. Contreras, J. Cortina, S. Denninghoff, V. Fonseca, M. Girma, N. Götting, G. Heinzelmann, G. Hermann, A. Heusler, W. Hofmann, D. Horns, I. Jung, R. Kankanyan, M. Kestel, J. Kettler, A. Kohnle, A. Konopelko, H. Kornmeyer, D. Kranich, H. Krawczynski, H. Lampeitl, M. Lopez, E. Lorenz, F. Lucarelli, O. Mang, H. Meyer, R. Mirzoyan, A. Moralejo, E. Ona, M. Panter, A. Plyasheshnikov, G. Pühlhofer, G. Rauterberg, R. Reyes, W. Rhode, J. Ripken, A. Röhring, G. P. Rowell, V. Sahakian, M. Samorski, M. Schilling, M. Siems, D. Sobzynska, W. Stamm, M. Tluczykont, H. J. Völk, C. A. Wiedner, and W. Wittek. Search for TeV gamma ray emission from the Andromeda galaxy. *aap*, 400:153–159, March 2003. doi:10.1051/0004-6361:20021895.

Markus Ahlers and Jordi Salvado. Cosmogenic gamma-rays and the composition of cosmic rays. *Phys. Rev. D*, 84:085019, 2011. doi:10.1103/PhysRevD.84.085019.

M. Ajello and et al. W. B. Atwood. Fermi large area telescope performance after 10 years of operation. *The Astrophysical Journal Supplement Series*, 256(1):12, sep 2021. doi:10.3847/1538-4365/ac0ceb. URL https://doi.org/10.3847%2F1538-4365%2Fac0ceb.

M. Ajello, M. S. Shaw, R. W. Romani, C. D. Dermer, L. Costamante, O. G. King, W. Max-Moerbeck, A. Readhead, A. Reimer, J. L. Richards, and et al. The luminosity function

offermi-detected flat-spectrum radio quasars. *The Astrophysical Journal*, 751(2):108, May 2012. ISSN 1538-4357. doi:10.1088/0004-637x/751/2/108. URL http://dx.doi.org/10.1088/0004-637X/751/2/108.

M. Ajello et al. Fermi-LAT Observations of High-Energy γ-Ray Emission Toward the Galactic Center. *Astrophys. J.*, 819(1):44, 2016. doi:10.3847/0004-637X/819/1/44.

M. Ajello et al. Fermi Large Area Telescope Performance after 10 Years of Operation. *Astrophys. J. Supp.*, 256(1):12, 2021. doi:10.3847/1538-4365/ac0ceb.

A. Albert, R. Alfaro, C. Alvarez, J. C. Arteaga-VelÃ¡zquez, K. P. Arunbabu, D. Avila Rojas, H. A. Ayala Solares, E. Belmont-Moreno, S. Y. BenZvi, C. Brisbois, and et al. Constraints on the emission of gamma-rays from m31 with hawc. *The Astrophysical Journal*, 893(1): 16, Apr 2020a. ISSN 1538-4357. doi:10.3847/1538-4357/ab7999. URL http://dx.doi.org/10.3847/1538-4357/ab7999.

A. Albert et al. Searching for Dark Matter Annihilation in Recently Discovered Milky Way Satellites with Fermi-LAT. *Astrophys. J.*, 834(2):110, 2017. doi:10.3847/1538-4357/834/2/110.

A. Albert et al. 3HWC: The Third HAWC Catalog of Very-High-Energy Gamma-ray Sources. *Astrophys. J.*, 905(1):76, 2020b. doi:10.3847/1538-4357/abc2d8.

A. Albert et al. Evidence that Ultra-high-energy Gamma Rays Are a Universal Feature near Powerful Pulsars. *Astrophys. J. Lett.*, 911(2):L27, 2021. doi:10.3847/2041-8213/abf4dc.

et al. Albert, A. Searching for Dark Matter Annihilation in Recently Discovered Milky Way Satellites with Fermi-Lat. , 834(2):110, January 2017. doi:10.3847/1538-4357/834/2/110.

Samer Alnussirat et al. The Advanced Particle-astrophysics Telescope: Simulation of the Instrument Performance for Gamma-Ray Detection. *PoS*, ICRC2021:590, 2021. doi:10.22323/1.395.0590.

Rafael Alves Batista and Andrey Saveliev. The gamma-ray window to intergalactic magnetism. *Universe*, 7(7), 2021. ISSN 2218-1997. doi:10.3390/universe7070223. URL https://www.mdpi.com/2218-1997/7/7/223.

E. Aprile et al. First Dark Matter Search with Nuclear Recoils from the XENONnT Experiment. 3 2023.

et al. A.U. Abeysekara. A search for dark matter in the galactic halo with HAWC. *Journal of Cosmology and Astroparticle Physics*, 2018(02):049–049, feb 2018. doi:10.1088/1475-7516/2018/02/049. URL https://doi.org/10.1088%2F1475-7516%2F2018%2F02%2F049.

Arash Bahramian, Craig O. Heinke, Gregory R. Sivakoff, and Jeanette C. Gladstone. Stellar Encounter Rate in Galactic Globular Clusters. *Astrophys. J.*, 766:136, 2013. doi:10.1088/0004-637X/766/2/136.

X. Bai, B. Y. Bi, X. J. Bi, Z. Cao, S. Z. Chen, Y. Chen, A. Chiavassa, X. H. Cui, Z. G. Dai, D. della Volpe, T. Di Girolamo, Giuseppe Di Sciascio, Y. Z. Fan, J. Giacalone, Y. Q. Guo, H. H. He, T. L. He, M. Heller, D. Huang, Y. F. Huang, H. Jia, L. T. Ksenofontov, D. Leahy, F. Li, Z. Li, E. W. Liang, P. Lipari, R. Y. Liu, Y. Liu, S. Liu, X. Ma, O. Martineau-Huynh, D. Martraire, T. Montaruli, D. Ruffolo, Y. V. Stenkin, H. Q. Su, T. Tam, Q. W. Tang, W. W. Tian, P. Vallania, S. Vernetto, C. Vigorito, J. . C. Wang, L. Z. Wang, X. Wang, X. Y. Wang, X. J. Wang, Z. X. Wang, D. M. Wei, J. J. Wei, D. Wu, H. R. Wu, X. F. Wu, D. H. Yan, A. Y. Yang, R. Z. Yang, Z. G. Yao, L. Q. Yin, Q. Yuan, B. Zhang, B. Zhang, L. Zhang, M. F. Zhang, S. S. Zhang, X. Zhang, Y. Zhao, X. X. Zhou, F. R. Zhu, and H. Zhu. The large high altitude air shower observatory (lhaaso) science white paper, 2019.

Keith Bechtol, A. Drlica-Wagner, Eduardo Balbinot, Adriano Pieres, J. Simon, B. Yanny, Risa Wechsler, J. Frieman, A. Walker, Pobi Williams, E. Rozo, E. Rykoff, Anna Queiroz, E. Luque, Aurélien Benoit-Lévy, Rebecca Bernstein, Douglas Tucker, I. Sevilla, and J. Zuntz. Eight new milky way companions discovered in first-year dark energy survey data. *The Astrophysical Journal*, 807, 03 2015. doi:10.1088/0004-637X/807/1/50.

Krzysztof Belczynski, Vassiliki Kalogera, and Tomasz Bulik. A Comprehensive Study of Binary Compact Objects as Gravitational Wave Sources: Evolutionary Channels, Rates, and Physical Properties. , 572(1):407–431, June 2002. doi:10.1086/340304.

C. L. Bennett, D. Larson, J. L. Weiland, N. Jarosik, G. Hinshaw, N. Odegard, K. M. Smith, R. S. Hill, B. Gold, M. Halpern, E. Komatsu, M. R. Nolta, L. Page, D. N. Spergel, E. Wollack, J. Dunkley, A. Kogut, M. Limon, S. S. Meyer, G. S. Tucker, and E. L. Wright. Nine-year Wilkinson Microwave Anisotropy Probe (WMAP) Observations: Final Maps and Results. , 208(2):20, October 2013. doi:10.1088/0067-0049/208/2/20.

V. Berezinsky and O. Kalashev. High energy electromagnetic cascades in extragalactic space: physics and features. *Phys. Rev. D*, 94(2):023007, 2016. doi:10.1103/PhysRevD.94.023007.

Lars Bergstrom, Torsten Bringmann, Ilias Cholis, Dan Hooper, and Christoph Weniger. New Limits on Dark Matter Annihilation from AMS Cosmic Ray Positron Data. *Phys. Rev. Lett.*, 111:171101, 2013. doi:10.1103/PhysRevLett.111.171101.

Gianfranco Bertone and Dan Hooper. A History of Dark Matter. *Rev. Mod. Phys.*, 90(4): 045002, 2018. doi:10.1103/RevModPhys.90.045002.

Gianfranco Bertone and Tim Tait, M. P. A new era in the search for dark matter. *Nature*, 562(7725):51–56, 2018. doi:10.1038/s41586-018-0542-z.

H. Bethe and W. Heitler. On the Stopping of Fast Particles and on the Creation of Positive Electrons. *Proceedings of the Royal Society of London Series A*, 146(856):83–112, August 1934. doi:10.1098/rspa.1934.0140.

Pooja Bhattacharjee, Pratik Majumdar, Sayan Biswas, and Partha S. Joarder. Analysis of Fermi-LAT data from Tucana-II: Possible constraints on the Dark Matter models with an intriguing hint of a signal. *JCAP*, 08:028, 2019. doi:10.1088/1475-7516/2019/08/028.

Marek Biesiada, Xuheng Ding, Aleksandra Piórkowska, and Zong-Hong Zhu. Strong gravitational lensing of gravitational waves from double compact binaries—perspectives for the Einstein Telescope. , 2014(10):080, October 2014. doi:10.1088/1475-7516/2014/10/080.

Carlos Blanco. Î³-cascade: a simple program to compute cosmological gamma-ray propagation. *Journal of Cosmology and Astroparticle Physics*, 2019(01):013â013, Jan 2019. ISSN 1475-7516. doi:10.1088/1475-7516/2019/01/013. URL `http://dx.doi.org/10.1088/1475-7516/2019/01/013`.

Carlos Blanco and Dan Hooper. High-Energy Gamma Rays and Neutrinos from Nearby Radio Galaxies. *JCAP*, 12:017, 2017. doi:10.1088/1475-7516/2017/12/017.

Carlos Blanco and Tim Linden. Gamma-rays from star forming activity appear to outshine misaligned active galactic nuclei, 2021.

Roger Blandford and Ramesh Narayan. Fermat's Principle, Caustics, and the Classification of Gravitational Lens Images. , 310:568, November 1986. doi:10.1086/164709.

Roger Blandford and Ramesh Narayan. Fermat's principle, caustics, and the classification of gravitational lens images. *Astrophys. J.*, 310:568–582, 1986. doi:10.1086/164709.

V. Bonnivard, C. Combet, D. Maurin, and M. G. Walker. Spherical Jeans analysis for dark matter indirect detection in dwarf spheroidal galaxies - impact of physical parameters and triaxiality. , 446(3):3002–3021, January 2015. doi:10.1093/mnras/stu2296.

Jo Bovy and Scott Tremaine. On the Local Dark Matter Density. , 756(1):89, September 2012. doi:10.1088/0004-637X/756/1/89.

James Buckley and APT Team. The Advanced Particle-astrophysics Telescope (APT). *Bulletin of the AAS*, 54(3), apr 1 2022. https://baas.aas.org/pub/2022n3i404p04.

James H. Buckley et al. The Advanced Particle-astrophysics Telescope (APT) Project Status. *PoS*, ICRC2021:655, 2021. doi:10.22323/1.395.0655.

Riccardo Buscicchio, Christopher J. Moore, Geraint Pratten, Patricia Schmidt, Matteo Bianconi, and Alberto Vecchio. Constraining the lensing of binary black holes from their stochastic background. *Phys. Rev. Lett.*, 125(14):141102, 2020. doi:10.1103/PhysRevLett.125.141102.

Tom Callister, Maya Fishbach, Daniel E. Holz, and Will M. Farr. Shouts and Murmurs: Combining Individual Gravitational-wave Sources with the Stochastic Background to Measure the History of Binary Black Hole Mergers. , 896(2):L32, June 2020. doi:10.3847/2041-8213/ab9743.

Francesca Calore, Ilias Cholis, and Christoph Weniger. Background Model Systematics for the Fermi GeV Excess. *JCAP*, 03:038, 2015. doi:10.1088/1475-7516/2015/03/038.

Francesca Calore, Marco Cirelli, Laurent Derome, Yoann Genolini, David Maurin, Pierre Salati, and Pasquale Dario Serpico. AMS-02 antiprotons and dark matter: Trimmed hints and robust bounds. *SciPost Phys.*, 12(5):163, 2022. doi:10.21468/SciPostPhys.12.5.163.

Daniela Calzetti. Reddening and Star Formation in Starburst Galaxies. , 113:162–184, January 1997. doi:10.1086/118242.

Daniela Calzetti, Lee Armus, Ralph C. Bohlin, Anne L. Kinney, Jan Koornneef, and Thaisa Storchi-Bergmann. The Dust Content and Opacity of Actively Star-forming Galaxies. , 533(2):682–695, April 2000. doi:10.1086/308692.

Shuo Cao, Yu Pan, Marek Biesiada, Wlodzimierz Godlowski, and Zong-Hong Zhu. Constraints on cosmological models from strong gravitational lensing systems. , 2012(3):016, March 2012. doi:10.1088/1475-7516/2012/03/016.

Zhen Cao, D. della Volpe, and et al. Siming Liu. The large high altitude air shower observatory (lhaaso) science book (2021 edition), 2022.

Kyu-Hyun Chae. The Cosmic Lens All-Sky Survey: statistical strong lensing, cosmological parameters, and global properties of galaxy populations. , 346(3):746–772, December 2003. doi:10.1111/j.1365-2966.2003.07092.x.

Kyu-Hyun Chae. Constraints on the Velocity Dispersion Function of Early-Type Galaxies from the Statistics of Strong Gravitational Lensing. , 630(2):764–770, September 2005. doi:10.1086/432435.

Kyu-Hyun Chae and Shude Mao. Limits on the Evolution of Galaxies from the Statistics of Gravitational Lenses. , 599(2):L61–L64, December 2003. doi:10.1086/381247.

T. K. Chan, D. Kereš, J. Oñorbe, P. F. Hopkins, A. L. Muratov, C. A. Faucher-Giguère, and E. Quataert. The impact of baryonic physics on the structure of dark matter haloes: the view from the FIRE cosmological simulations. , 454(3):2981–3001, December 2015. doi:10.1093/mnras/stv2165.

E. Charles et al. Sensitivity Projections for Dark Matter Searches with the Fermi Large Area Telescope. *Phys. Rept.*, 636:1–46, 2016. doi:10.1016/j.physrep.2016.05.001.

Yun-Young Choi, Changbom Park, and Michael S. Vogeley. Internal and Collective Properties of Galaxies in the Sloan Digital Sky Survey. , 658(2):884–897, April 2007. doi:10.1086/511060.

Ilias Cholis, Yi-Ming Zhong, Samuel D. McDermott, and Joseph P. Surdutovich. The Return of the Templates: Revisiting the Galactic Center Excess with Multi-Messenger Observations. 12 2021.

Laura Chomiuk and Matthew S. Povich. Toward a unification of star formation rate determinations in the milky way and other galaxies. *The Astronomical Journal*, 142

(6):197, Nov 2011. ISSN 1538-3881. doi:10.1088/0004-6256/142/6/197. URL http://dx.doi.org/10.1088/0004-6256/142/6/197.

Shaun Cole, Peder Norberg, Carlton M. Baugh, Carlos S. Frenk, Joss Bland-Hawthorn, Terry Bridges, Russell Cannon, Matthew Colless, Chris Collins, Warrick Couch, and et al. The 2df galaxy redshift survey: near-infrared galaxy luminosity functions. *Monthly Notices of the Royal Astronomical Society*, 326(1):255â273, Sep 2001. ISSN 1365-2966. doi:10.1046/j.1365-8711.2001.04591.x. URL http://dx.doi.org/10.1046/j.1365-8711.2001.04591.x.

Thomas E. Collett. The Population of Galaxy-Galaxy Strong Lenses in Forthcoming Optical Imaging Surveys. , 811(1):20, September 2015. doi:10.1088/0004-637X/811/1/20.

J. M. Cordes, I. Wasserman, J. W. T. Hessels, T. J. W. Lazio, S. Chatterjee, and R. S. Wharton. Lensing of Fast Radio Bursts by Plasma Structures in Host Galaxies. , 842(1): 35, June 2017. doi:10.3847/1538-4357/aa74da.

Virginia L. Corless and Lindsay J. King. A statistical study of weak lensing by triaxial dark matter haloes: consequences for parameter estimation. , 380(1):149–161, September 2007. doi:10.1111/j.1365-2966.2007.12018.x.

A. Cuoco, E. Komatsu, and J. M. Siegal-Gaskins. Joint anisotropy and source count constraints on the contribution of blazars to the diffuse gamma-ray background. *Phys. Rev. D*, 86:063004, 2012. doi:10.1103/PhysRevD.86.063004.

Giulia Cusin, Ruth Durrer, and Irina Dvorkin. Strong and weak lensing of Gravitational Waves: a semi-analytical approach. 12 2019.

Liang Dai and Tejaswi Venumadhav. On the waveforms of gravitationally lensed gravitational waves. *arXiv e-prints*, art. arXiv:1702.04724, February 2017.

Liang Dai and Tejaswi Venumadhav. On the waveforms of gravitationally lensed gravitational waves. 2 2017.

Liang Dai, Tejaswi Venumadhav, and Kris Sigurdson. Effect of lensing magnification on the apparent distribution of black hole mergers. , 95(4):044011, February 2017. doi:10.1103/PhysRevD.95.044011.

Liang Dai, Barak Zackay, Tejaswi Venumadhav, Javier Roulet, and Matias Zaldarriaga. Search for Lensed Gravitational Waves Including Morse Phase Information: An Intriguing Candidate in O2. *arXiv e-prints*, art. arXiv:2007.12709, July 2020.

Adam N. Davis, Dragan Huterer, and Lawrence M. Krauss. Strong lensing constraints on the velocity dispersion and density profile of elliptical galaxies. , 344(4):1029–1040, October 2003. doi:10.1046/j.1365-8711.2003.06789.x.

Tansu Daylan, Douglas P. Finkbeiner, Dan Hooper, Tim Linden, Stephen K. N. Portillo, Nicholas L. Rodd, and Tracy R. Slatyer. The characterization of the gamma-ray signal from the central Milky Way: A case for annihilating dark matter. *Phys. Dark Univ.*, 12: 1–23, 2016. doi:10.1016/j.dark.2015.12.005.

M. Di Mauro, F. Calore, F. Donato, M. Ajello, and L. Latronico. Diffuse γ-ray emission from misaligned active galactic nuclei. *Astrophys. J.*, 780:161, 2014. doi:10.1088/0004-637X/780/2/161.

Mattia Di Mauro. Characteristics of the Galactic Center excess measured with 11 years of *Fermi*-LAT data. *Phys. Rev. D*, 103(6):063029, 2021. doi:10.1103/PhysRevD.103.063029.

Mattia Di Mauro, Martin Stref, and Francesca Calore. Investigating the effect of Milky Way dwarf spheroidal galaxies extension on dark matter searches with Fermi-LAT data. , 106 (12):123032, December 2022. doi:10.1103/PhysRevD.106.123032.

Mattia Di Mauro, Martin Stref, and Francesca Calore. Investigating the effect of Milky Way dwarf spheroidal galaxies extension on dark matter searches with Fermi-LAT data. *Phys. Rev. D*, 106(12):123032, 2022. doi:10.1103/PhysRevD.106.123032.

J. M. Diego. The Universe at extreme magnification. , 625:A84, May 2019. doi:10.1051/0004-6361/201833670.

Jose M. Diego, Nick Kaiser, Tom Broadhurst, Patrick L. Kelly, Steve Rodney, Takahiro Morishita, Masamune Oguri, Timothy W. Ross, Adi Zitrin, Mathilde Jauzac, Johan Richard, Liliya Williams, Jesus Vega-Ferrero, Brenda Frye, and Alexei V. Filippenko. Dark Matter under the Microscope: Constraining Compact Dark Matter with Caustic Crossing Events. , 857(1):25, April 2018. doi:10.3847/1538-4357/aab617.

Roland Diehl, Hubert Halloin, Karsten Kretschmer, Giselher G. Lichti, Volker Schönfelder, Andrew W. Strong, Andreas von Kienlin, Wei Wang, Pierre Jean, Jürgen Knödlseder, Jean-Pierre Roques, Georg Weidenspointner, Stephane Schanne, Dieter H. Hartmann, Christoph Winkler, and Cornelia Wunderer. Radioactive ^{26}Al from massive stars in the Galaxy. , 439(7072):45–47, January 2006. doi:10.1038/nature04364.

Xuheng Ding, Marek Biesiada, and Zong-Hong Zhu. Strongly lensed gravitational waves from intrinsically faint double compact binaries—prediction for the Einstein Telescope. , 2015(12):006, December 2015. doi:10.1088/1475-7516/2015/12/006.

Michal Dominik, Krzysztof Belczynski, Christopher Fryer, Daniel E. Holz, Emanuele Berti, Tomasz Bulik, Ilya Mand el, and Richard O'Shaughnessy. Double Compact Objects. II. Cosmological Merger Rates. , 779(1):72, December 2013. doi:10.1088/0004-637X/779/1/72.

Michal Dominik, Emanuele Berti, Richard O'Shaughnessy, Ilya Mandel, Krzysztof Belczynski, Christopher Fryer, Daniel E. Holz, Tomasz Bulik, and Francesco Pannarale. Double Compact Objects III: Gravitational-wave Detection Rates. , 806(2):263, June 2015. doi:10.1088/0004-637X/806/2/263.

A. DomÃnguez, J. R. Primack, D. J. Rosario, F. Prada, R. C. Gilmore, S. M. Faber, D. C. Koo, R. S. Somerville, M. A. PÃ©rez-Torres, P. PÃ©rez-GonzÃ¡lez, and et al. Extragalactic background light inferred from aegis galaxy-sed-type fractions. *Monthly Notices of the Royal Astronomical Society*, 410(4):2556â2578, Oct 2010. ISSN 0035-8711. doi:10.1111/j.1365-2966.2010.17631.x. URL http://dx.doi.org/10.1111/j.1365-2966.2010.17631.x.

A. Drlica-Wagner et al. Search for Gamma-Ray Emission from DES Dwarf Spheroidal Galaxy Candidates with Fermi-LAT Data. *Astrophys. J. Lett.*, 809(1):L4, 2015. doi:10.1088/2041-8205/809/1/L4.

Alex Drlica-Wagner et al. Probing the Fundamental Nature of Dark Matter with the Large Synoptic Survey Telescope. 2 2019.

et al. Drlica-Wagner, A. Eight Ultra-faint Galaxy Candidates Discovered in Year Two of the Dark Energy Survey. , 813(2):109, November 2015. doi:10.1088/0004-637X/813/2/109.

Alan R. Duffy, Joop Schaye, Scott T. Kay, Claudio Dalla Vecchia, Richard A. Battye, and C. M. Booth. Impact of baryon physics on dark matter structures: a detailed simulation study of halo density profiles. , 405(4):2161–2178, July 2010. doi:10.1111/j.1365-2966.2010.16613.x.

Addy J. Evans, Louis E. Strigari, Oskar Svenborn, Andrea Albert, J. Patrick Harding, Dan Hooper, Tim Linden, and Andrew B. Pace. On the gamma-ray emission from the core of the Sagittarius dwarf galaxy. *Mon. Not. Roy. Astron. Soc.*, 524:4574–4585, 2023. doi:10.1093/mnras/stad2074.

Jose M. Ezquiaga, Daniel E. Holz, Wayne Hu, Macarena Lagos, and Robert M. Wald. Phase effects from strong gravitational lensing of gravitational waves. *arXiv e-prints*, art. arXiv:2008.12814, August 2020.

Jose María Ezquiaga, Daniel E. Holz, Wayne Hu, Macarena Lagos, and Robert M. Wald. Phase effects from strong gravitational lensing of gravitational waves. 8 2020.

S. M. Faber and R. E. Jackson. Velocity dispersions and mass-to-light ratios for elliptical galaxies. , 204:668–683, March 1976. doi:10.1086/154215.

Ke Fang and Kohta Murase. Multi-messenger Implications of Sub-PeV Diffuse Galactic Gamma-Ray Emission. *Astrophys. J.*, 919:93, 2021. doi:10.3847/1538-4357/ac11f0.

Robert Feldmann, Dan Hooper, and Nickolay Y. Gnedin. Circum-galactic gas and the isotropic gamma-ray background. *The Astrophysical Journal*, 763(1):21, Dec 2012. ISSN 1538-4357. doi:10.1088/0004-637x/763/1/21. URL http://dx.doi.org/10.1088/0004-637X/763/1/21.

Maya Fishbach and Vicky Kalogera. The time delay distribution and formation metallicity of LIGO-Virgo's binary black holes. 5 2021.

D. J. Fixsen. THE TEMPERATURE OF THE COSMIC MICROWAVE BACKGROUND. *The Astrophysical Journal*, 707(2):916–920, nov 2009. doi:10.1088/0004-637x/707/2/916. URL https://doi.org/10.1088%2F0004-637x%2F707%2F2%2F916.

Chris L. Fryer, Krzysztof Belczynski, Grzegorz Wiktorowicz, Michal Dominik, Vicky Kalogera, and Daniel E. Holz. Compact remnant mass function: Dependence on the explosion mechanism and metallicity. *The Astrophysical Journal*, 749(1):91, Mar 2012. ISSN 1538-4357. doi:10.1088/0004-637x/749/1/91. URL http://dx.doi.org/10.1088/0004-637X/749/1/91.

Stefano Gabici and Pasquale Blasi. The Gamma-ray background from large scale structure formation. *Astropart. Phys.*, 19:679–689, 2003. doi:10.1016/S0927-6505(03)00106-3.

Stefano Gabici and Pasquale Blasi. On the Detectability of gamma-rays from clusters of galaxies: Mergers versus secondary infall. *Astropart. Phys.*, 20:579–590, 2004. doi:10.1016/j.astropartphys.2003.09.002.

Graciela B Gelmini, Oleg Kalashev, and Dmitri V Semikoz. Gamma-ray constraints on maximum cosmogenic neutrino fluxes and uhecr source evolution models. *Journal of Cosmology and Astroparticle Physics*, 2012(01):044â044, Jan 2012. ISSN 1475-7516. doi:10.1088/1475-7516/2012/01/044. URL http://dx.doi.org/10.1088/1475-7516/2012/01/044.

Thorsten Glüsenkamp. Analysis of the cumulative neutrino flux from Fermi-LAT blazar populations using 3 years of IceCube data. *EPJ Web Conf.*, 121:05006, 2016. doi:10.1051/epjconf/201612105006.

Oleg Y. Gnedin, Andrey V. Kravtsov, Anatoly A. Klypin, and Daisuke Nagai. Response of dark matter halos to condensation of baryons: Cosmological simulations and improved adiabatic contraction model. *The Astrophysical Journal*, 616(1):16–26, nov 2004. doi:10.1086/424914. URL https://doi.org/10.1086%2F424914.

Oleg Y. Gnedin, Daniel Ceverino, Nickolay Y. Gnedin, Anatoly A. Klypin, Andrey V. Kravtsov, Robyn Levine, Daisuke Nagai, and Gustavo Yepes. Halo contraction effect in hydrodynamic simulations of galaxy formation, 2011.

Lisa Goodenough and Dan Hooper. Possible Evidence For Dark Matter Annihilation In The Inner Milky Way From The Fermi Gamma Ray Space Telescope. 10 2009.

Chris Gordon and Oscar Macias. Dark Matter and Pulsar Model Constraints from Galactic Center Fermi-LAT Gamma Ray Observations. *Phys. Rev. D*, 88(8):083521, 2013. doi:10.1103/PhysRevD.88.083521. [Erratum: Phys.Rev.D 89, 049901 (2014)].

F. Governato, A. Zolotov, A. Pontzen, C. Christensen, S. H. Oh, A. M. Brooks, T. Quinn, S. Shen, and J. Wadsley. Cuspy no more: how outflows affect the central dark matter and baryon distribution in {*upLambda* cold dark matter galaxies. *Monthly Notices of the Royal Astronomical Society*, 422(2):1231–1240, mar 2012. doi:10.1111/j.1365-2966.2012.20696.x. URL https://doi.org/10.1111%2Fj.1365-2966.2012.20696.x.

et al. H. Abdallah. Search for dark matter annihilations towards the inner galactic halo from 10 years of observations with h.e.s.s. *Physical Review Letters*, 117(11), sep 2016. doi:10.1103/physrevlett.117.111301. URL `https://doi.org/10.1103%2Fphysrevlett.117.111301`.

O. A. Hannuksela, K. Haris, K. K. Y. Ng, S. Kumar, A. K. Mehta, D. Keitel, T. G. F. Li, and P. Ajith. Search for Gravitational Lensing Signatures in LIGO-Virgo Binary Black Hole Events. , 874(1):L2, March 2019. doi:10.3847/2041-8213/ab0c0f.

J. Patrick Harding and Kevork N. Abazajian. Models of the Contribution of Blazars to the Anisotropy of the Extragalactic Diffuse Gamma-ray Background. *JCAP*, 11:026, 2012. doi:10.1088/1475-7516/2012/11/026.

Jonathan R. Hargis, Beth Willman, and Annika H. G. Peter. Too Many, Too Few, or Just Right? The Predicted Number and Distribution of Milky Way Dwarf Galaxies. *Astrophys. J. Lett.*, 795(1):L13, 2014. doi:10.1088/2041-8205/795/1/L13.

K. Haris, Ajit Kumar Mehta, Sumit Kumar, Tejaswi Venumadhav, and Parameswaran Ajith. Identifying strongly lensed gravitational wave signals from binary black hole mergers. *arXiv e-prints*, art. arXiv:1807.07062, July 2018.

Chen He, Keith Bechtol, Andrew P. Hearin, and Dan Hooper. Prospects for Detecting Gamma Rays from Annihilating Dark Matter in Dwarf Galaxies in the Era of the Dark Energy Survey and Large Synoptic Survey Telescope. *Phys. Rev. D*, 91(6):063515, 2015. doi:10.1103/PhysRevD.91.063515.

Stefan Hilbert, Simon D. M. White, Jan Hartlap, and Peter Schneider. Strong-lensing optical depths in a ΛCDM universe - II. The influence of the stellar mass in galaxies. , 386(4): 1845–1854, June 2008. doi:10.1111/j.1365-2966.2008.13190.x.

M. Hoeft, J. P. Mücket, and S. Gottlöber. Velocity Dispersion Profiles in Dark Matter Halos. , 602(1):162–169, February 2004. doi:10.1086/380990.

Henk Hoekstra, H. K. C. Yee, and Michael D. Gladders. Properties of Galaxy Dark Matter Halos from Weak Lensing. , 606(1):67–77, May 2004. doi:10.1086/382726.

Daniel E. Holz. Seeing Double: Strong Gravitational Lensing of High-Redshift Supernovae. , 556(2):L71–L74, August 2001. doi:10.1086/322947.

Daniel E. Holz, M. Coleman Miller, and Jean M. Quashnock. Gravitational Lensing Limits on the Average Redshift of Gamma-Ray Bursts. , 510(1):54–63, January 1999. doi:10.1086/306568.

D. Hooper. TASI Lectures on Indirect Searches For Dark Matter. In *TASI 2018 - Theory in an Era of Data*, page 10, June 2018. doi:10.22323/1.333.0010.

Dan Hooper. A Case for Radio Galaxies as the Sources of IceCube's Astrophysical Neutrino Flux. *JCAP*, 09:002, 2016. doi:10.1088/1475-7516/2016/09/002.

Dan Hooper. *Particle Cosmology and Astrophysics*. Princeton University Press, Princeton, NJ, 2022. ISBN 9780691235042. URL https://press.princeton.edu/books/hardcover/9780691235042/particle-cosmology-and-astrophysics.

Dan Hooper and Lisa Goodenough. Dark Matter Annihilation in The Galactic Center As Seen by the Fermi Gamma Ray Space Telescope. *Phys. Lett. B*, 697:412–428, 2011. doi:10.1016/j.physletb.2011.02.029.

Dan Hooper and Tim Linden. On The Origin Of The Gamma Rays From The Galactic Center. *Phys. Rev. D*, 84:123005, 2011. doi:10.1103/PhysRevD.84.123005.

Dan Hooper and Tim Linden. On The Gamma-Ray Emission From Reticulum II and Other Dwarf Galaxies. *JCAP*, 09:016, 2015. doi:10.1088/1475-7516/2015/09/016.

Dan Hooper and Tim Linden. Millisecond Pulsars, TeV Halos, and Implications For The Galactic Center Gamma-Ray Excess. *Phys. Rev. D*, 98(4):043005, 2018. doi:10.1103/PhysRevD.98.043005.

Dan Hooper and Tim Linden. Evidence of tev halos around millisecond pulsars, 2021.

Dan Hooper and Tracy R. Slatyer. Two Emission Mechanisms in the Fermi Bubbles: A Possible Signal of Annihilating Dark Matter. *Phys. Dark Univ.*, 2:118–138, 2013. doi:10.1016/j.dark.2013.06.003.

Dan Hooper, Tim Linden, and Alejandro Lopez. Radio Galaxies Dominate the High-Energy Diffuse Gamma-Ray Background. *JCAP*, 08:019, 2016. doi:10.1088/1475-7516/2016/08/019.

Dan Hooper, Ilias Cholis, Tim Linden, and Ke Fang. HAWC Observations Strongly Favor Pulsar Interpretations of the Cosmic-Ray Positron Excess. *Phys. Rev. D*, 96(10):103013, 2017. doi:10.1103/PhysRevD.96.103013.

Dan Hooper, Tim Linden, and Abby Vieregg. Active Galactic Nuclei and the Origin of IceCube's Diffuse Neutrino Flux. *JCAP*, 02:012, 2019. doi:10.1088/1475-7516/2019/02/012.

Andrew M. Hopkins and John F. Beacom. On the normalization of the cosmic star formation history. *The Astrophysical Journal*, 651(1):142â154, Nov 2006. ISSN 1538-4357. doi:10.1086/506610. URL http://dx.doi.org/10.1086/506610.

Shunsaku Horiuchi, John F. Beacom, Christopher S. Kochanek, Jose L. Prieto, K. Z. Stanek, and Todd A. Thompson. The cosmic core-collapse supernova rate does not match the massive-star formation rate. *The Astrophysical Journal*, 738(2):154, Aug 2011. ISSN 1538-4357. doi:10.1088/0004-637x/738/2/154. URL http://dx.doi.org/10.1088/0004-637X/738/2/154.

A. P. Igoshev and S. B. Popov. Neutron starâs initial spin period distribution. *Monthly Notices of the Royal Astronomical Society*, 432(2):967â972, Apr 2013. ISSN 1365-2966. doi:10.1093/mnras/stt519. URL http://dx.doi.org/10.1093/mnras/stt519.

Yoshiyuki Inoue. Contribution of gamma-ray-loud radio galaxiesâ core emissions to the cosmic mev and gev gamma-ray background radiation. *The Astrophysical Journal*, 733(1): 66, May 2011. ISSN 1538-4357. doi:10.1088/0004-637x/733/1/66. URL http://dx.doi.org/10.1088/0004-637X/733/1/66.

S. Johnston and D. Galloway. Pulsar braking indices revisited. *Monthly Notices of the Royal Astronomical Society*, 306(4):L50âL54, Jul 1999. ISSN 1365-2966. doi:10.1046/j.1365-8711.1999.02737.x. URL http://dx.doi.org/10.1046/j.1365-8711.1999.02737.x.

Chris Karwin, Simona Murgia, Sheldon Campbell, and Igor Moskalenko. *Fermi*-LAT Observations of γ-Ray Emission Towards the Outer Halo of M31. *PoS*, ICRC2019:570, 2021a. doi:10.22323/1.358.0570.

Christopher M. Karwin, Simona Murgia, Igor Moskalenko, Sean Fillingham, Anne-Katherine Burns, and Max Fieg. Dark matter interpretation of the *Fermi*-LAT observations toward the outer halo of M31. *Phys. Rev. D*, 103(2):023027, 2021b. doi:10.1103/PhysRevD.103.023027.

V. M. Kaspi, M. E. Roberts, G. Vasisht, E. V. Gotthelf, M. Pivovaroff, and N. Kawai. Chandraxâray observations of g11.2â0.3: Implications for pulsar ages. *The Astrophysical Journal*, 560(1):371â377, Oct 2001. ISSN 1538-4357. doi:10.1086/322515. URL http://dx.doi.org/10.1086/322515.

Charles R. Keeton and Piero Madau. Lensing Constraints on the Cores of Massive Dark Matter Halos. , 549(1):L25–L28, March 2001. doi:10.1086/319136.

Robert C. Kennicutt, Jr. and Neal J. Evans, II. Star Formation in the Milky Way and Nearby Galaxies. *Ann. Rev. Astron. Astrophys.*, 50:531–608, 2012. doi:10.1146/annurev-astro-081811-125610.

Uri Keshet, Eli Waxman, Abraham Loeb, Volker Springel, and Lars Hernquist. Gamma-rays from intergalactic shocks. *Astrophys. J.*, 585:128–150, 2003. doi:10.1086/345946.

Carolyn A. Kierans. AMEGO: exploring the extreme multi-messenger universe. In Jan-Willem A. den Herder, Kazuhiro Nakazawa, and Shouleh Nikzad, editors, *Space Telescopes and Instrumentation 2020: Ultraviolet to Gamma Ray*. SPIE, dec 2020. doi:10.1117/12.2562352. URL https://doi.org/10.1117%2F12.2562352.

Kyungmin Kim, Joongoo Lee, Robin S. H. Yuen, Otto Akseli Hannuksela, and Tjonnie G. F. Li. Identification of Lensed Gravitational Waves with Deep Learning. *arXiv e-prints*, art. arXiv:2010.12093, October 2020.

Andrey Kolmogorov. Sulla determinazione empirica di una legge di distribuzione. *Giornale dellâIstituto Italiano degli Attuari*, 4:83–91, 1933.

Sergey E. Koposov, Vasily Belokurov, Gabriel Torrealba, and N. Wyn Evans. Beasts of the Southern Wild: Discovery of Nine Ultra Faint Satellites in the Vicinity of the Magellanic Clouds. , 805(2):130, June 2015. doi:10.1088/0004-637X/805/2/130.

R. Kormann, P. Schneider, and M. Bartelmann. Isothermal elliptical gravitational lens models. , 284:285–299, April 1994.

Pavel Kroupa. On the variation of the initial mass function. *mnras*, 322(2):231–246, April 2001. doi:10.1046/j.1365-8711.2001.04022.x.

N. Langer and C. A. Norman. On the Collapsar Model of Long Gamma-Ray Bursts:Constraints from Cosmic Metallicity Evolution. , 638(2):L63–L66, February 2006. doi:10.1086/500363.

N. Langer and C. A. Norman. On the collapsar model of long gamma-ray bursts:constraints from cosmic metallicity evolution. *The Astrophysical Journal*, 638(2):L63âL66, Jan 2006. ISSN 1538-4357. doi:10.1086/500363. URL `http://dx.doi.org/10.1086/500363`.

Jesse Leaman, Weidong Li, Ryan Chornock, and Alexei V. Filippenko. Nearby supernova rates from the Lick Observatory Supernova Search - I. The methods and data base. *mnras*, 412(3):1419–1440, April 2011. doi:10.1111/j.1365-2966.2011.18158.x.

Shun-Sheng Li, Shude Mao, Yuetong Zhao, and Youjun Lu. Gravitational lensing of gravitational waves: a statistical perspective. , 476(2):2220–2229, May 2018. doi:10.1093/mnras/sty411.

Weidong Li, Ryan Chornock, Jesse Leaman, Alexei V. Filippenko, Dovi Poznanski, Xiaofeng Wang, Mohan Ganeshalingam, and Filippo Mannucci. Nearby supernova rates from the Lick Observatory Supernova Search - III. The rate-size relation, and the rates as a function of galaxy Hubble type and colour. *mnras*, 412(3):1473–1507, April 2011a. doi:10.1111/j.1365-2966.2011.18162.x.

Weidong Li, Jesse Leaman, Ryan Chornock, Alexei V. Filippenko, Dovi Poznanski, Mohan Ganeshalingam, Xiaofeng Wang, Maryam Modjaz, Saurabh Jha, Ryan J. Foley, and Nathan Smith. Nearby supernova rates from the Lick Observatory Supernova Search - II. The observed luminosity functions and fractions of supernovae in a complete sample. *mnras*, 412(3):1441–1472, April 2011b. doi:10.1111/j.1365-2966.2011.18160.x.

Xue Li, Jens Hjorth, and Johan Richard. The rates and time-delay distribution of multiply imaged supernovae behind lensing clusters. , 2012(11):015, November 2012. doi:10.1088/1475-7516/2012/11/015.

Timothy C. Licquia and Jeffrey A. Newman. Improved estimates of the milky wayâs stellar mass and star formation rate from hierarchical bayesian meta-analysis. *The Astrophysical Journal*, 806(1):96, Jun 2015. ISSN 1538-4357. doi:10.1088/0004-637x/806/1/96. URL `http://dx.doi.org/10.1088/0004-637X/806/1/96`.

Tim Linden. Star-Forming Galaxies Significantly Contribute to the Isotropic Gamma-Ray Background. *Phys. Rev. D*, 96(8):083001, 2017. doi:10.1103/PhysRevD.96.083001.

Tim Linden and Benjamin J. Buckman. Pulsar TeV Halos Explain the Diffuse TeV Excess Observed by Milagro. *Phys. Rev. Lett.*, 120(12):121101, 2018. doi:10.1103/PhysRevLett.120.121101.

Tim Linden, Katie Auchettl, Joseph Bramante, Ilias Cholis, Ke Fang, Dan Hooper, Tanvi Karwal, and Shirley Weishi Li. Using HAWC to discover invisible pulsars. *Phys. Rev. D*, 96(10):103016, 2017. doi:10.1103/PhysRevD.96.103016.

Xiaoshu Liu, Ignacio Magana Hernandez, and Jolien Creighton. Identifying strong gravitational-wave lensing during the second observing run of Advanced LIGO and Advanced Virgo. *arXiv e-prints*, art. arXiv:2009.06539, September 2020a.

Yuting Liu, Shuo Cao, Tonghua Liu, Xiaolei Li, Shuaibo Geng, Yujie Lian, and Wuzheng Guo. Model-independent constraints on cosmic curvature: implication from updated Hubble diagram of high-redshift standard candles. *arXiv e-prints*, art. arXiv:2008.08378, August 2020b.

D. R. Lorimer, A. J. Faulkner, A. G. Lyne, R. N. Manchester, M. Kramer, M. A. McLaughlin, G. Hobbs, A. Possenti, I. H. Stairs, F. Camilo, M. Burgay, N. D'Amico, A. Corongiu, and F. Crawford. The Parkes Multibeam Pulsar Survey - VI. Discovery and timing of 142 pulsars and a Galactic population analysis. *mnras*, 372(2):777–800, October 2006. doi:10.1111/j.1365-2966.2006.10887.x.

Piero Madau and Mark Dickinson. Cosmic Star-Formation History. , 52:415–486, August 2014. doi:10.1146/annurev-astro-081811-125615.

Piero Madau and Mark Dickinson. Cosmic star-formation history. *Annual Review of Astronomy and Astrophysics*, 52(1):415â486, Aug 2014. ISSN 1545-4282. doi:10.1146/annurev-astro-081811-125615. URL `http://dx.doi.org/10.1146/annurev-astro-081811-125615`.

Michele Maggiore, Chris Van Den Broeck, Nicola Bartolo, Enis Belgacem, Daniele Bertacca, Marie Anne Bizouard, Marica Branchesi, Sebastien Clesse, Stefano Foffa, Juan García-Bellido, Stefan Grimm, Jan Harms, Tanja Hinderer, Sabino Matarrese, Cristiano Palomba, Marco Peloso, Angelo Ricciardone, and Mairi Sakellariadou. Science case for the Einstein telescope. , 2020(3):050, March 2020. doi:10.1088/1475-7516/2020/03/050.

MAGIC Collaboration. Limits to dark matter annihilation cross-section from a combined analysis of MAGIC and Fermi-LAT observations of dwarf satellite galaxies. , 2016(2): 039–039, February 2016. doi:10.1088/1475-7516/2016/02/039.

Dmitry Malyshev and David W. Hogg. Statistics of Gamma-Ray Point Sources below the Fermi Detection Limit. , 738(2):181, September 2011. doi:10.1088/0004-637X/738/2/181.

R N Manchester, G B Hobbs, A Teoh, and M Hobbs. The Australia Telescope National Facility pulsar catalogue. *Astron. J.*, 129:1993, 2005. doi:10.1086/428488.

Dan Maoz, Filippo Mannucci, Weidong Li, Alexei V. Filippenko, Massimo Della Valle, and Nino Panagia. Nearby supernova rates from the lick observatory supernova search - iv. a recovery method for the delay-time distribution. *Monthly Notices of the Royal Astronomical Society*, 412(3):1508â1521, Mar 2011. ISSN 0035-8711. doi:10.1111/j.1365-2966.2010.16808.x. URL `http://dx.doi.org/10.1111/j.1365-2966.2010.16808.x`.

Lea Marcotulli, Mattia Di Mauro, and Marco Ajello. Source-count Distribution of Gamma-Ray Blazars. *Astrophys. J.*, 896(1):6, 2020. doi:10.3847/1538-4357/ab8cbd.

Michael Marks, Pavel Kroupa, JÃ¶rg Dabringhausen, and Marcel S. Pawlowski. Evidence for top-heavy stellar initial mass functions with increasing density and decreasing metallicity. *Monthly Notices of the Royal Astronomical Society*, 422(3):2246â2254, Mar 2012. ISSN 0035-8711. doi:10.1111/j.1365-2966.2012.20767.x. URL `http://dx.doi.org/10.1111/j.1365-2966.2012.20767.x`.

Gregory D. Martinez. A robust determination of Milky Way satellite properties using hierarchical mass modelling. , 451(3):2524–2535, August 2015. doi:10.1093/mnras/stv942.

Richard Massey, Thomas Kitching, and Johan Richard. The dark matter of gravitational lensing. *Reports on Progress in Physics*, 73(8):086901, August 2010. doi:10.1088/0034-4885/73/8/086901.

J. C. Mather. The Cosmic Background Explorer (COBE). *Optical Engineering*, 21:769–774, August 1982. doi:10.1117/12.7972975.

Mattia Di Mauro. The origin of the fermi-lat γ-ray background, 2016.

Nicholas J. McConnell and Chung-Pei Ma. Revisiting the Scaling Relations of Black Hole Masses and Host Galaxy Properties. , 764(2):184, February 2013. doi:10.1088/0004-637X/764/2/184.

Alex McDaniel, Tesla Jeltema, and Stefano Profumo. Exploring a cosmic-ray origin of the multiwavelength emission in M31. *Phys. Rev. D*, 100(2):023014, 2019. doi:10.1103/PhysRevD.100.023014.

Connor McIsaac, David Keitel, Thomas Collett, Ian Harry, Simone Mozzon, Oliver Edy, and David Bacon. Search for strongly lensed counterpart images of binary black hole mergers in the first two LIGO observing runs. , 102(8):084031, October 2020. doi:10.1103/PhysRevD.102.084031.

Massimo Meneghetti, Guido Davoli, Pietro Bergamini, Piero Rosati, Priyamvada Natarajan, Carlo Giocoli, Gabriel B. Caminha, R. Benton Metcalf, Elena Rasia, Stefano Borgani, Francesco Calura, Claudio Grillo, Amata Mercurio, and Eros Vanzella. An excess of small-scale gravitational lenses observed in galaxy clusters. *Science*, 369(6509):1347–1351, September 2020. doi:10.1126/science.aax5164.

Julian B. Muñoz, Ely D. Kovetz, Liang Dai, and Marc Kamionkowski. Lensing of Fast Radio Bursts as a Probe of Compact Dark Matter. , 117(9):091301, August 2016. doi:10.1103/PhysRevLett.117.091301.

Suvodip Mukherjee, Tom Broadhurst, Jose M. Diego, Joseph Silk, and George F. Smoot. Inferring the lensing rate of LIGO-Virgo sources from the stochastic gravitational wave background. *Mon. Not. Roy. Astron. Soc.*, 501(2):2451–2466, 2021. doi:10.1093/mnras/staa3813.

Kohta Murase. High-Energy Emission Induced by Ultra-high-Energy Photons as a Probe of Ultra-high-Energy Cosmic-Ray Accelerators Embedded in the Cosmic Web. *Astrophys. J. Lett.*, 745:L16, 2012. doi:10.1088/2041-8205/745/2/L16.

Kohta Murase and John F. Beacom. Constraining Very Heavy Dark Matter Using Diffuse Backgrounds of Neutrinos and Cascaded Gamma Rays. *JCAP*, 10:043, 2012. doi:10.1088/1475-7516/2012/10/043.

Kohta Murase, John F. Beacom, and Hajime Takami. Gamma-Ray and Neutrino Backgrounds as Probes of the High-Energy Universe: Hints of Cascades, General Constraints, and Implications for TeV Searches. *JCAP*, 08:030, 2012. doi:10.1088/1475-7516/2012/08/030.

Kohta Murase, Charles D. Dermer, Hajime Takami, and Giulia Migliori. Blazars as Ultra-high-energy Cosmic-ray Sources: Implications for TeV Gamma-Ray Observations. , 749 (1):63, April 2012. doi:10.1088/0004-637X/749/1/63.

Ethan O. Nadler, Arka Banerjee, Susmita Adhikari, Yao-Yuan Mao, and Risa H. Wechsler. The Effects of Dark Matter and Baryonic Physics on the Milky Way Subhalo Population in the Presence of the Large Magellanic Cloud. , 920(1):L11, October 2021. doi:10.3847/2041-8213/ac29c1.

Ramesh Narayan and Matthias Bartelmann. Lectures on Gravitational Lensing. *arXiv e-prints*, art. astro-ph/9606001, June 1996.

Julio F. Navarro, Carlos S. Frenk, and Simon D. M. White. The Structure of Cold Dark Matter Halos. , 462:563, May 1996. doi:10.1086/177173.

Julio F. Navarro, Carlos S. Frenk, and Simon D. M. White. A Universal Density Profile from Hierarchical Clustering. , 490(2):493–508, December 1997. doi:10.1086/304888.

Ken K. Y. Ng, Kaze W. K. Wong, Tom Broadhurst, and Tjonnie G. F. Li. Precise LIGO Lensing Rate Predictions for Binary Black Holes. *Phys. Rev. D*, 97(2):023012, 2018. doi:10.1103/PhysRevD.97.023012.

Masamune Oguri. Effect of gravitational lensing on the distribution of gravitational waves from distant binary black hole mergers. , 480(3):3842–3855, November 2018. doi:10.1093/mnras/sty2145.

Masamune Oguri, Atsushi Taruya, Yasushi Suto, and Edwin L. Turner. Strong Gravitational Lensing Time Delay Statistics and the Density Profile of Dark Halos. , 568(2):488–499, April 2002. doi:10.1086/339064.

J. P. Ostriker and J. E. Gunn. On the Nature of Pulsars. I. Theory. , 157:1395, September 1969. doi:10.1086/150160.

Andrew B. Pace and Louis E. Strigari. Scaling relations for dark matter annihilation and decay profiles in dwarf spheroidal galaxies. , 482(3):3480–3496, January 2019. doi:10.1093/mnras/sty2839.

Andrew B. Pace and Louis E. Strigari. Scaling Relations for Dark Matter Annihilation and Decay Profiles in Dwarf Spheroidal Galaxies. *Mon. Not. Roy. Astron. Soc.*, 482(3): 3480–3496, 2019. doi:10.1093/mnras/sty2839.

Andrew B. Pace, Matthew G. Walker, Sergey E. Koposov, Nelson Caldwell, Mario Mateo, Edward W. Olszewski, III Bailey, John I., and Mei-Yu Wang. Spectroscopic Confirmation of the Sixth Globular Cluster in the Fornax Dwarf Spheroidal Galaxy. , 923(1):77, December 2021. doi:10.3847/1538-4357/ac2cd2.

Vasiliki Pavlidou and Brian D. Fields. The guaranteed gamma-ray background. *The Astrophysical Journal*, 575(1):L5–L8, aug 2002. doi:10.1086/342670. URL `https://doi.org/10.1086%2F342670`.

Joachim Wambsganss Peter Schneider, Christopher Kochanek. *Gravitational Lensing: Strong, Weak and Micro: Saas-Fee Advanced Course 33 (Saas-Fee Advanced Courses)*. 1 edition, 2006. ISBN 354030309X,9783540303091. URL `http://gen.lib.rus.ec/book/index.php?md5=7aeb5cf9f38ad723d46b9048c99aa022`.

Aleksandra Piórkowska, Marek Biesiada, and Zong-Hong Zhu. Strong gravitational lensing of gravitational waves in Einstein Telescope. , 2013(10):022, October 2013. doi:10.1088/1475-7516/2013/10/022.

Planck Collaboration and et al. Aghanim, N. Planck 2018 results. I. Overview and the cosmological legacy of Planck. , 641:A1, September 2020. doi:10.1051/0004-6361/201833880.

Planck Collaboration, N. Aghanim, et al. Planck 2018 results. VI. Cosmological parameters. , 641:A6, September 2020. doi:10.1051/0004-6361/201833910.

S. B. Popov and R. Turolla. Initial spin periods of neutron stars in supernova remnants. *Astrophysics and Space Science*, 341(2):457â464, May 2012. ISSN 1572-946X. doi:10.1007/s10509-012-1100-z. URL `http://dx.doi.org/10.1007/s10509-012-1100-z`.

Konstantin A. Postnov and Lev R. Yungelson. The Evolution of Compact Binary Star Systems. *Living Reviews in Relativity*, 9(1):6, December 2006. doi:10.12942/lrr-2006-6.

Konstantin A. Postnov and Lev R. Yungelson. The Evolution of Compact Binary Star Systems. *Living Reviews in Relativity*, 17(1):3, May 2014. doi:10.12942/lrr-2014-3.

William H. Press and Paul Schechter. Formation of Galaxies and Clusters of Galaxies by Self-Similar Gravitational Condensation. , 187:425–438, February 1974. doi:10.1086/152650.

S. Rahmani, S. Lianou, and P. Barmby. Star formation laws in the andromeda galaxy: gas, stars, metals and the surface density of star formation. *Monthly Notices of the Royal Astronomical Society*, 456(4):4128â4144, Jan 2016. ISSN 1365-2966. doi:10.1093/mnras/stv2951. URL `http://dx.doi.org/10.1093/mnras/stv2951`.

David Reitze and et al. Adhikari, Rana X. Cosmic Explorer: The U.S. Contribution to Gravitational-Wave Astronomy beyond LIGO. In *Bulletin of the American Astronomical Society*, volume 51, page 35, September 2019.

Adam G. Riess, JÃŒrgen Fliri, and David Valls-Gabaud. Cepheid period-luminosity relations in the near-infrared and the distance to m31 from thehubble space telescopewide field camera 3. *The Astrophysical Journal*, 745(2):156, Jan 2012. ISSN 1538-4357. doi:10.1088/0004-637x/745/2/156. URL `http://dx.doi.org/10.1088/0004-637X/745/2/156`.

M. S. Roberts and R. N. Whitehurst. The rotation curve and geometry of M31 at large galactocentric distances. , 201:327–346, October 1975. doi:10.1086/153889.

Andrew Robertson, Graham P. Smith, Richard Massey, Vincent Eke, Mathilde Jauzac, Matteo Bianconi, and Dan Ryczanowski. What does strong gravitational lensing? The mass and redshift distribution of high-magnification lenses. , 495(4):3727–3739, July 2020. doi:10.1093/mnras/staa1429.

Karolina Rozwadowska, Francesco Vissani, and Enrico Cappellaro. On the rate of core collapse supernovae in the milky way. *New Astronomy*, 83:101498, Feb 2021. ISSN 1384-1076. doi:10.1016/j.newast.2020.101498. URL `http://dx.doi.org/10.1016/j.newast.2020.101498`.

Vera C. Rubin and Jr. Ford, W. Kent. Rotation of the Andromeda Nebula from a Spectroscopic Survey of Emission Regions. , 159:379, February 1970. doi:10.1086/150317.

Barbara Ryden. *Introduction to cosmology*. 2003.

et al. S. Archambault. Dark matter constraints from a joint analysis of dwarf spheroidal galaxy observations with VERITAS. *Physical Review D*, 95(8), apr 2017.

Saurabh, Parth Bambhaniya, and Pankaj S. Joshi. Probing the shadow image of the sagittarius a* with event horizon telescope, 2022.

P. Schneider, J. Ehlers, and E.E. Falco. *Gravitational Lenses*. Springer-Verlag Berlin Heidelberg, 1992. doi:10.1007/978-3-662-03758-4.

Peter Schneider. Detection of (dark) matter concentrations via weak gravitational lensing. , 283(3):837–853, December 1996. doi:10.1093/mnras/283.3.837.

I. Smail, R. S. Ellis, and M. J. Fitchett. Gravitational lensing of distant field galaxies by rich clusters - I. Faint galaxy redshift distributions. , 270:245–270, September 1994. doi:10.1093/mnras/270.2.245.

N. Smirnov. Table for estimating the goodness of fit of empirical distributions. *Ann. Math. Statist.*, 19(2):279–281, 06 1948. doi:10.1214/aoms/1177730256. URL `https://doi.org/10.1214/aoms/1177730256`.

Daniel Smith, Dan Hooper, and Abigail Vieregg. Revisiting AGN as the source of IceCube's diffuse neutrino flux. *JCAP*, 03:031, 2021. doi:10.1088/1475-7516/2021/03/031.

Graham P. Smith, Mathilde Jauzac, John Veitch, Will M. Farr, Richard Massey, and Johan Richard. What if LIGO's gravitational wave detections are strongly lensed by massive galaxy clusters? , 475(3):3823–3828, April 2018. doi:10.1093/mnras/sty031.

Jubee Sohn, Margaret J. Geller, H. Jabran Zahid, Daniel G. Fabricant, Antonaldo Diaferio, and Kenneth J. Rines. The Velocity Dispersion Function of Very Massive Galaxy Clusters: Abell 2029 and Coma. , 229(2):20, April 2017. doi:10.3847/1538-4365/aa653e.

Gary Steigman, Basudeb Dasgupta, and John F Beacom. Precise relic WIMP abundance and its impact on searches for dark matter annihilation. *Phys. Rev. D*, 86(2):023506, jul 2012. ISSN 1550-7998. doi:10.1103/PhysRevD.86.023506. URL `https://link.aps.org/doi/10.1103/PhysRevD.86.023506`.

Louis E. Strigari. Dark matter in dwarf spheroidal galaxies and indirect detection: a review. *Rept. Prog. Phys.*, 81(5):056901, 2018. doi:10.1088/1361-6633/aaae16.

Takahiro Sudoh, Tim Linden, and Dan Hooper. The highest energy hawc sources are leptonic and powered by pulsars, 2021.

S. H. Suyu, V. Bonvin, F. Courbin, C. D. Fassnacht, C. E. Rusu, D. Sluse, T. Treu, K. C. Wong, M. W. Auger, X. Ding, S. Hilbert, P. J. Marshall, N. Rumbaugh, A. Sonnenfeld, M. Tewes, O. Tihhonova, A. Agnello, R. D. Blandford, G. C. F. Chen, T. Collett, L. V. E. Koopmans, K. Liao, G. Meylan, and C. Spiniello. H0LiCOW - I. H_0 Lenses in COSMOGRAIL's Wellspring: program overview. , 468(3):2590–2604, July 2017. doi:10.1093/mnras/stx483.

Ryuichi Takahashi and Takashi Nakamura. Wave Effects in the Gravitational Lensing of Gravitational Waves from Chirping Binaries. , 595(2):1039–1051, October 2003.

Ryuichi Takahashi and Takashi Nakamura. Wave effects in gravitational lensing of gravitational waves from chirping binaries. *Astrophys. J.*, 595:1039–1051, 2003. doi:10.1086/377430.

Ryuichi Takahashi, Masamune Oguri, Masanori Sato, and Takashi Hamana. Probability Distribution Functions of Cosmological Lensing: Convergence, Shear, and Magnification. , 742(1):15, November 2011. doi:10.1088/0004-637X/742/1/15.

Irene Tamborra, Shin'ichiro Ando, and Kohta Murase. Star-forming galaxies as the origin of diffuse high-energy backgrounds: Gamma-ray and neutrino connections, and implications for starburst history. *JCAP*, 09:043, 2014. doi:10.1088/1475-7516/2014/09/043.

Andrew M. Taylor, Markus Ahlers, and Dan Hooper. Indications of Negative Evolution for the Sources of the Highest Energy Cosmic Rays. *Phys. Rev. D*, 92(6):063011, 2015. doi:10.1103/PhysRevD.92.063011.

The LIGO Scientific collaboration. Gravitational wave astronomy with LIGO and similar detectors in the next decade. *arXiv e-prints*, art. arXiv:1904.03187, April 2019a.

The LIGO Scientific collaboration. Gravitational wave astronomy with LIGO and similar detectors in the next decade. *arXiv e-prints*, art. arXiv:1904.03187, April 2019b.

C. To et al. Dark Energy Survey Year 1 Results: Cosmological Constraints from Cluster Abundances, Weak Lensing, and Galaxy Correlations. *Phys. Rev. Lett.*, 126:141301, 2021. doi:10.1103/PhysRevLett.126.141301.

R. B. Tully and J. R. Fisher. Reprint of 1977A&A....54..661T. A new method of determining distance to galaxies. , 500:105–117, February 1977.

E. L. Turner, J. P. Ostriker, and III Gott, J. R. The statistics of gravitational lenses : the distributions of image angular separations and lens redshifts. , 284:1–22, September 1984. doi:10.1086/162379.

Sidney van den Bergh. *The Galaxies of the Local Group*. 2000.

Salvatore Vitale, Will M. Farr, Ken K. Y. Ng, and Carl L. Rodriguez. Measuring the Star Formation Rate with Gravitational Waves from Binary Black Holes. , 886(1):L1, November 2019. doi:10.3847/2041-8213/ab50c0.

Yijun Wang, Rico K. L. Lo, Alvin K. Y. Li, and Yanbei Chen. Identifying Type-II Strongly-Lensed Gravitational-Wave Images in Third-Generation Gravitational-Wave Detectors. 1 2021.

Miles Winter, Gabrijela Zaharijas, Keith Bechtol, and Justin Vandenbroucke. Estimating the GeV Emission of Millisecond Pulsars in Dwarf Spheroidal Galaxies. *Astrophys. J. Lett.*, 832(1):L6, 2016. doi:10.3847/2041-8205/832/1/L6.

Lilan Yang, Xuheng Ding, Marek Biesiada, Kai Liao, and Zong-Hong Zhu. How Does the Earth's Rotation Affect Predictions of Gravitational Wave Strong Lensing Rates? , 874 (2):139, April 2019. doi:10.3847/1538-4357/ab095c.

Lilan Yang, Shichao Wu, Kai Liao, Xuheng Ding, Zhiqiang You, Zhoujian Cao, Marek Biesiada, and Zong-Hong Zhu. Event rate predictions of strongly lensed gravitational waves with detector networks and more realistic templates. *arXiv e-prints*, art. arXiv:2105.07011, May 2021.

Xing-Jiang Zhu, E. Howell, T. Regimbau, D. Blair, and Zong-Hong Zhu. Stochastic Gravitational Wave Background from Coalescing Binary Black Holes. , 739(2):86, October 2011. doi:10.1088/0004-637X/739/2/86.

F. Zwicky. Die Rotverschiebung von extragalaktischen Nebeln. *Helv. Phys. Acta*, 6:110–127, 1933. doi:10.1007/s10714-008-0707-4.